



AFRL-RQ-WP-TR-2015-0130

**SCIENTIFIC RESEARCH PROGRAM FOR POWER,
ENERGY, AND THERMAL TECHNOLOGIES**

**Task Order 0002: Power, Thermal and Control Technologies and
Processes Experimental Research**

**Subtask: Laboratory Test Set-up to Evaluate Electromechanical Actuation
Systems for Aircraft Flight Control**

Street A. Barnett

University of Dayton Research Institute

AUGUST 2015

Interim Report

Approved for public release; distribution unlimited.

See additional restrictions described on inside pages

STINFO COPY

**AIR FORCE RESEARCH LABORATORY
AEROSPACE SYSTEMS DIRECTORATE
WRIGHT-PATTERSON AIR FORCE BASE, OH 45433-7541
AIR FORCE MATERIEL COMMAND
UNITED STATES AIR FORCE**

NOTICE AND SIGNATURE PAGE

Using Government drawings, specifications, or other data included in this document for any purpose other than Government procurement does not in any way obligate the U.S. Government. The fact that the Government formulated or supplied the drawings, specifications, or other data does not license the holder or any other person or corporation; or convey any rights or permission to manufacture, use, or sell any patented invention that may relate to them.

This report was cleared for public release by the USAF 88th Air Base Wing (88 ABW) Public Affairs Office (PAO) and is available to the general public, including foreign nationals.

Copies may be obtained from the Defense Technical Information Center (DTIC)
(<http://www.dtic.mil>).

AFRL-RQ-WP-TR-2015-0130 HAS BEEN REVIEWED AND IS APPROVED FOR
PUBLICATION IN ACCORDANCE WITH ASSIGNED DISTRIBUTION STATEMENT.

*//Signature//

GREGORY L. RHOADS
Program Manager
Mechanical and Thermal Systems Branch
Power and Control Division

//Signature//

DANIEL M. HATZUNG, Acting Chief
Mechanical and Thermal Systems Branch
Power and Control Division
Aerospace Systems Directorate

This report is published in the interest of scientific and technical information exchange, and its publication does not constitute the Government's approval or disapproval of its ideas or findings.

*Disseminated copies will show “//Signature//” stamped or typed above the signature blocks.

REPORT DOCUMENTATION PAGE				Form Approved OMB No. 0704-0188	
<p>The public reporting burden for this collection of information is estimated to average 1 hour per response, including the time for reviewing instructions, searching existing data sources, gathering and maintaining the data needed, and completing and reviewing the collection of information. Send comments regarding this burden estimate or any other aspect of this collection of information, including suggestions for reducing this burden, to Department of Defense, Washington Headquarters Services, Directorate for Information Operations and Reports (0704-0188), 1215 Jefferson Davis Highway, Suite 1204, Arlington, VA 22202-4302. Respondents should be aware that notwithstanding any other provision of law, no person shall be subject to any penalty for failing to comply with a collection of information if it does not display a currently valid OMB control number. PLEASE DO NOT RETURN YOUR FORM TO THE ABOVE ADDRESS.</p>					
1. REPORT DATE (DD-MM-YY) August 2015		2. REPORT TYPE Interim		3. DATES COVERED (From - To) 01 January 2015 – 15 May 2015	
4. TITLE AND SUBTITLE SCIENTIFIC RESEARCH PROGRAM FOR POWER, ENERGY, AND THERMAL TECHNOLOGIES Task Order 0002: Power, Thermal and Control Technologies and Processes Experimental Research Subtask: Laboratory Test Set-up to Evaluate Electromechanical Actuation Systems for Aircraft Flight Control				5a. CONTRACT NUMBER FA8650-12-D-2224-0002	
				5b. GRANT NUMBER	
				5c. PROGRAM ELEMENT NUMBER 62203F	
6. AUTHOR(S) Street A. Barnett				5d. PROJECT NUMBER 3145	
				5e. TASK NUMBER N/A	
				5f. WORK UNIT NUMBER Q1BD	
7. PERFORMING ORGANIZATION NAME(S) AND ADDRESS(ES) University of Dayton Research Institute Energy Technology and Materials Division 300 College Park Dayton, OH 45469-0170				8. PERFORMING ORGANIZATION REPORT NUMBER	
9. SPONSORING/MONITORING AGENCY NAME(S) AND ADDRESS(ES) Air Force Research Laboratory Aerospace Systems Directorate Wright-Patterson Air Force Base, OH 45433-7541 Air Force Materiel Command United States Air Force				10. SPONSORING/MONITORING AGENCY ACRONYM(S) AFRL/RQQM	
				11. SPONSORING/MONITORING AGENCY REPORT NUMBER(S) AFRL-RQ-WP-TR-2015-0130	
12. DISTRIBUTION/AVAILABILITY STATEMENT Approved for public release; distribution unlimited.					
13. SUPPLEMENTARY NOTES PA Case Number: 88ABW-2015-1582; Clearance Date: 06 Apr 2015. This report is a Master of Science thesis.					
14. ABSTRACT <p>A laboratory apparatus and data acquisition (DAQ) system were constructed for evaluating aircraft flight control actuators under simulated mission profiles. An MTS Systems Corporation hydraulic load frame was used to simulate a control surface's aero load. A National Instruments Corporation (NI)-based DAQ system was used to record the motor controller's DC bus voltage at a high rate, actuator's position, load, and temperatures. The DC bus root mean square (RMS) voltage, current, and power, and regenerative power were recorded by a Newton's 4th power analyzer. Key performance characteristics tests such as frequency response, step response, reversal, backlash, and holding with a Danahar EC5 actuator were carried out to verify this laboratory setup.</p> <p>The continuous frequency sweeping test revealed that the electromechanical actuator (EMA) reached the speed limit first, then the current limit, and finally the temperature limit. When the actuator's electronics reached the thermal limit, the actuator controller drastically reduced its power. This caused drastic magnitude attenuation and phase lagging. Continuous frequency sweeping proved to be a useful test to evaluate the EMA's characteristics.</p>					
15. SUBJECT TERMS electromechanical, actuation, flight control, hydraulic load frame					
16. SECURITY CLASSIFICATION OF:			17. LIMITATION OF ABSTRACT: SAR	18. NUMBER OF PAGES 118	19a. NAME OF RESPONSIBLE PERSON (Monitor) Gregory L. Rhoads 19b. TELEPHONE NUMBER (Include Area Code) N/A
a. REPORT Unclassified	b. ABSTRACT Unclassified	c. THIS PAGE Unclassified			

LABORATORY TEST SET-UP TO EVALUATE ELECTROMECHANICAL
ACTUATION SYSTEM FOR AIRCRAFT FLIGHT CONTROL

Thesis

Submitted to

The School of Engineering of the
UNIVERSITY OF DAYTON

In Partial Fulfillment of the Requirements for

The Degree of

Master of Science in Mechanical Engineering

By

Street A. Barnett

UNIVERSITY OF DAYTON

Dayton, Ohio

May, 2015

TABLE OF CONTENTS

LIST OF FIGURES	iv
LIST OF TABLES.....	ix
ACRONYMS	x
LABORATORY TEST SET-UP TO EVALUATE ELECTROMECHANICAL ACTUATION SYSTEM FOR AIRCRAFT FLIGHT CONTROL.....	xii
ABSTRACT.....	xiii
ACKNOWLEDGEMENTS	xv
INTRODUCTION	1
BACKGROUND	5
PURPOSE.....	12
EXPERIMENTAL APPARATUS.....	14
Test Methodology	14
Test Apparatus.....	15
Characterizing Mechanical Hardware.....	16
Press frequency sweeps	16
Recording Mechanical Behavior	23
Recording Thermal Behavior	25
High Speed DAQ	31

Low Speed DAQ	37
CALIBRATION AND UNCERTAINTY	38
TEST RESULTS.....	42
Backlash	42
Step Response	47
Reversal Test.....	58
Frequency Response.....	63
Holding Tests	70
DYNAMIC LOAD CONTROL	77
Cascade Control	78
Signal Response of the EMA and Hydraulic Press Fixture	79
Recording Electrical Data	83
CONCLUSION.....	86
BIBLIOGRAPHY	88
APPENDIX.....	91
Hardware Specifications	91
Kollmorgen EC5 Electromechanical Actuator	91
Kollmorgen AKM42G Servomotor.....	91
Kollmorgen S610 Servodrive	92

MTS Servohydraulic Load Frame	92
MTS Servohydraulic Controller	93
MTS Force Transducer	94
National Instruments Data Acquisition Machine	95
Newton's 4 th Power Analyzer.....	98
LEM Current Transducer and Tectronix Voltage Probe	99
Omega Thermocouples Probes	99

LIST OF FIGURES

Figure 1 - EPAD Program's electromechanical actuator and power control and monitor electronics [7].....	2
Figure 2 - Electro-hydrostatic Actuator and an Electro-mechanical Actuator [7].....	8
Figure 3 – Photograph of Automatic Test Equipment [24]	9
Figure 4 – Detail of Automatic Test Equipment [24]	9
Figure 5 – Hardware model of the FLEA [25]	11
Figure 6 - Schematic of Experiment Test Setup	15
Figure 7 - Hydraulic Press Frequency Sweep.....	17
Figure 8 – 1500 N Frequency Sweep for Press.....	18
Figure 9 - Close up view of the first 2 Hz of the 1500 N frequency sweep	19
Figure 10 - Close up section near 39 Hz of the 1500 N frequency sweep.....	19
Figure 11 - Hydraulic Press Bode Plot at 1500 N.....	20
Figure 12 - Frequency sweep of press with 13 kN amplitudes.....	21
Figure 13 - Close up view of the first 1 Hz of the 13 kN frequency sweep	21
Figure 14 - Close up section at the end of the of the 13 kN frequency sweep	22
Figure 15 - Hydraulic Press Bode Plot 13 kN.....	22
Figure 16 – Filtered Force Signal	24

Figure 17 – Filtered Displacement Signal	24
Figure 18 - Thermocouple Placement in the Motor of the EMAS [1].....	26
Figure 19 - Thermocouple Identification [1]	27
Figure 20 - Heat sink (left) and Servodrive board (Right) [1].....	28
Figure 21 - Underside of heat sink with placement of thermocouples shown [1]	28
Figure 22 - Thermocouples embedded in Drive 1	29
Figure 23 - Servodrive board with Heat Sink (left) and without Heat Sink (Right) [1] ...	30
Figure 24 - Thermocouples embedded in Drive 2 [1].....	30
Figure 25 - Servodrive System Completed with Thermocouples [1]	31
Figure 26 - Measurements made on 3 Motor Phases.....	32
Figure 27 - Electrical Measurements	33
Figure 28 - Schematic for capturing DC bus current and voltage	34
Figure 29 - Simplified Schematic of where DC current and voltage are being recorded.	35
Figure 30 - High Speed Data Acquisition System.....	36
Figure 31 - Low Speed Acquisition System	37
Figure 32 - Backlash Test Force Profile	43
Figure 33 - Backlash Test Set-up.....	44
Figure 34 - Backlash Test Results under 200N Alternate Load	45
Figure 35 - Backlash Test Result under 1000N Alternate Load.....	45
Figure 36 - Backlash Test Result under 2500 N Alternate load, 50% of motor's stall load	46
Figure 37- Definition of Overshoot, settling time, and rising time from a Step Response	47

Figure 38-Mechanical Step Response Results	48
Figure 39 - Rise Time and Settling Time of Step Response	49
Figure 40 - Overshoot of Step Response	49
Figure 41-Rise Time and Settling Time of Step Response	50
Figure 42-Settling Time of Step Response	50
Figure 43 – DC bus Voltage and Current Data from Step Response.....	51
Figure 44 - DC Bus Electrical Power in Step Response Test	52
Figure 45 - DC bus Voltage and Regen Resistor Current Data from Step Response.....	53
Figure 46 - Electrical Power in Watts Recorded on the Regen Resistor	53
Figure 47 - Regenerative Portion of the Step Response Test Recorded By the Power Analyzer	55
Figure 48 –Electrical Power in Watts Recorded on the Regenerative Resistor.....	55
Figure 49 - Commanded Displacement for the Reversal Test	59
Figure 50-Mechanical Reversal Results	60
Figure 51 - Close up of first reversal	60
Figure 52 - Close up of second reversal.....	61
Figure 53 - DC bus Voltage and Current	62
Figure 54 - Electrical Power from Reversal Test.....	63
Figure 55 - Commanded Profile for the 3.8 mm Frequency Response Test.....	64
Figure 56 - Displacement Results from the 3.8 mm Frequency Sweep Test.....	65
Figure 57 - Velocity Results from the 3.8 mm Frequency Sweep Test	65
Figure 58 - Voltage and Current Results from the 3.8 mm Frequency Sweep Test	66

Figure 59 - Thermal Voltage and Current Results from the 3.8 mm Frequency Sweep Test.....	66
Figure 60 - Electrical Power Results from the 3.8 mm Frequency Sweep Test	67
Figure 61 - Close up view of Displacement Results When Reaching the Velocity Limit	68
Figure 62 - Close up view of Displacement Results When Reaching the Current Limit .	69
Figure 63 - Close up view of Displacement Results When Reaching the Temperature Limit.....	69
Figure 64 - Bode Plot of 3.8 mm Frequency Sweep Test.....	70
Figure 65 - Temperature plot for holding 5000 N with no Disturbance	71
Figure 66 - Temperature plot of motor for holding 5000 N with no Disturbance	72
Figure 67 - Temperature plot of IGBTs for holding 5000 N with no Disturbance.....	72
Figure 68 - Commanded and Recorded Displacement for the 5000 N Holding Test with a Sinusoidal Disturbance	74
Figure 69 - Commanded and Recorded Force for the 5000 N Holding Test with a Sinusoidal Disturbance	74
Figure 70 - Temperature plot for holding 5000 N with Sinusoidal Disturbance	75
Figure 71 - Temperature plot of Motor for holding 5000 N with Sinusoidal Disturbance	75
Figure 72 - Temperature plot of IGBTs for holding 5000 N with Sinusoidal Disturbance	76
Figure 73 - Control of Force and Displacement over a Dynamic Profile	78
Figure 74 - EMA Test System Control Scheme	79
Figure 75 - Cascade Control Command Generation.....	79
Figure 76 - Diagram of Signal Response Test	80

Figure 77 – Segment of a 4 Hz Signal response of EMA.....	81
Figure 78 - Time Delay vs Frequency for Press and EMA [29]	81
Figure 79 - System Spring Constant (K) [29]	83
Figure 80 - Unfiltered and Filtered DC Bus Voltage.....	84
Figure 81 - Unfiltered and Filtered DC Bus Current	85
Figure 82 - Industrial EMA under test.....	91
Figure 83 - EMA motor specifications	92
Figure 84- EMA drive specifications.....	92
Figure 85 - Hydraulic Press specifications	93
Figure 86 - Hydraulic Press Controller specifications	94
Figure 87 - Hydraulic Press Load Cell	94
Figure 88 - PXIe Chassis	95
Figure 89 - PXI Controller.....	95
Figure 90 - Module 1—Electrical Card	96
Figure 91 - Module 2—Mechanical Card.....	96
Figure 92 - Module 3—Thermal Card	97
Figure 93 - Newton's 4th Power Analyzer.....	98
Figure 94 - Electrical Sensors	99
Figure 95 - Thermocouples.....	99

LIST OF TABLES

Table 1 - Summary of measurement uncertainty	41
Table 2 - Backlash of EMA gear train under varying loads	46
Table 3 - System Spring Constant Results.....	83

ACRONYMS

DAQ	Data Acquisition
DC	Direct Current
EHA	Electro-Hydrostatic Actuator
EHAS	Electro-Hydrostatic Actuator System
EMA	Electromechanical Actuator
EMAS	Electromechanical Actuator System
EMI	Electromagnetic Interference
EPAD	Electrically Powered Actuation Design
FLEA	Flyable Electro-Mechanical Actuator
HAS	Hydraulic Actuation System
HPU	Hydraulic Power Unit
HSM	Hydraulic Service Manifold
IGBT	Insulated Gate Bipolar Transistor
LabVIEW	Laboratory Virtual Instrumentation Engineering Workbench

LVDT	Linear Voltage Displacement Transducer
MEA	More Electric Aircraft
NASA	National Aeronautics and Space Administration
NI	National Instruments
PCU	Power Control Unit
PCME	Power Control and Monitor Electronics
PID	Proportional, Integral, Derivative
PMDC	Permanent Magnet Direct Current
PWM	Pulse Width Modulated
RMS	Root Mean Square
RT	Real-Time
SNR	Signal to Noise Ratio
SRA	Systems Research Aircraft
TC	Thermocouple
VAC	Volts Alternating Current
VDC	Volts Direct Current
VI	Virtual Instrument

LABORATORY TEST SET-UP TO EVALUATE ELECTROMECHANICAL
ACTUATION SYSTEM FOR AIRCRAFT FLIGHT CONTROL

Name: Barnett, Street Anthony

APPROVED BY:

Quinn Leland, Ph.D.
Advisory Committee Chairman
Senior Mechanical Engineer
AFRL, WPAFB, Ohio

Jamie Ervin, Ph.D.
Committee Member
Professor
Department of Mechanical
and Aerospace Engineering

Bang Tsao, Ph.D.
Committee Member
Instructor
Department of Electrical
and Computer Engineering

Steve Fuchs
Committee Member
Senior Engineering Researcher
UDRI

John G. Weber, Ph.D.
Associate Dean
School of Engineering

Eddy Rojas, Ph.D., M.A., P.E.
Dean
School of Engineering

ABSTRACT

LABORATORY TEST SET-UP TO EVALUATE ELECTROMECHANICAL ACTUATION SYSTEM FOR AIRCRAFT FLIGHT CONTROL

Name: Barnett, Street A.
University of Dayton

Advisor: Dr. Quinn Leland

A laboratory apparatus and data acquisition system were constructed for evaluating aircraft flight control actuators under simulated mission profiles. A MTS hydraulic load frame was used to simulate a control surface's aero load. A NI based DAQ system was used to record the motor controller's DC bus voltage at a high rate, actuator's position, load, and temperatures. The DC bus rms voltage, current, and power, and regenerative power were recorded by a Newton's 4th power analyzer. Key performance characteristics tests such as frequency response, step response, reversal, backlash, and holding with a Danahar EC5 actuator were carried out to verify this laboratory setup.

The continuous frequency sweeping test revealed that the EMA reached the speed limit first, then the current limit, and finally the temperature limit. When the actuator's electronics reached the thermal limit, the actuator controller drastically reduced its power. This caused drastic magnitude attenuation and phase lagging. Continuous frequency sweeping proved to be a useful test to evaluate the EMA's characteristics.

The lab tests showed that holding presents the most significant challenge to the thermal management of an EMA system. To reduce the thermal gradient within the motor, a half rotation back forth at 0.01 Hz sinusoidal disturbance was imposed during holding to evenly engage the motor's three phases. This resulted in an 81% temperature variation reduction among the three windings. Although this small motion disturbance is effective in reducing the motor and motor drive's thermal gradient, it is not known if such a disturbance is feasible in practice.

The step response and reversal test showed that when an EMA reverses direction or suddenly decelerates, a significant spike of regenerative power occurred. This regenerative power could present itself as a thermal challenge to an aircraft flight control EMA system.

Using the MTS hydraulic load frame to simulate a dynamic aero load of a flight control surface in synchronization with position movement of an actuator proved to be a challenge. A double loop control scheme has been derived which compensates the time delay difference between the load frame and the actuator. It is our hope that this control strategy, once fully implemented, will enable more accurate dynamic load control in simulating an EMA's mission profile for performance evaluation.

ACKNOWLEDGEMENTS

First, I would like to thank my advisor, Dr. Quinn Leland, for providing me the opportunity to work on such a challenging and rewarding project. I would also like to thank committee members, Dr. Jamie Ervin, Dr. Bang Tsao, and Steve Fuchs for their guidance and participation. I also owe a debt of gratitude to the following people who over the years provided valuable technical support and advice: Bryan Harris, Cameron Riepenhoff, Victor Tsao, Evan Racine, and John Murphy of UDRI, Justin DelMar and Ben Razidlo of AFRL, Tommy Baudendistel and Mike Boyd of PCKA, Tom Greene, Laura Walker, and Josh Johnson of UES. Lastly, I am grateful to Joseph Weimer, Dr. Russell Spyker, and Dr. Joseph Fellner of AFRL who provided laboratory facilities and equipment.

CHAPTER 1

INTRODUCTION

Aircraft Flight control systems have made major advances throughout the years, from wing warping on the Wright's first glider to modern day fighter jets, whose design is aerodynamically unstable and requires fly-by-wire technology. Modern aircraft employ fly-by-wire and auto stabilization processes executed by an on board flight computer in order to master the principle of flight control [1].

Flight control systems are made up of primary and secondary control surfaces for maneuvering. Primary flight control surfaces are used for pitch, roll, and yaw control. They are comprised of the canard, flaperons (flaps and ailerons), and rudder [2]. Secondary flight surfaces provide increased lift control by increasing wing camber and improving wing aerodynamics. However, increased lift control amplifies drag [3]. Combat aircraft are highly agile, maneuverable during flight, and have high thrust capabilities which can overcome this drag.

Flight control linkage systems connect the pilot with the control surfaces responsible for maneuvering [4]. The linkage evolved from manually operated direct mechanical rods, levers, cables, and pulleys to fully power operated hydraulic control. This, in turn,

evolved into 'Fly-by-wire', where direct mechanical linkages between the cockpit controls and the control surfaces were replaced by electrical signaling [5].

Fly-by-wire provides the pilot with the mechanical advantage necessary to execute maneuvering commands under enormous loads in high speed flight and offer artificial feel through feedback so the pilot is not flying blind. Aeronautical and space programs are interested in developing reliable power-by-wire actuation systems to replace existing hydraulic actuation systems for flight surface controls in order to improve efficiency, reliability, and maintainability [6]. The Air Force, Navy, and NASA collaborated together to create the Electrically Powered Actuation Design (EPAD) program to develop and validate power-by-wire actuation technology through flight tests on a primary flight control surface of a tactical aircraft [7]. The EPAD program replaced standard hydraulic actuators on the left aileron of the NASA F/A-18B Systems Research Aircraft (SRA) with electromechanical actuators (EMA) flown throughout the SRA flight envelope. The two primary pieces of hardware making up the system were the EMA and its Power Control and Monitor Electronics or PCME. Figure 1 shows both devices.

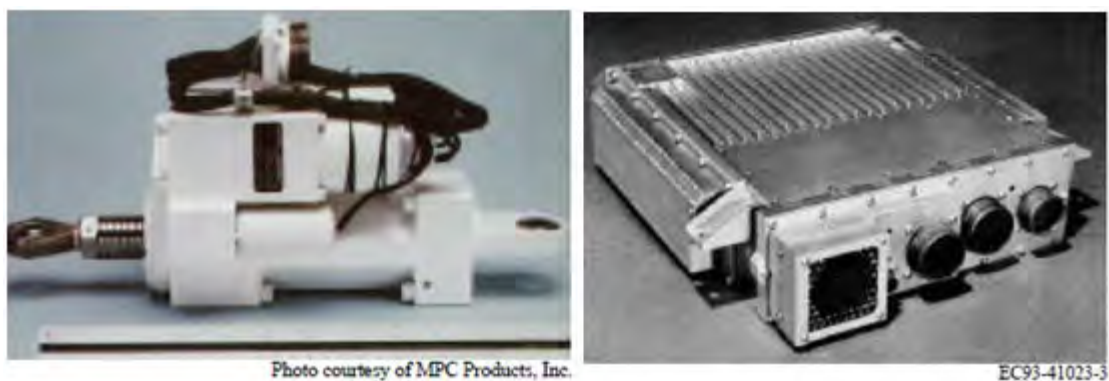


Figure 1 - EPAD Program's electromechanical actuator and power control and monitor electronics [7]

During flight tests, positions of EMA controlled left aileron and hydraulic controlled right aileron were recorded and compared to assess the EMA performance. Other parameters, such as flight profile, actuator and motor control electronics temperature, voltage, and current were also recorded during the flight test [7]. The lessons learned and unresolved research areas provide the basis for the Electromechanical Actuation System Integration and Thermal Management project. This project is to better understand the thermal management issues associated with EMAS for in flight scenarios. It was thought before the flight test that highly transient actuation loads would account for the majority of thermal generation over the duration of a mission. However, it was found that the majority of the heat was generated during conditions where the ailerons were at full deflection under constant aero loads, requiring the servomotor to maintain constant torque output causing high current draw and heat generation due to winding resistance of the motor [8]. In the early stages of electrohydraulic actuation design and integration, peak electrical loads on electrical generation system were grossly underestimated, thus requiring the redesign of aircraft electric power generation systems [8].

To implement EMA for aircraft flight critical control surface actuation with confidence, it is important to understand the Electromechanical Actuator System (EMAS) performance in terms of its interaction with the aircraft electrical power system and thermal characteristics over the flight envelope. An EMAS's transient behavior, which includes peak and regenerative powers [9] and thermal load, has a profound influence on EMA design and integration with aircraft electrical power and structural systems. The goal of this thesis is to design and build a laboratory apparatus that is able to subject an

EMA to a simulated mission profile and record the EMA's performance. The simulated missions would represent an aircraft's flight maneuvering (e.g., roll, dive, high rate climb, and steady level flight) and takeoff / landing approaches when aircraft stall speed is a concern and maximum lift is required by control surfaces. Experimental data, such as electrical, mechanical, the thermal parameters, are recorded for EMA characterization and evaluation.

CHAPTER 2

BACKGROUND

The earliest successful form of flight surface control of an aircraft was wing warping, originally developed by the Wright Brothers in the early 20th century [10]. Wing warping involved a system of pulleys and cables affixed to the trailing edges of the wing that would twist each end of the wing in opposite directions. This mechanical flight control system was controlled by the use of a yoke, also known as a control column or center stick located in the cockpit. This concept involved flexing of aircraft structural members unfortunately made maneuvering difficult to control and was susceptible to failure in flight. These relatively soft wings were replaced with a more rigid wing design in order to compensate for the increased speeds in the evolution of aircraft. As a result of the wings becoming stiffer, wing warping was replaced by aileron controls [11]. The use of ailerons made flight maneuverability easier to control and also eliminated the need to flex the structural members of the aircraft. This manual flight control system used push rods, tension cables, pulleys, counterweights, and sometimes chains to transmit the forces applied by the pilot from the yoke directly to the control surfaces on the aircraft. As aircraft grew in size, speed, and performance, the pilot could no longer handle the aerodynamic forces applied to the flight control surfaces. In the 1940s, hydro-mechanical systems were used to overcome the limitations of the pilot and the manual flight control

system while still giving the pilot the ability to sense small forces proportional to aero loads on the aircraft [5] [12]. There are two parts to the hydraulic actuation system (HAS), the mechanical circuit and the hydraulic circuit. The mechanical circuit linked the cockpit controls with the hydraulic circuits similar to the old mechanical flight control system with the use of rods, pulleys, and chains. The hydraulic circuit used hydraulic pumps, reservoirs, pipes and valves to control the flight control surface. The hydraulic pumps generated hydraulic pressure which, in turn, powered the actuator which would move the flight control surface to the desired position [13]. The HAS used three separate components in its design: hydraulic supply system, valves and connections associated with the control network, and actuators. It only takes one of these systems to fail to make the aircraft inoperable. Because the hydraulic system is constantly on and under high pressure, even when the actuator is not moving, its efficiency is very low. Also leakage of the hydraulic lines at several thousand psi resulted in high maintenance cost.

To replace the HAS, the Electro-hydrostatic actuator system (EHAS) was implemented in the past two decades. The EHAS was first introduced commercially in the Airbus A380 in 1995 [14] [15]. The EHAS is a localized hydraulic system, composed of a local fluid reservoir, a pump driven by an electric motor, and an actuator. The pump is on only when the actuator is moving. The EHAS uses a high powered motor that moves to a fixed angle repeatedly and accurately [16]. The motor in the EHA is used to drive a reversible pump tied to a hydraulic cylinder which moves fluid in order to pressurize or depressurize the cylinder, causing the piston inside to move back and forth. This piston is directly linked to the actuator arm, so when it moves, the actuator moves, see Figure 2a. The EHAS encompasses all of these components into one packaged unit.

In addition, the EHAS only draws power when the actuator is being moved, meaning the pressure is maintained when the motor stops. This behavior is in contrast to that of the HAS where the hydraulic pumps are on continuously to maintain a constant pressure which is a large power drain. Functioning in power on demand mode, The use of the EHAS significantly reduced power consumption. Another advantage in using is weight reduction due to the elimination of centralized hydraulic piping lines. However, fluid leakage and associated maintenance still remains [17]. In addition, there is a new challenge associated with EHAS, which is the thermal management. In the HAS the circulating hydraulic fluid acts as a temperature regulator, while in EHAS the fluid could get too cold or the system too hot.

Finally, an increasing pace in aviation towards a MEA through advancement in permanent magnet direct current (PMDC) motors [14] operating at 270 VDC, high power solid state switching devices, and lightweight microprocessors yielded the EMAS which completely eliminated the need for hydraulic fluid [18]. EMAS utilizes power drive electronics to drive a PMDC motor operating a reduction gear box followed by a rotary to linear conversion device such as a ball screw/nut assembly attached to the control surface linkage (Figure 2b). EMAS offer features such as power on demand, increased stiffness, reduced weight and maintenance, and a reduction in lifecycle costs [19] [20]. The EMA is an appealing alternative to EHA, since it allows the elimination of local hydraulic circuits, implying a significant maintenance cost reduction due to the absence of wearing parts such as seals [20]. They provide an energy efficient means to flight surface control, thus reducing loads required by conventional hydraulic systems [21]. However, electro-mechanical actuators still lack the knowledge base relative to other fielded actuator types,

particularly with regard to thermal management issues [22] [23]. Therefore, an effort was undertaken to characterize energy loads associated with this alternative actuation and its systems level effect. The research described in this thesis is directly correlated to characterizing the electrical and thermal loads associated with EMAS for aircraft surface controls.

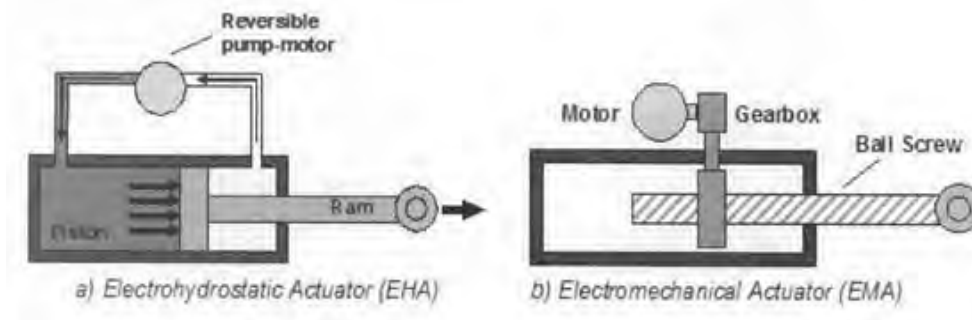


Figure 2 - Electro-hydrostatic Actuator and an Electro-mechanical Actuator [7]

In order to have a better understanding of EMAS for flight control surfaces and how they operate under real time flight conditions, test stands have been developed to mimic aero loads [24] [25] [26]. These test stands are used for the prognostic testing of EMAS that have had mechanical or electrical faults injected into them. The faults are incorporated into the system in order to better understand the EMA reliability, and to aid in designing fault detection software for real time flight applications.

Currently, research is being done to better understand aircraft EMAS characteristics under real time flight conditions. An example of such research which utilizes a lab apparatus for testing and monitoring high performance EMAs was developed in reference 24. The lab apparatus allowed for testing up to two EMAs operating simultaneously. Utilizing a hydraulic actuator to emulate an aerodynamic load,

the behavior of real flight control surfaces in diverse test conditions was achieved. While the lab apparatus was operating, it measured and monitored mechanical, hydraulic and electrical parameters while maintaining dynamic control. The lab apparatus is shown in Figure 3 and Figure 4.

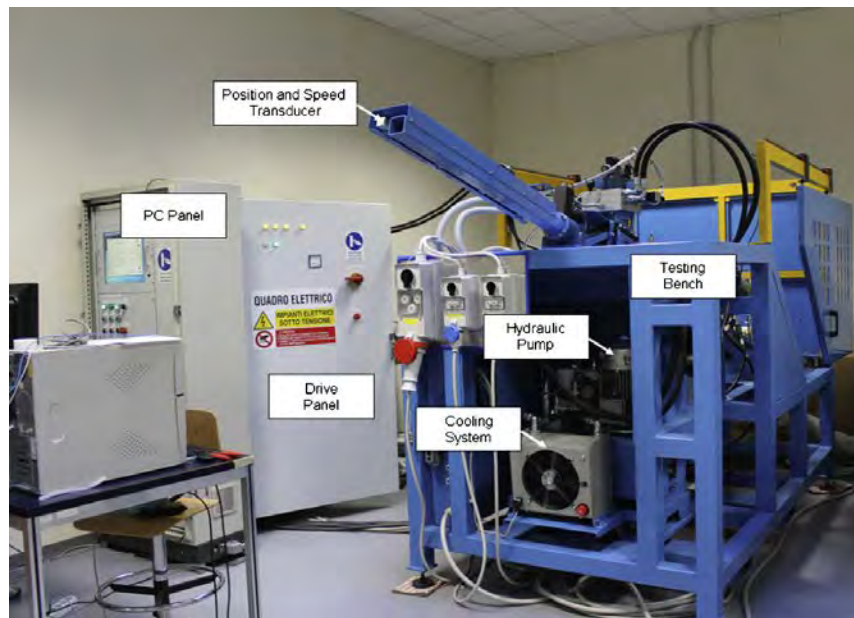


Figure 3 – Photograph of Automatic Test Equipment [24]

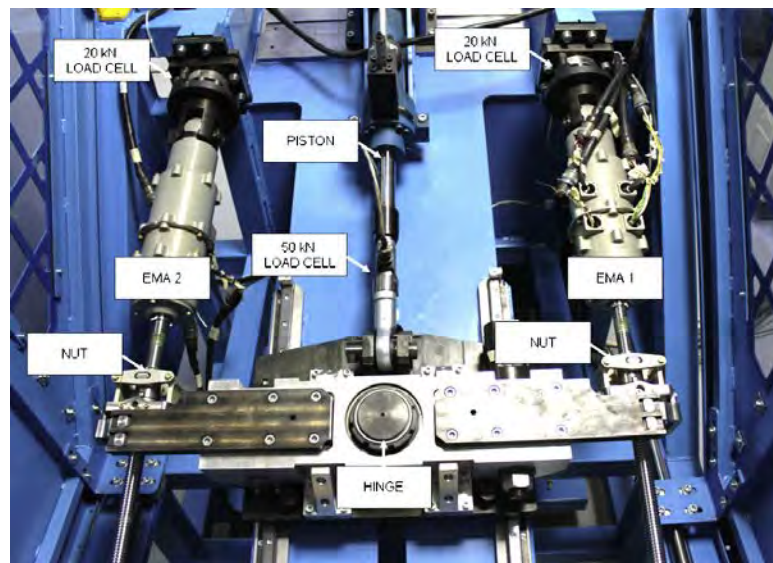


Figure 4 – Detail of Automatic Test Equipment [24]

The tests run in the apparatus showed satisfactory results in simulating real aircraft loads and recording all critical parameters to be analyzed. Since the laboratory apparatus can also be used to study two EMAs simultaneously, future testing for force fighting can be implemented in the test profiles. Further improvements need to be implemented for the apparatus, such as the hydraulic load control, in which the hydraulic circuit had difficulty in following the imposed profile. Also, the lab apparatus was developed to test a specific kind of EMA, and the design may not be able to easily test different aircraft EMAs. The sampling frequency of the data collected was at 10 kHz which is low for recording electrical data. With such a low sampling rate of electrical data, it would be difficult to sample dynamic spikes in EMA power draw under various conditions, especially if the EMA driver has a switching frequency higher than 10kHz.

Other research which utilized a lab apparatus called the flyable electro-mechanical actuator stand (FLEA) to be placed on a variety of aircraft is described in reference 25. The goal was to design and fly a self-contained portable test apparatus with three actuators. Two actuators would be tested under a third actuator that would implement a real time aero load. This entire apparatus was constructed with T-slotted aluminum segments that were connected with brackets and fasteners to allow for easy assembly and disassembly. Figure 5 depicts the hardware model of the FLEA.

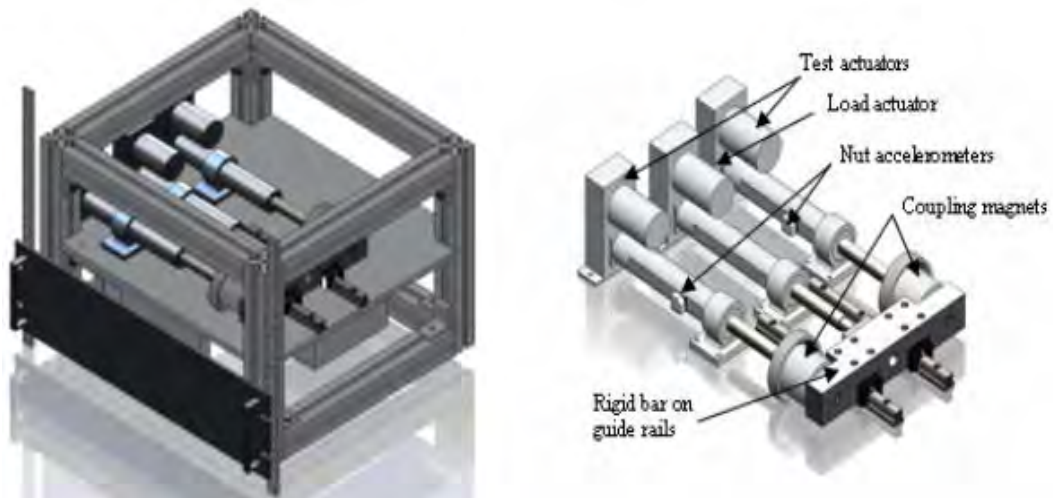


Figure 5 – Hardware model of the FLEA [25]

One of the EMAs was injected with faults while the other actuator being tested has no faults. The load is switched from the healthy actuator to the faulty actuator while in flight. The profile of displacement and load applied to them is derived from real-time flight data from one of the control surfaces of a UH-60 Blackhawk helicopter [25] [26].

CHAPTER 3

PURPOSE

The purpose of this thesis is to develop a test apparatus to characterize EMAS performance. This was done by controlling a hydraulic load fixture to simulate a load on the EMA and record data using a data acquisition (DAQ) machine to allow EMA evaluation. In short, a linear EMA with a rotary motor was placed in line with a hydraulic load fixture. The load fixture was given load commands (emulating the loads that would be experienced by a flight control surface actuator) while the EMA was provided position commands. The EMA used to validate the lab apparatus was a Danaher Motion EC5 linear actuator driven by an S610 controller. It performed under a load provided by an MTS 370.10 22 KIP hydraulic load fixture driven by an MTS FlexTest60 controller. The specifications of the EMAS and hydraulic load fixture can be found in the Appendix – Hardware and Control Equipment. The hydraulic load fixture and EMA are coupled together and affect each other. Specifically, the EMA's stroke was seen as a disturbance to the hydraulic press as it attempts to provide a particular force, and the press's force was seen as a disturbance to the EMA's stroke. The hydraulic press emulates the load that the EMA must overcome. Stroke, load force, voltages, and current to the EMA, and temperatures at selected locations in and on the motor and controller were recorded.

Additionally, mechanical, thermal and electrical parameters were measured at high sampling rates to identify stresses associated with varying mission profiles. These were recorded using National Instruments (NI) DAQ.

Along with a simulated mission profile based on NASA Dryden flight test study [7], several artificial mission profiles were generated to aid in the characterization of various EMA performance measures. These profiles are designed to evaluate various characteristics of EMAs that are important parameters of any aircraft flight control actuator. A more detailed description of the test setup and procedure can be found in the Experimental Apparatus section of this thesis.

CHAPTER 4

EXPERIMENTAL APPARATUS

A laboratory test apparatus, including hardware, control software, data acquisition system, and test methodology was developed to simulate flight control conditions to study and test EMAS's performance. During testing, the DAQ will record the EMA's mechanical, electrical, and thermal responses. Additionally, a control block which would execute commands, maintain stability of the experiment, and trigger measurement by the acquisition equipment at consistent time intervals with the use of NI LabVIEW Real Time was created. Finally, rate limits based on the specifications of each test component was evaluated in order to constrain the testing range to a safe test envelope for the EMA being used.

Test Methodology

A hydraulic load fixture was controlled to simulate aero loads an EMA would experience in flight while the EMA was commanded a motion profile corresponding to the loads. A NI instrument based DAQ system was assembled to record mechanical, electrical and thermal data that could be used to evaluate the EMA was tested. A

LabVIEW based control program synchronized the action of the hydraulic load, EMA motion, and data recording.

Test Apparatus

The overall test setup included mechanical hardware, control hardware, and a data acquisition system. Figure 6 is a schematic of the test apparatus setup. Thermocouples were embedded in the servomotor and EMA electronic control box. The force experienced by the EMA was measured by a load cell on the hydraulic load fixture. The position of the EMA ram was measured by a digital encoder built into the motor and converted to a linear position by the driver (EMA Signal in Figure 6). These measurements permitted evaluation of dynamic control associated with the experiment in addition to EMAS abilities. More specific information such as images and technical details for each hardware, control, and DAQ device can be found in Appendix A.

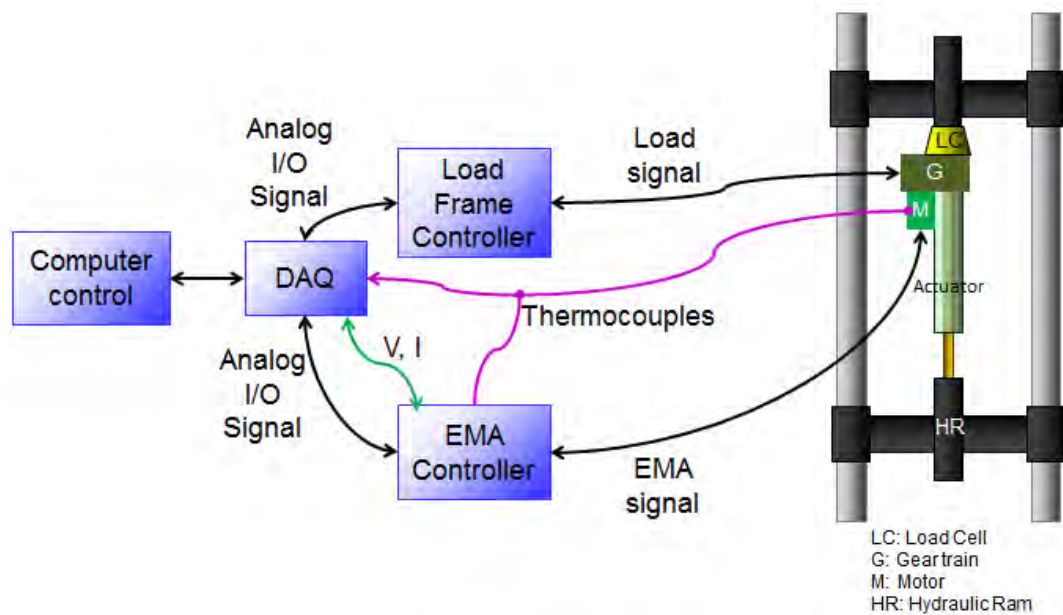


Figure 6 - Schematic of Experiment Test Setup

Characterizing Mechanical Hardware

The main hardware that is being used for the testing apparatus is a load fixture, in this case a MTS hydraulic load frame which is used to provide load to an EMA under evaluation. The force, displacement, and frequency parameters that were chosen were based on the NASA Dryden EPAD study. The stroke displacement from this study was 4.5 inches (114.3 mm), the max frequency dynamically that was 2 Hz, and the maximum load was 13,200 lbf (58,716 N) [4].

The press being used for the EMA test apparatus is an MTS 370.10 22KIP load frame with an MTS 661.20H-03 load cell operated by a Flex Test 60 controller. The software being used to operate the MTS press is Station Manager. In order to have a better understanding of our test equipment's capabilities, a series of tests were run to make sure that the hydraulic load frame was up to the standards needed for use in a simulated flight test profile.

Press frequency sweeps

Frequency sweeps were run without any filtering on the Press using 1500 N, and 13 kN. Figure 7 is the lab apparatus used in running the frequency sweeps of the MTS press. Two aluminum plates were bolted together with steel bolts, the top plate is threaded into the load cell while the bottom plate is threaded into the press hydraulic arm. This was set up so that a stiff specimen could be inside the load fixture (between the actuator arm of the load fixture and the load cell) in order to run force frequency sweeps and minimal displacement. The limiting factor for force would be the strength of the aluminum and the steel bolts. The frequency sweep test was done to confirm that the

hydraulic load fixture could reach loading frequencies that are normally subjected to an aircraft primary control surface.



Figure 7 - Hydraulic Press Frequency Sweep

Two aluminum plates were mated about their diameter by (4) ½ inch bolts/nuts. The equation for ½ inch bolt tensile stress area is:

$$A_s = 0.7854 [D - (0.9743/n)]^2 \quad (1)$$

Where A_s is the stress area (in sq.), D is the nominal bolt diameter in inch, and n is the number of threads per inch. Given $D = 0.5$ in and $n = 13$, the stress area is 0.14 in^2 , and the minimum tensile strength of $\frac{1}{2}$ inch bolt is 36000 psi. Since there are four bolts, the maximum calculated force that can be applied before failure of the bolts is 36,000 psi multiplied by the stress area which was 0.14 in^2 . This is then multiplied by the number of bolts which is four. The maximum force calculated was 20,160 lbf which is close to the maximum force of the load fixture, 22 kips.

Figure 8 is the frequency sweep resulting from a load of 1500 N. This plot shows that the load fixture follows the force sweep very well in the lower frequency portion of the profile then it gradually starts to overshoot the desired load as the frequency increases. Figure 9 demonstrates the tight force control of the hydraulic load fixture as the frequency increases from 0 to 2 Hz. At the end of the frequency sweep (near 39 Hz), Figure 10 shows that the control of the press has diminished because the overshooting amplitudes and becoming out of phase with the commanded input force.

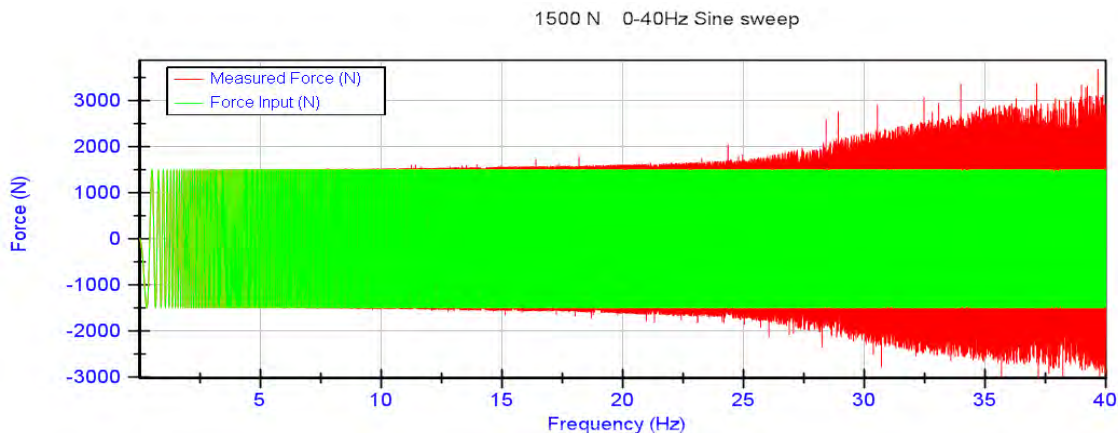


Figure 8 – 1500 N Frequency Sweep for Press

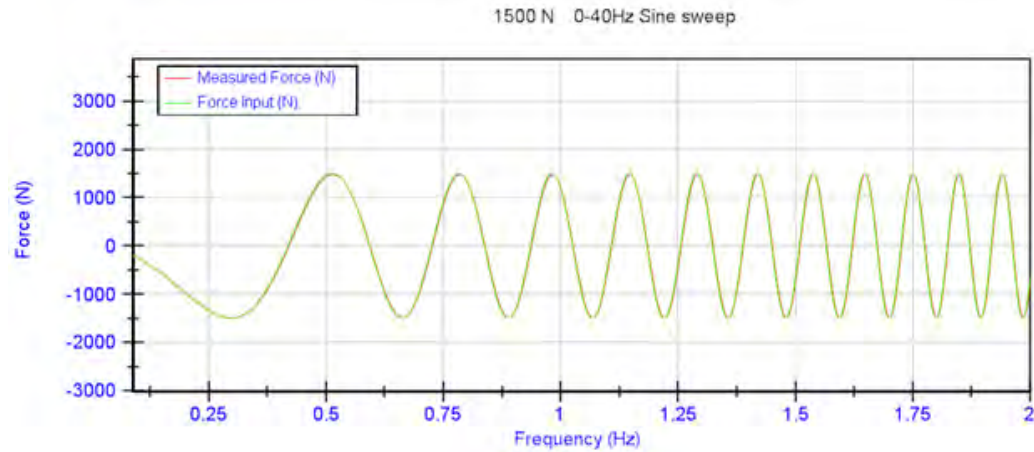


Figure 9 - Close up view of the first 2 Hz of the 1500 N frequency sweep

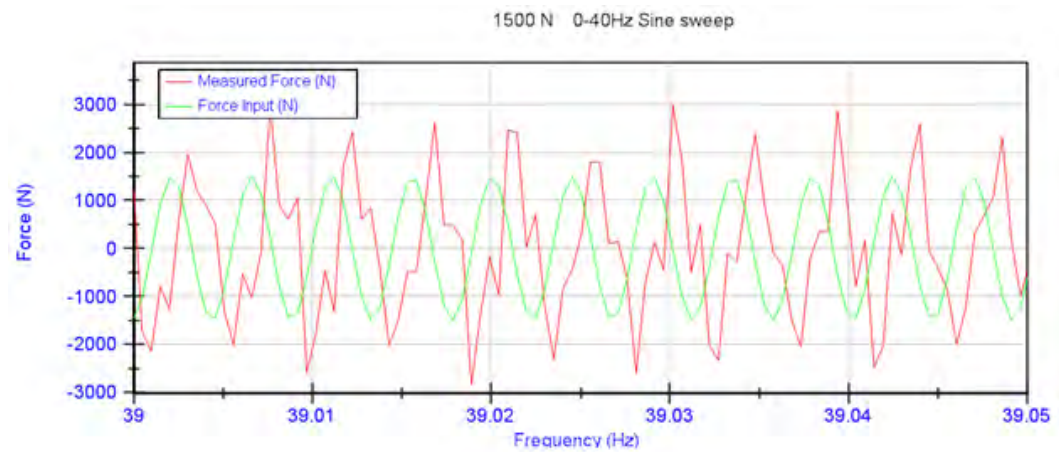


Figure 10 - Close up section near 39 Hz of the 1500 N frequency sweep

Figure 11 is a Bode Plot of the hydraulic load fixture frequency response under 1500 N. It shows that the response was 45° out of phase at approximately 13 Hz and reached 3 dB in magnitude at approximately 30 Hz.

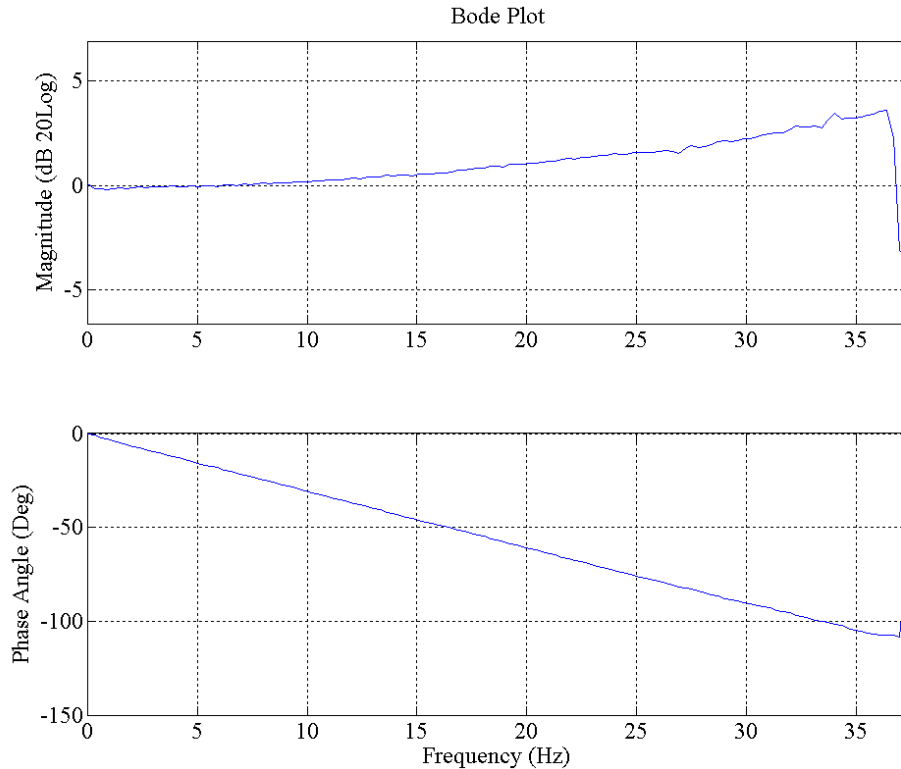


Figure 11 - Hydraulic Press Bode Plot at 1500 N

Figure 12, Figure 13, and Figure 14 are the frequency sweep result of the load fixture under a load of 13 kN. They show that the hydraulic load fixture follows the force sweep very well in the beginning of the sweep, but just like in the 1500 N sweep, the force control starts to degrade with increasing frequency. The test only went to 13 Hz because the test specimen (2 aluminum plates) was flexing and chattering, so the test was stopped for safety purposes.

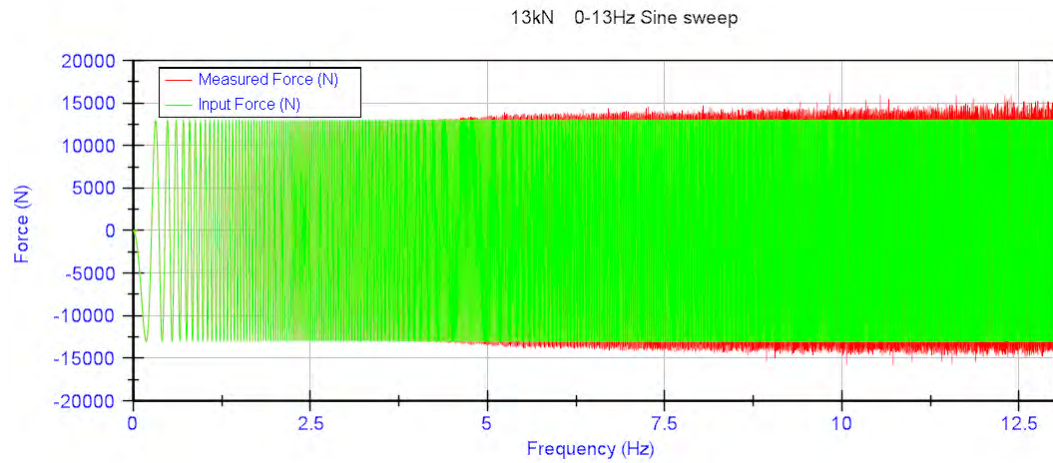


Figure 12 - Frequency sweep of press with 13 kN amplitudes

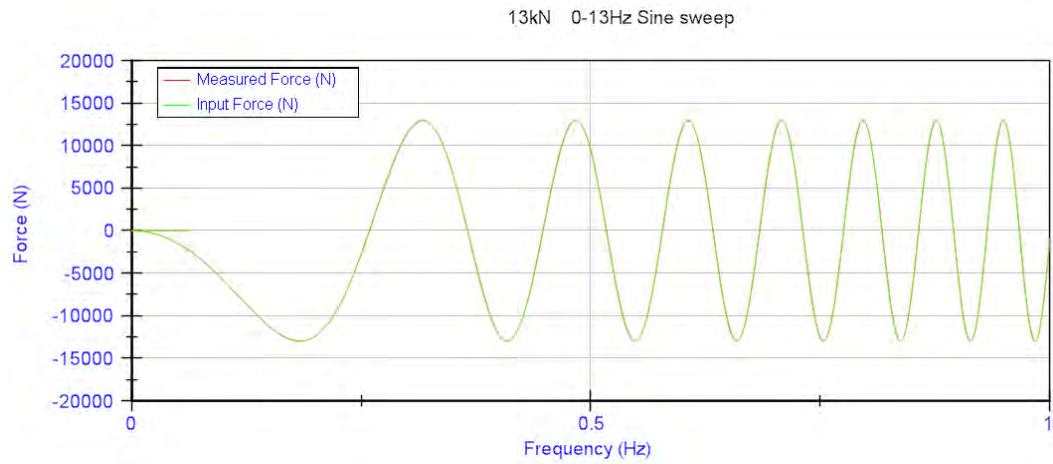


Figure 13 - Close up view of the first 1 Hz of the 13 kN frequency sweep

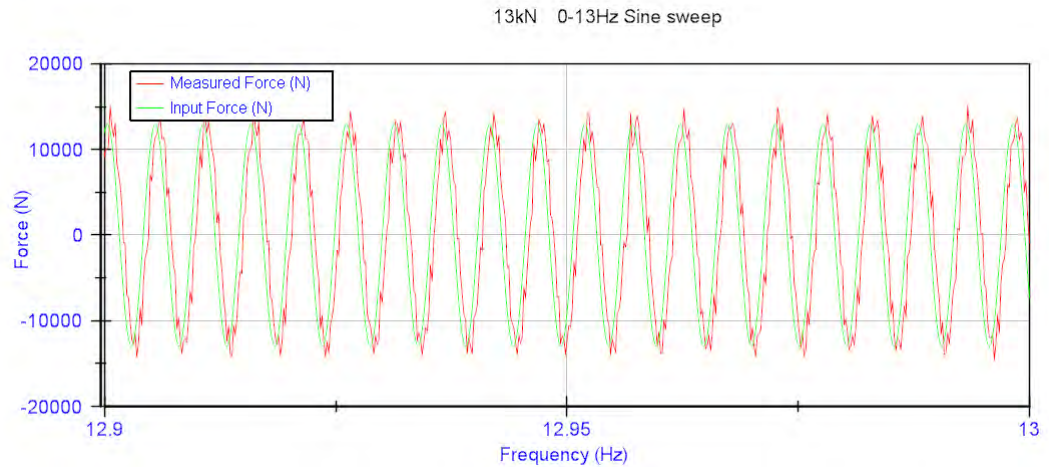


Figure 14 - Close up section at the end of the of the 13 kN frequency sweep

Figure 15 is a Bode Plot of the hydraulic load fixture response under 13 kN. It shows that the phase lag grew linearly from 0 to 35° near 12 Hz. The magnitude became erratic after 12.7 Hz.

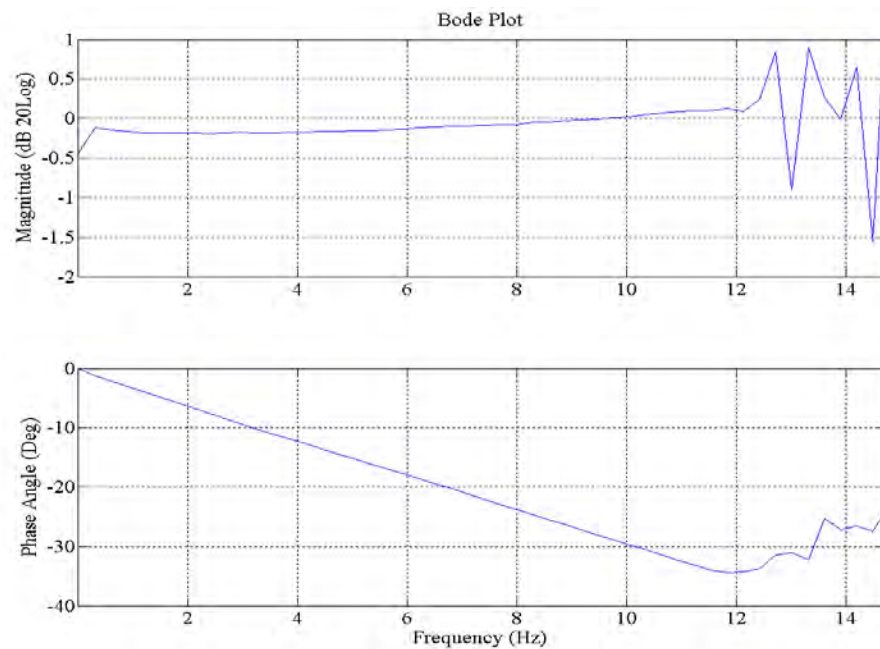


Figure 15 - Hydraulic Press Bode Plot 13 kN

Based on the two hydraulic load fixture frequency response tests, it was concluded that the hydraulic load fixture is capable of replicating dynamic force profiles up to 30 Hz at a 1500 N amplitude and up to 12 Hz at 13 kN. Both results are greater than typical mechanical frequencies experienced by an EMAS (10 Hz) and, therefore, substantiate the use of the hydraulic load fixture to replicate aerodynamic loads of a flight control surface.

Recording Mechanical Behavior

Actuator load, stroke, and temperatures of the motor winding and controllers are recorded to characterize the EMA's mechanical behavior. Aircraft flight control actuators have a frequency response of 6 Hz to 8 Hz. Future military fighters could have as high as 10 Hz frequency response rates. A sampling rate of 3000 samples per second was chosen for the actuator load and stroke. During testing, electrical disturbance was found, signal to noise ratio (SNR), on the stroke and force recorded signals. To mitigate the noise imposed on the mechanical signal, two 2nd order low pass filters were incorporated for stroke and force recorded signals. The filters were constructed with a cutoff frequency of 1000 Hz to eliminate high frequency content of the 16 kHz switching frequency from the IGBTs (Insulated Gate Bipolar Transistor) in the motor controller switchmode noise and the MTS Systems load frame controller chassis power supply noise, but not attenuate actual mechanical frequencies experienced by the actuator. The filters greatly improved the ratio of signal to noise information (Figure 16 and Figure 17).

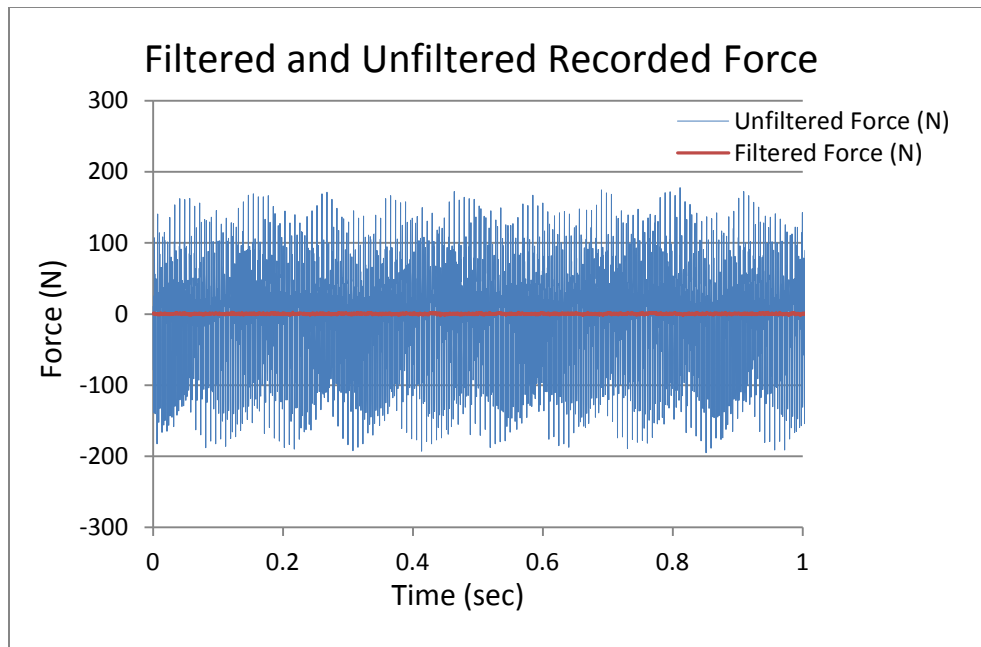


Figure 16 – Filtered Force Signal

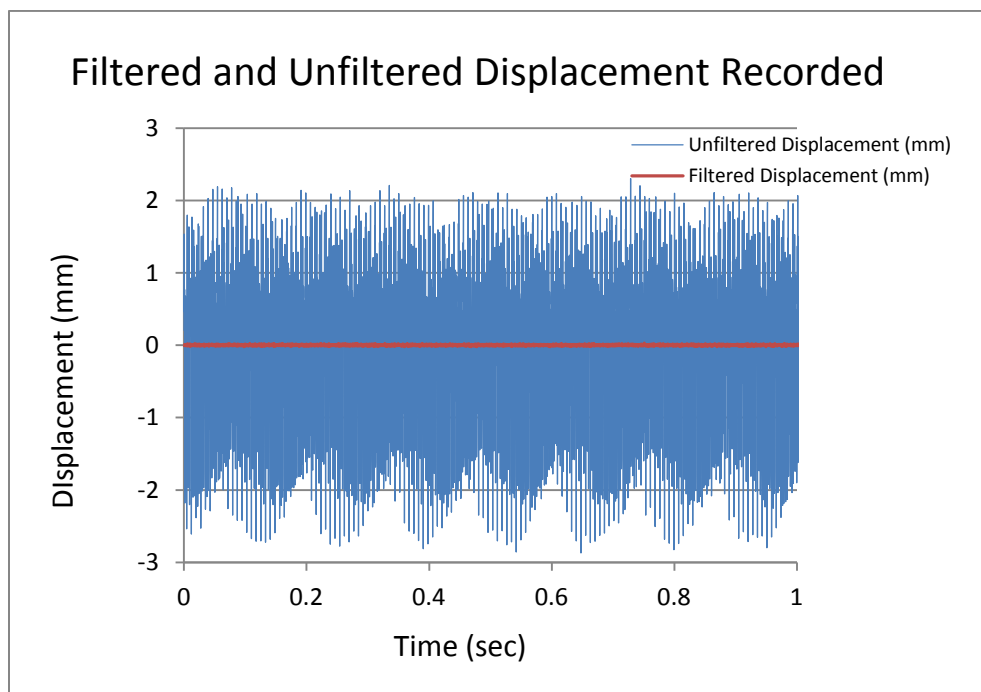


Figure 17 – Filtered Displacement Signal

Recording Thermal Behavior

Temperatures at various points in and on the motor were recorded. Because the motor has such a large thermal mass the temperature recording is a fairly low frequency task. However, we are interested in the temperature variation of small electrical components as well. These components have much less thermal mass resulting in a much higher rate of temperature change. Additionally, a number of the mechanical profiles are less than 10 seconds. In order to capture relevant thermal information over such a short test, the sampling rate would have to be less than 1 second. Therefore, a sampling frequency of 10 Hz was chosen for recording thermal data. The thermocouples for recording temperature were located at the motor's end turn winding for the three phases of the motor (which are expected to be the hottest spots inside the motor), motor surface, power electronics case, IGBT heat sink, transistor, regenerative power resistor, heat sink fin base, and environment surrounding the motor. Figure 18 and Figure 19 show the placement of these thermocouples in the motor and controller of the EMAS.

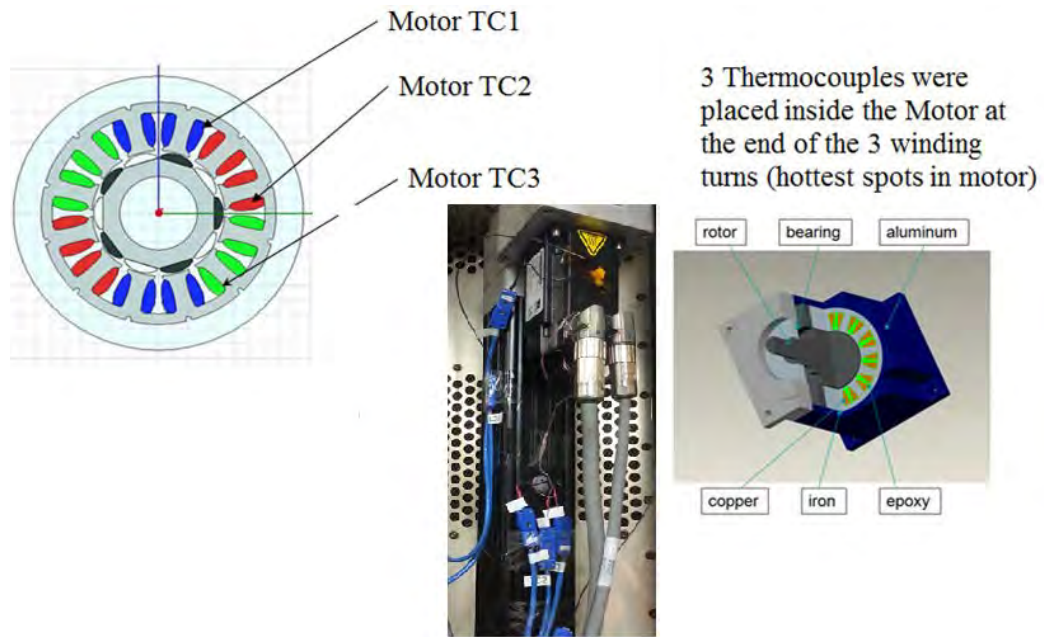


Figure 18 - Thermocouple Placement in the Motor of the EMAS [1]

Both servodrives were instrumented with thermocouples (TCs) on traditionally heat intensive components. Drive 1 in the dual drive setup functioned primarily as the EMA control generating a pulse width modulation (PWM) power to drive the EMA motor while Drive 2 provided 240 VAC mains supply rectification to 330 VDC. Figure 19 is an overview of thermocouple locations and their placement relative to the dual drive setup.

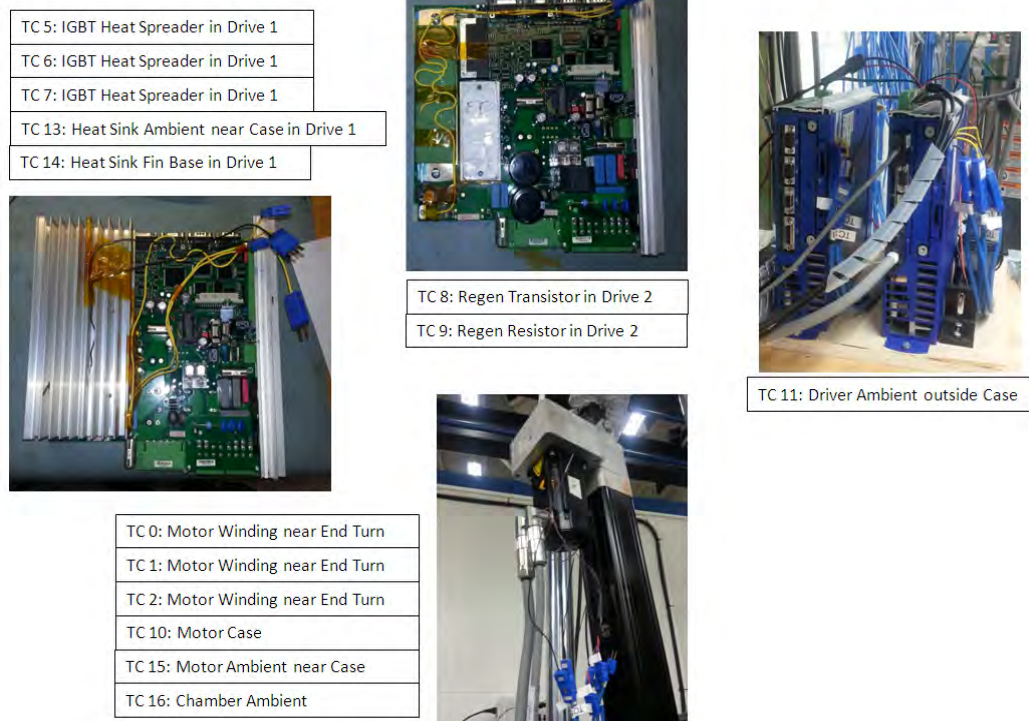


Figure 19 - Thermocouple Identification [1]

Drive 1's board was removed from its case, and the heat sink shown in Figure 20 was detached. The red rectangle highlights the heat spreader housing six primary IGBT switches. Points 5, 6, and 7 denote the location of TC 5: IGBT heat spreader, TC 6: IGBT heat spreader, and TC 7: IGBT heat spreader. TC 13 was placed in the center of the heat sink half the distance between the fin base and end. TC 13 has no contact with the heat sink and, therefore, was named TC 13: Heat sink ambient near case. TC 14: Heat sink fin base was placed in the same trough as TC 13 but in contact with the fin base.

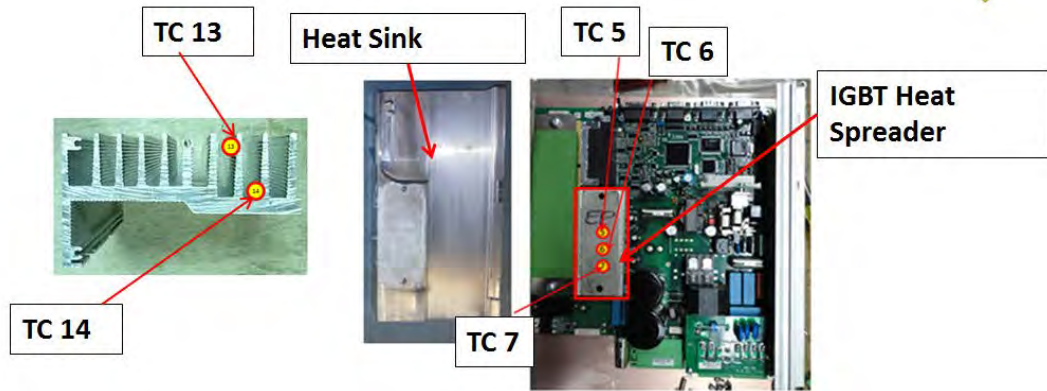


Figure 20 - Heat sink (left) and Servodrive board (Right) [1]

In order to reassemble the heat sink atop the heat spreader with thermocouples, three equally spaced trenches were machined into the heat sink. Figure 21 is a three dimensional design of the heat sink and the corresponding thermocouple trenches. Thermal compound was used near these locations to reduce thermal resistance between the heat spreader and heat sink.

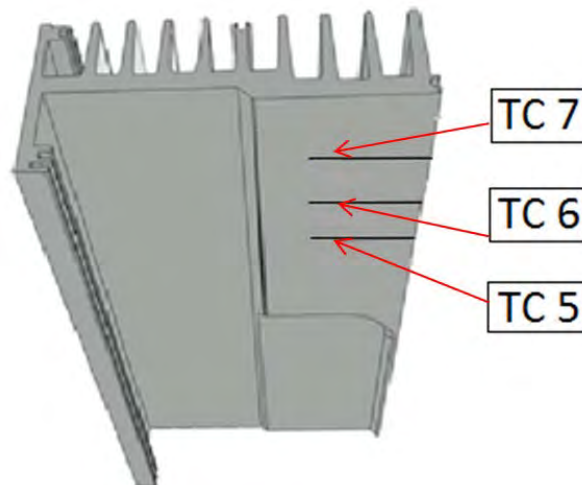


Figure 21 - Underside of heat sink with placement of thermocouples shown [1]

Figure 22 demonstrates the use of electrically insulated kapton tape to help route TC leads from the point of measurement to outside the driver case.



Figure 22 - Thermocouples embedded in Drive 1

Drive 2's board was removed from its case, and the heat sink shown in Figure 23 was detached. The red rectangle highlights the regenerative resistor ($33\ \Omega$), responsible for dissipating energy during regeneration. TC 9: Regen resistor was placed atop the regenerative resistor near the center of its longitudinal axis. TC 8: Regen Transistor was placed on the case of the transistor or switch responsible for opening and closing of the regenerative circuit. Figure 24 shows how TC 8 and 9 leads were molded for best fit and secured with kapton tape.

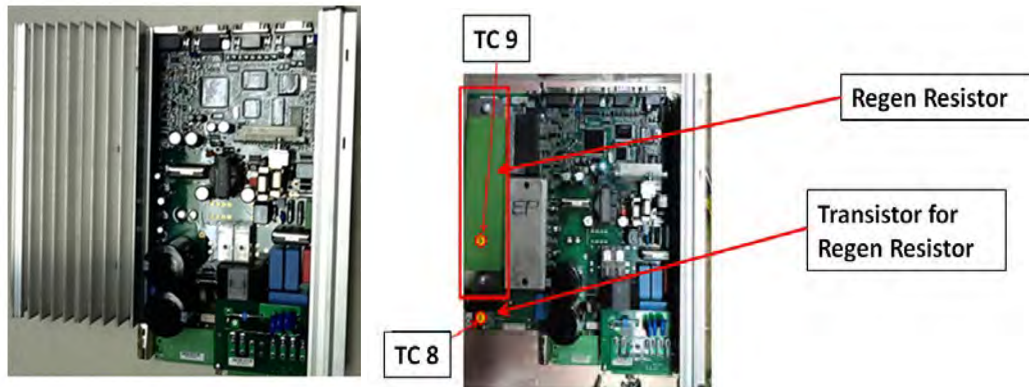


Figure 23 - Servodrive board with Heat Sink (left) and without Heat Sink (Right) [1]

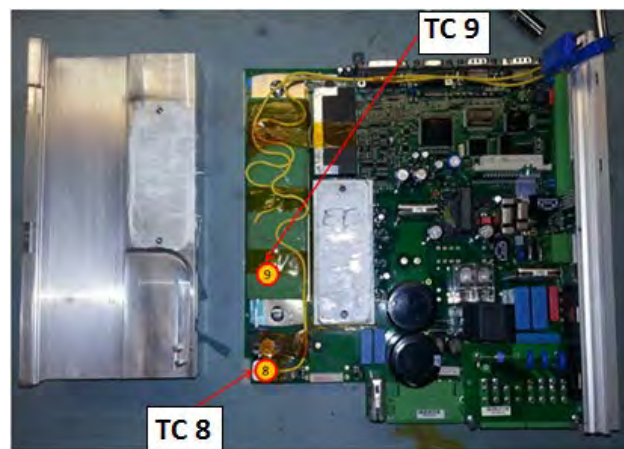


Figure 24 - Thermocouples embedded in Drive 2 [1]

Figure 25 shows the final result of drive fabrication for thermal instrumentation.



Figure 25 - Servodrive System Completed with Thermocouples [1]

High Speed DAQ

The term high speed DAQ system refers to components and methods used to record electrical data. Electrical measurements were made from the three phase lines leaving the controller and running to the EMA motor. Figure 26 shows more closely the method of measuring voltage and current on the three phase circuit to the motor. Current A and current B refer to the line current on two of the legs of the three phase circuit, legs A and B. Voltage A and B are line-to-line voltages of legs A and B with respect to the third leg, Leg C.

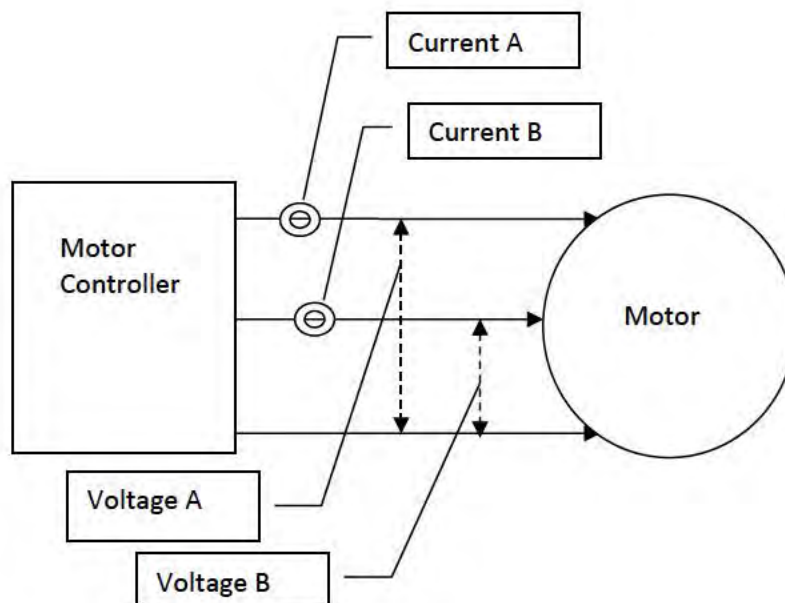


Figure 26 - Measurements made on 3 Motor Phases

Based on these measured values and the effective circuit containing a (balanced three phase) wye-connected motor, circuit analysis leads to total instantaneous power as the sum of instantaneous power on phase A and phase B [27]. This was the foundation for calculating electrical work done on the motor under a conservation of energy approach. Figure 27 is a diagram of the analogous circuit made up of the source (driver) and load (motor) and corresponding resistance of each phase. Utilizing Ohm's Law, Watt's Law, and Kirchhoff's voltage/current Laws, the Two Watt Meter Method can be derived for calculating total power in the circuit.

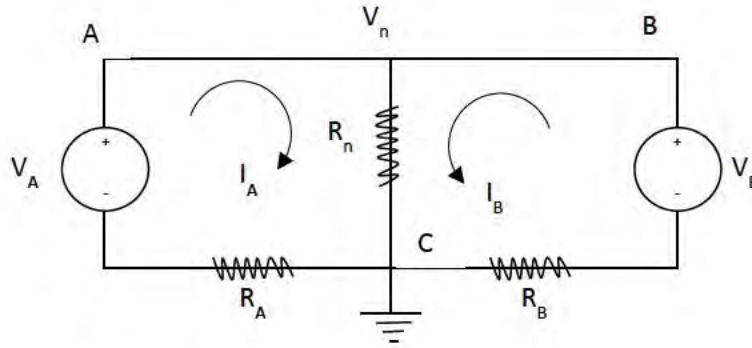


Figure 27 - Electrical Measurements

Ohm's Law:

$$V = IR \quad (1)$$

Watt's Law:

$$P = VI = \frac{V^2}{R} = I^2 R \quad (2)$$

Power dissipated across Resistor A:

$$P_{RA} = (V_A - V_n) * I_A \quad (3)$$

Power dissipated across Resistor B:

$$P_{RB} = (V_B - V_n) * I_B \quad (4)$$

Power dissipated across Resistor n:

$$P_{Rn} = V_n * I_n \quad (5)$$

From Kirchhoff's law, current on third leg is sum of current on other two legs:

$$I_n = I_A + I_B \quad (6)$$

Total power is the sum of power on each leg:

$$P_{tot} = P_{RA} + P_{RB} + P_{Rn} \quad (7)$$

Substituting equations 3, 4, and 5 gives:

$$P_{tot} = (V_A - V_n) * I_A + (V_B - V_n) * I_B + V_n * I_n \quad (8)$$

From equation 6, P_{tot} simplifies to:

$$P_{tot} = V_A * I_A + V_B * I_B \quad (9)$$

In addition to motor voltage and current, DC bus voltage and current were measured. The voltage and current were measured on the DC bus inside the controller to determine what power was being sent to the EMA motor during specific tests. The motor controller used for this experiment does not have access terminals for DC bus voltage and current measurement. Two identical controllers were modified in a daisy-chain fashion to gain access to bus voltage and current. A schematic of this set up can be shown in Figure 28 and Figure 29.

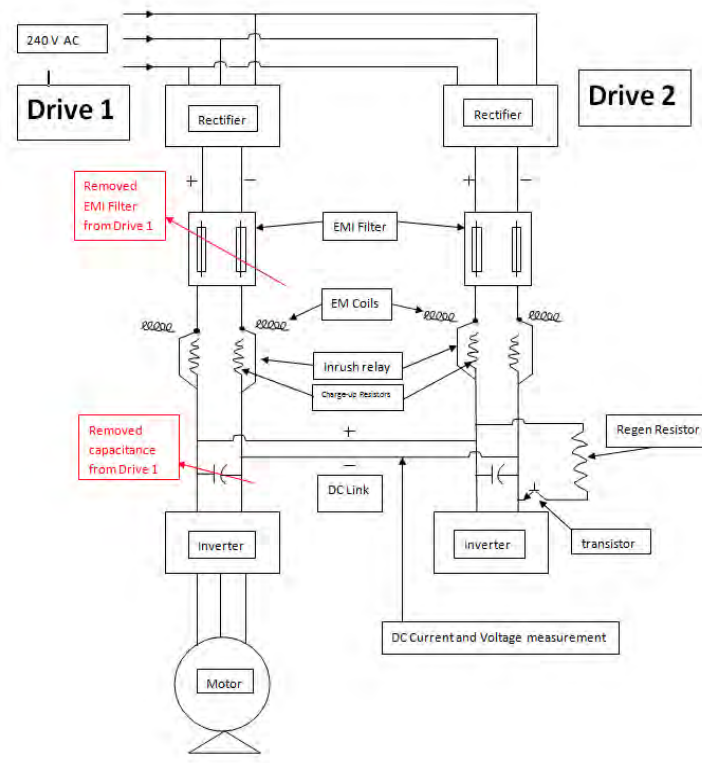


Figure 28 - Schematic for capturing DC bus current and voltage

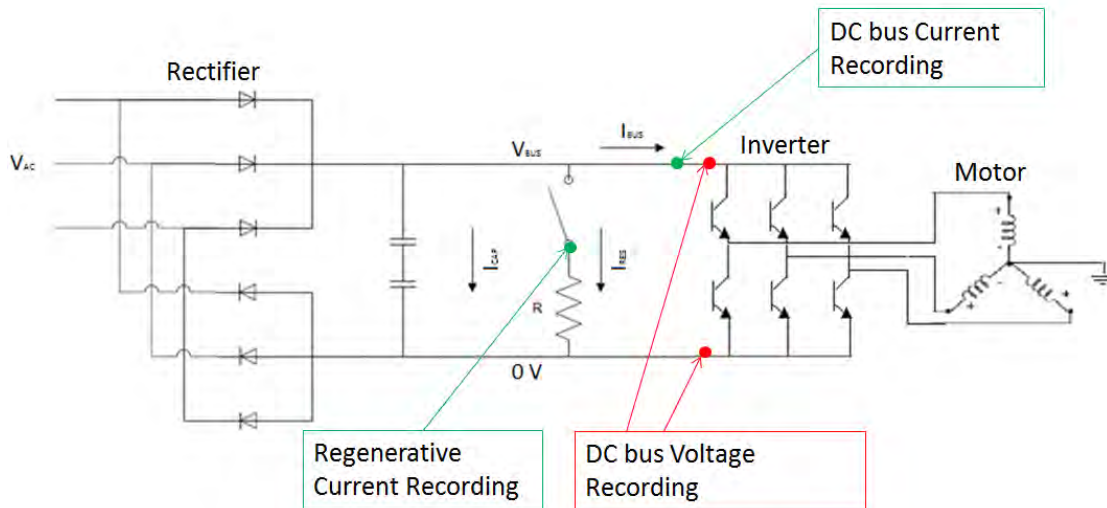


Figure 29 - Simplified Schematic of where DC current and voltage are being recorded

The electromagnetic interference (EMI) filter was removed from Drive 1 in order to sever the DC link so that the input voltage goes through the rectifier on Drive 2, down the DC bus on Drive 2 then back over to Drive 1, via the new external DC link, to be inverted and power the motor. The drives were set up this way in order to measure DC current and voltage across the DC bus as shown above. This method was required in order to “trick” Drive 1 into sensing that it was being powered via its input voltage and rectifier.) In order to capture any back flow of current from the motor, through the inverter, the capacitance was removed from Drive 1 to accommodate measurement between the capacitance and the inverter.

The BNC 2111 breakout board provided a connection between the output of the sensors and the input of the PXIe-6366 DAQ board. High speed DAQ operation was compiled in LabVIEW Control VI software which was responsible for sampling data at more than a sample every 1 ms so that transient electrical data could accurately recorded. Figure 30 outlines these components and their interactions for electrical measurements.

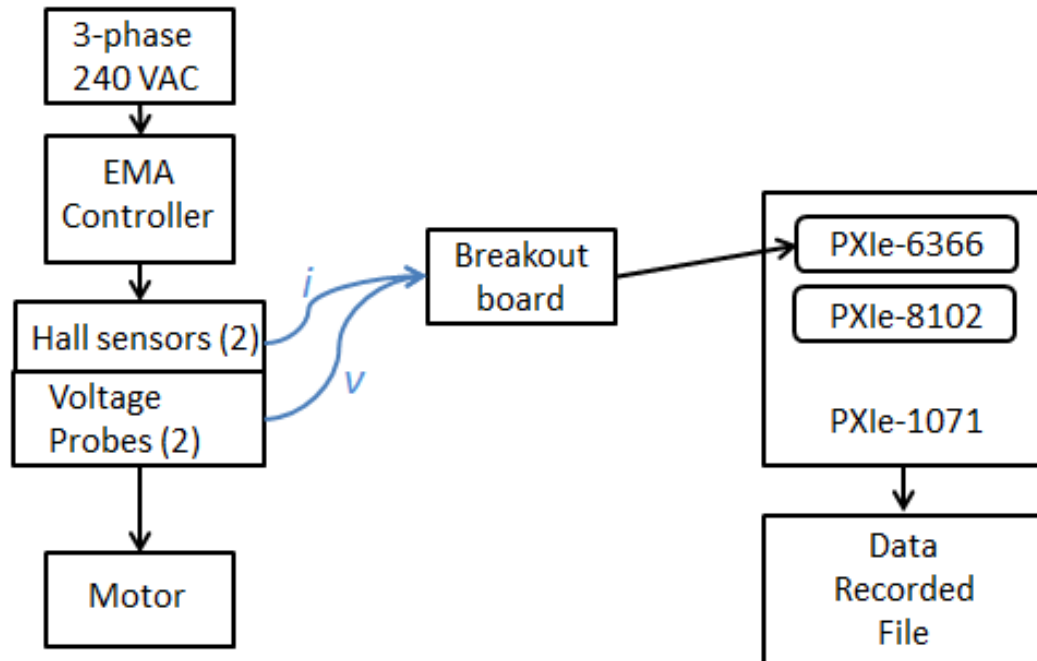


Figure 30 - High Speed Data Acquisition System

After testing and recording data with the current hall effect sensor on the EMA DC bus, it was found that high signal bandwidth measurement, specialized data processing algorithms, and dynamic sensor calibration are all required to accurately measure DC bus current. The combination of all these items was found not to be achievable within the scope of work for the project. Therefore, a search process was undertaken and a data logging power analyzer, Newton's 4th, was found with the needed capability. It had the best cost and schedule tradeoff for obtaining accurate, traceable measurements. The Newton's 4th power analyzer was connected to the external DC link created on the EMA drivers to record DC bus voltage and current during a test. The Newton's 4th ended up operating in three wattmeter configuration to achieve maximum data throughput. This data was stored on the internal flash memory of the power analyzer and then extracted with the use of a thumb drive.

Low Speed DAQ

Components and their interconnection to record temperature measurements are highlighted below in Figure 31. The low speed DAQ system is responsible for temperature measurement acquisition where data is being sampled at 10 Hz. A total of 12 type T thermocouples were used in this process. For the motor, there are three TCs inside the motor on the end turns of the windings, one TC on the motor case outer surface, and one TC in ambient near the motor case. There are seven TCs within the driver to measure the temperature of transistor, heat spreaders of regenerative resistor and IGBTs, and ambient air near motor drive heat sink. Thermal DAQ operation is compiled in the LabVIEW control block. Thermal data is recorded in a CSV format and saved to the NI machine. The low speed DAQ system includes a terminal block where the TC signal connections are organized.

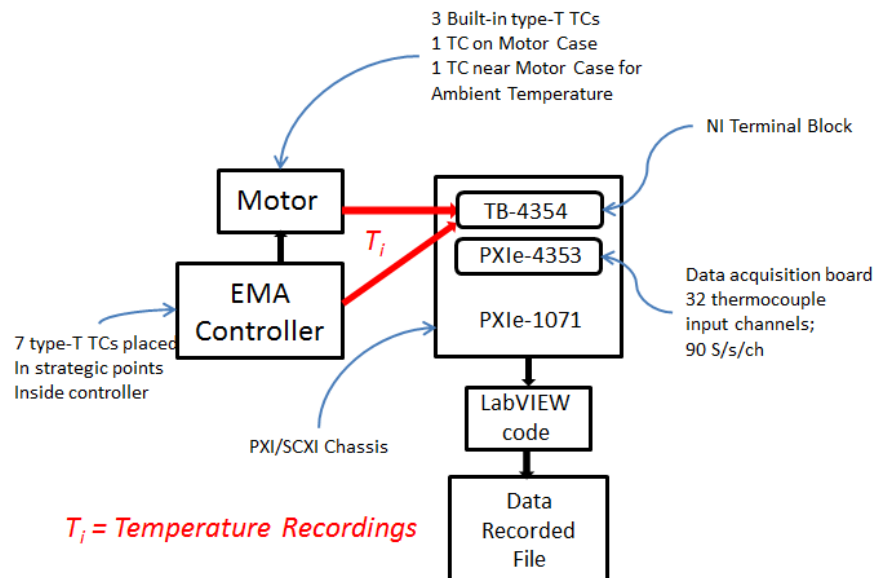


Figure 31 - Low Speed Acquisition System

CHAPTER 5

CALIBRATION AND UNCERTAINTY

Measurement uncertainties can come from the measuring instrument, from the item being measured, from the environment, from the operator, and from other sources [28]. To bound the uncertainty of the parameters, each measurement device, sensor, or transducer used for data collection was calibrated against a known input. Uncertainty analysis for all the measured and derived parameters was carried out.

For position measurement, four independent transducers are used, a linear variable differential transformer (LVDT) within the MTS load frame, an external LVDT fastened to actuator ram, an external dial fastened to actuator ram, and the motor's encoder. The MTS LVDT was calibrated by University of Dayton Research Institute (UDRI) personnel in 2014. It had a maximum uncertainty of ± 0.3 mm over a range of ± 140 mm. The external LVDT's specification sheet indicates a linearity of 0.45% over a linear range of ± 76.2 mm. This indicates that the external LVDT maximum uncertainty is ± 0.3429 mm. Linearity from the specification sheet was used because there was no other hardware in the lab that had ten times more accuracy than the linearity of the LVDT for the ± 76.2 mm range. The external dial and the motor position readout on the control screen were manually recorded in step response measurement. The external dial has a

readout resolution of 1/1000 inch. Its uncertainty, therefore, is ± 0.0127 mm. The motor position displayed on the control screen is in increments of 10 micrometers. Therefore, the motor position uncertainty in step response is ± 0.005 mm.

For load measurement, a load cell is attached to the MTS load frame. It was calibrated by UDRI personnel in 2014. Its uncertainty is ± 8.6 N force over a ± 4350 N range.

The voltage transducer is a Tektronix P5200 Voltage probe rated to 1300 V and providing 500X attenuation. The planned experiment includes nominal driver voltages of 320 VDC and possible spikes of 900 V. In order to quantify the voltage probe uncertainty, a calibration process was undertaken utilizing a high voltage DC source as power input and a high precision digital voltmeter as calibration standard. The high precision digital voltmeter is a HP 3456A Digital Voltmeter. Its uncertainty is $\pm 0.06\%$ of ± 899.5 VDC, which is ± 0.54 V. During the calibration, the output of the high DC voltage source was varied from -900VDC to 900VDC at increments of 50 VDC. The measurements of the DC voltage source output by both the voltage probe and HP3456A were recorded by a LabVIEW control program. At each calibration voltage, 1000 samples were recorded and averaged. This process was repeated 5 times at each fixed level of voltage. The maximum absolute error of the voltage probe against the HP voltmeter was 0.81 V. The overall maximum uncertainty of the voltage probe is the sum of the HP voltmeter error and the maximum curve fitting error, i.e. ± 0.54 V + ± 0.81 V = ± 1.35 V.

Current transducer is a LEM LA 55-P hall effect current transducer for measuring DC link current of the PMDC motor drive part of the electromechanical actuation system.

In order to quantify this current transducer uncertainty, a calibration process was undertaken which utilized a DC power supply, a resistor load bank, and a fluke multimeter. A power supply capable of 60Vdc and 50A was used to drive various levels of known current through a resistor load bank. The current was recorded by the transducer via a DAQ card and the fluke multimeter. The fluke multimeter, serving as the calibration standard, has an uncertainty of $\pm 0.5\%$ of ± 8.6 A, which is ± 0.043 A. During the calibration, current from the power supply was manually incremented by 0.5 A from -9.5 A to 9.5 A, and a LabVIEW control and measurement program was created to record transducer output and calculate average values. At each level of fixed current, the fluke multimeter output was recorded, 1000 samples of transducer output were recorded, and the average of those 1000 samples was calculated. This process was repeated 5 times at each fixed level of current. The maximum absolute error of the current transducer from the standard was 0.013 A. The overall maximum absolute error of the hall effect current transducer is the FLUKE Multimeter error plus the maximum transducer error, which ended up being ± 0.043 A + ± 0.013 A = ± 0.056 A.

Thermocouples for temperature measurement were calibrated with the use of a thermal bath and a high precision RTD which has an accuracy of $\pm 0.03^\circ\text{C}$. All of the thermocouples were placed around the RTD in close proximity to minimize errors. The bath was commanded to reach temperatures between 0°C to 100°C at 5 degree intervals. Once the RTD read that the bath temperature reached equilibrium, the thermocouples were recorded. This process was initiated for the increasing temperature curve, from 0 to 100°C , and for the decreasing temperature curve, from 100 to 0°C to identify any hysteresis errors. The maximum difference between the RTD reading and the

thermocouples' calibration curve fitting over the temperature range of 0 °C to 100 °C is ± 0.14 °C. The overall uncertainty the thermocouples is the sum of RTD uncertainty and the thermocouples' maximum curve fitting error, ± 0.03 °C + ± 0.14 °C = ± 0.2 °C .

A Newton's 4th Power Analyzer was used in order to record transient electrical data on the DC bus. The power analyzer has a data collection rate of 2.2Ms/sec and a data logging rate of 500 Hz. Over a voltage range of ± 1000 V rms, there is an accuracy of ± 0.836 V and over a current range ± 10 A rms there is an accuracy of ± 0.0088 A. Table 1 summarizes the uncertainties.

Table 1 - Summary of measurement uncertainty

Measurement	Range	Uncertainty
Load	± 4350 N	± 8.6 N
MTS Displacement LVDT	± 140 mm	± 0.3 mm
External LVDT	± 63.5 mm	± 0.529 mm
External Dial	± 12.7 mm	± 0.0127 mm
Voltage	± 900 V	± 1.35 V
Current	± 9.5 A	± 0.056 A
Temperature	0 °C to 100 °C	± 0.2 °C
Motor Encoder	360° rotation	$\pm 0.17^\circ$
Voltage by Newton's 4 th Power Analyzer	± 1000 V rms	± 0.836 V
Current by Newton's 4 th Power Analyzer	± 10 A rms	± 0.0088 A

CHAPTER 6

TEST RESULTS

Backlash

A large backlash of an aircraft's flight control actuators could have detrimental effects on flutter stability in the control surfaces due to reduced stiffness caused by backlash. As a result, backlash of flight control actuators cannot exceed user specified percentage of full stroke. To measure the backlash of an EMA, an external measurement device is directly attached to the side of the EMA. The external measurement device used here is a Teclock Corporation Dial Indicator with a resolution of 0.001" (0.0254 mm). The EMA is coupled to the hydraulic press and commanded to hold a fixed position while the hydraulic press applies a step input force against the EMA to push and pull the EMA. Because of this force, the EMA arm moves slightly up and down because of the backlash in the system and gear train. These results of the external measurement device attached to the EMA and the motor position from the motor driver software were recorded. The motor position from the driver software was recorded so that when subtracting the motor position from the measurement of the external measuring device, the backlash due to the gear train can be accurately calculated without incorporating the

motor slippage into the measurement. Figure 32 below is an example of the backlash test force profile that was applied to the static EMA.

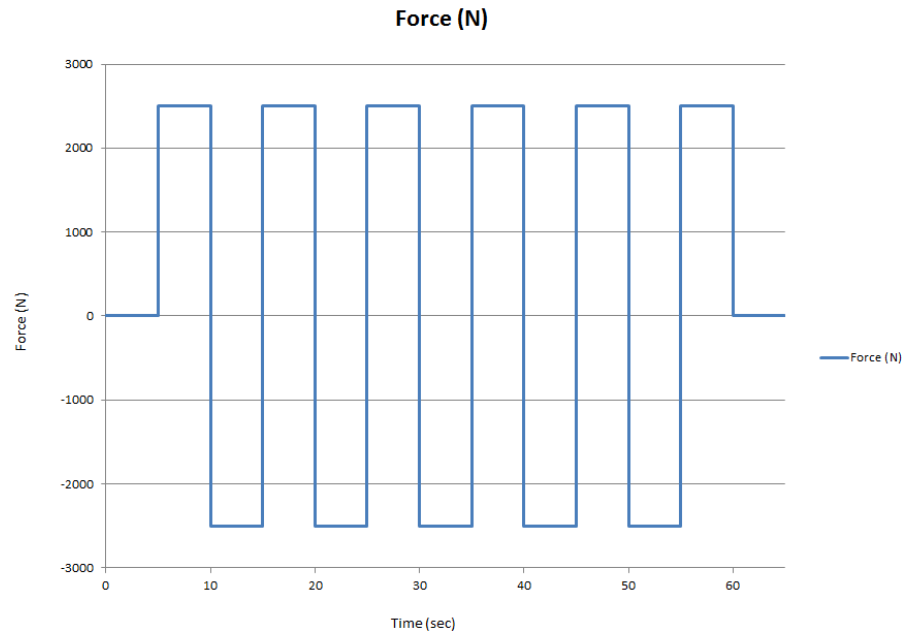


Figure 32 - Backlash Test Force Profile

Figure 33 shows the setup for backlash measurement. An independent measurement device was affixed securely to the side of the EMA and a rigid aluminum plate was positioned between the clevis end of the EMA and the cylinder portion of the arm so as to have a flat surface for the measurement device to measure position. This method was used in order to eliminate any displacement due to slop in the top and bottom clevis connections of the EMA so that only ‘true’ backlash in the gear train of the actuator is recorded. The EMA was connected to the press and commanded to hold a ‘zero’ position through a command of ‘zero’ velocity, to avoid jittering of the EMA which would result from a position command. While the EMA was holding still, the press followed a step force profile. The movement of the EMA ram due to the backlash was measured by the measurement device affixed to the EMA and was recorded by hand.

The magnitude of the applied force was chosen to be 200 N, 1000 N, and 2500 N. The EMA was installed vertically, the weight of EMA's ram and gear train is 45 lbf and equivalent to 200 N force, this force was used for the first loaded test to simulate a no load backlash condition. 2500 N is just less than the motor's maximum continuous load so that the measured EMA ram movement was solely due to backlash. These values simulated a very low load, medium load, and 32% motor stall load. Any slippage of the motor was recorded with the use of the EMA driver software and subtracted from the recording of the external measurement device attached to the EMA. Figure 34, Figure 35, and Figure 36 show the measurement readings at the three loads.



Figure 33 - Backlash Test Set-up

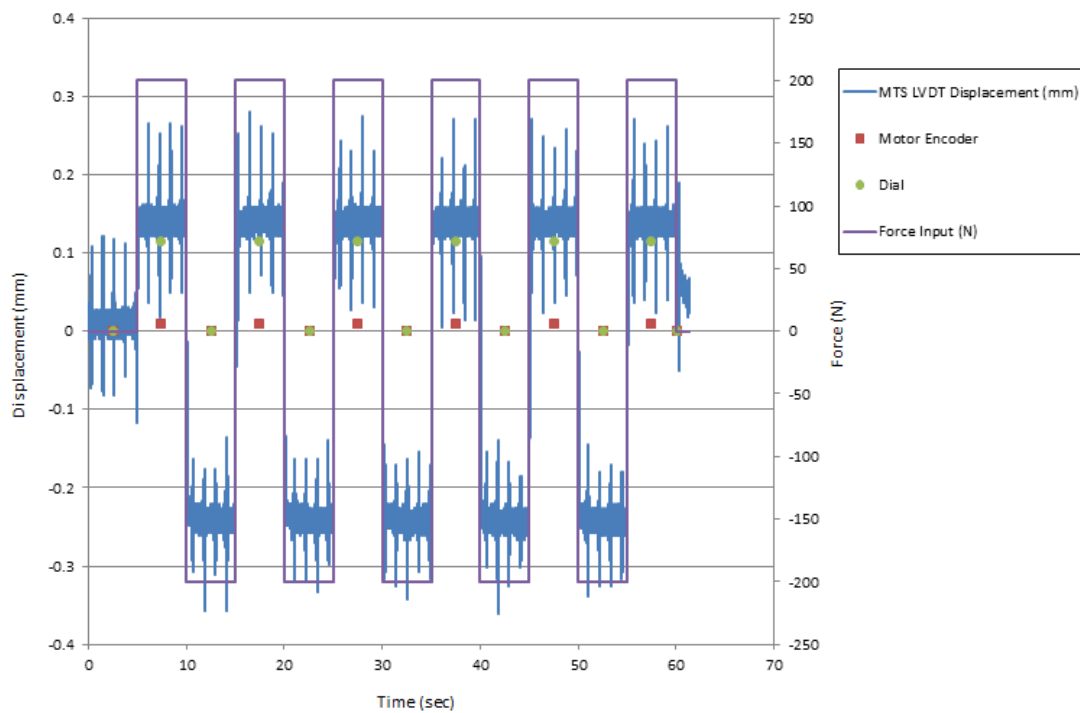


Figure 34 - Backlash Test Results under 200N Alternate Load

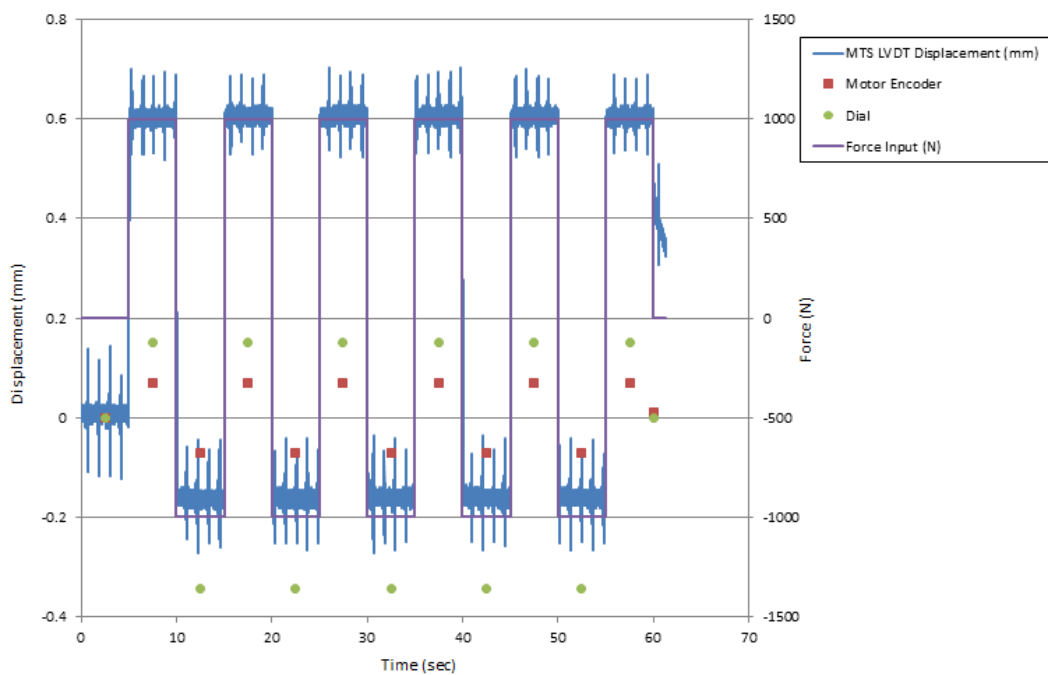


Figure 35 - Backlash Test Result under 1000N Alternate Load

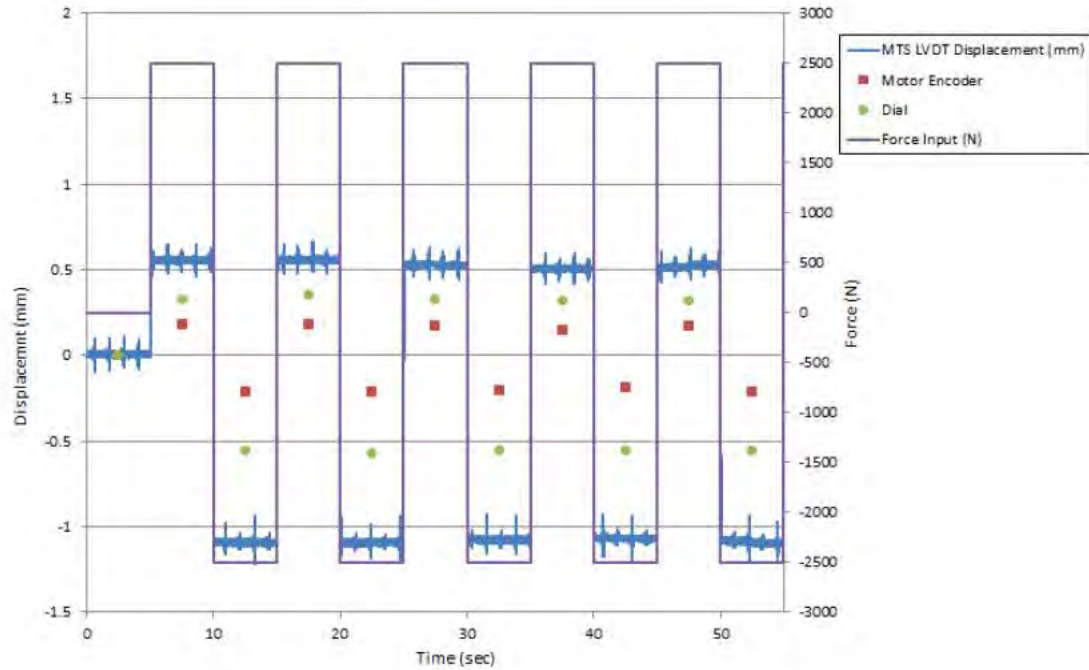


Figure 36 - Backlash Test Result under 2500 N Alternate load, 50% of motor's stall load

Figure 34 shows that the minimal backlash in the gear train is 0.104 mm. This is understandable because the gear train is made up of helical gears which produce backlash. When the EMA was under loads of 1000N and 2500N, the backlash increased to 0.355 mm and 0.499 mm respectively. This is expected, as higher forces cause higher elastic deformation of the actuator's linkage and, therefore, larger backlash. Table 2 are the results of the backlash testing. The error bar of the backlash is $\pm 0.0177\text{mm}$, $\pm 0.0127\text{mm}$ from the dial readout uncertainty and $\pm 0.005\text{mm}$ from the actuator's encoder readout uncertainty.

Table 2 - Backlash of EMA gear train under varying loads

Load (N)	± 200	± 1000	± 2500
Backlash (mm)	0.104	0.355	0.499
Backlash (%full stroke)	0.03%	0.12%	0.16%

Step Response

The step response test determined the overshoot, settling time, and rising time of the actuator for a given step command input. The overshoot was defined as the difference between the overshoot actuator stroke and the commanded stroke, in percentage of the commanded stroke. The settling time is the time from applied step command to the point where the actuator crosses the user specified percentage error band for the last time. The rising time is defined as the time required for 10% to 90% of the step stroke. Figure 37 depicts the definition of those three parameters. The evaluator will flag if the overshoot, settling time, and rising time are greater than user specified values.

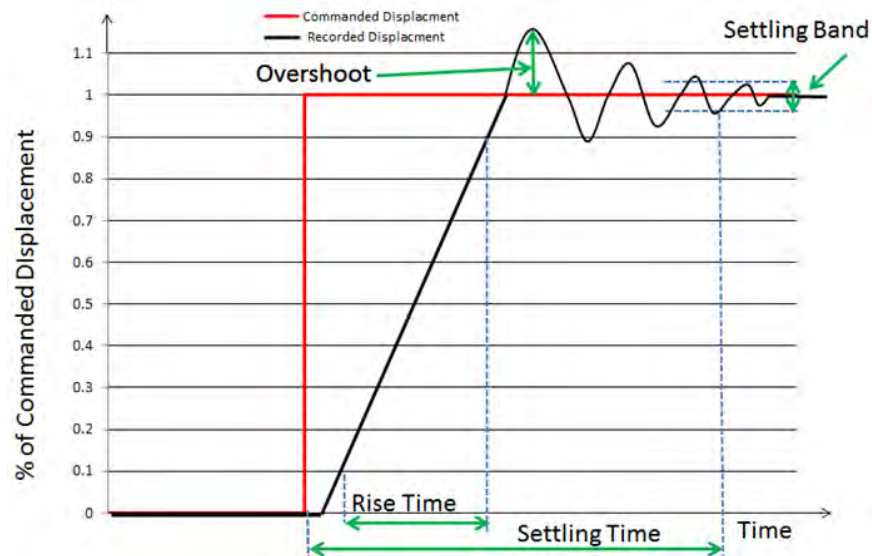


Figure 37- Definition of Overshoot, settling time, and rising time from a Step Response

A step response test was run on the Danaher EMA with mechanical and electrical data collected. Instead of a single step input, double steps back-to-back were commanded in a square wave form to also evaluate the power characteristics of the step response. Sufficient time between the two steps is allocated to decouple the interference

between them. The step amplitude is 127 mm, 40% of the actuator's full stroke. Figure 38 is the step response input, measured position, and measured velocity. The result from the first step was used to determine the rise time, overshoot, and settling time.

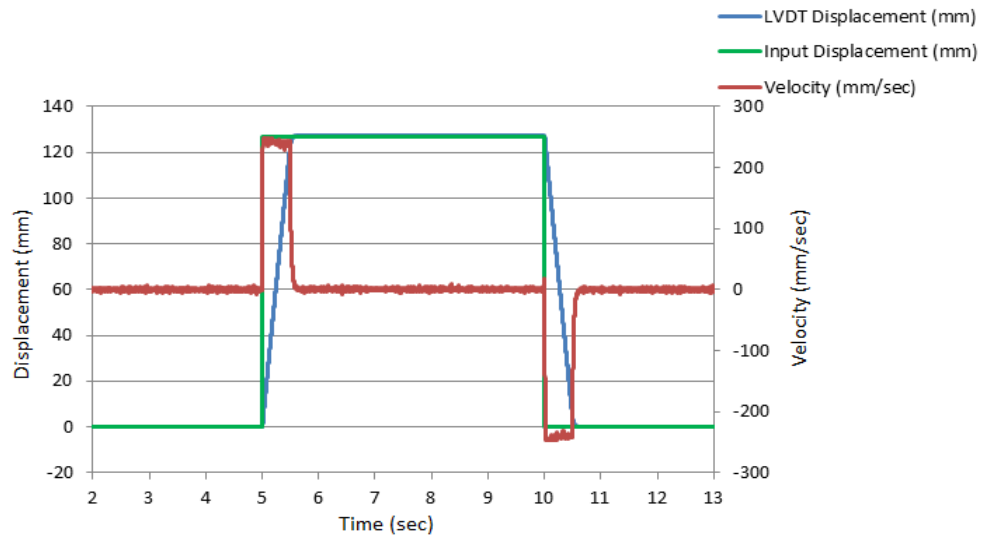


Figure 38-Mechanical Step Response Results

Figure 39 and Figure 40 are a close ups of the step response and depicts data for the rise time, settling time, and overshoot of the EMA for the step response portion of the test where the EMA is extending downward. The rise time of the EMA for this particular step response test was 0.408 seconds, and the settling time of the EMA is 0.517 seconds (Figure 39). There was not an overshoot for the EMA on this particular step response test. The recorded overshoot was 0.12% of the commanded 127 mm displacement (Figure 40).

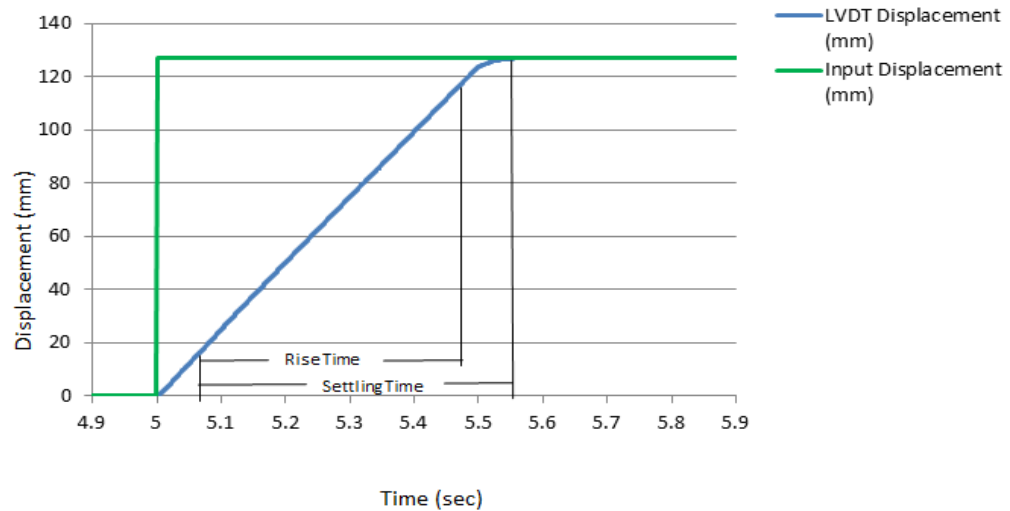


Figure 39 - Rise Time and Settling Time of Step Response

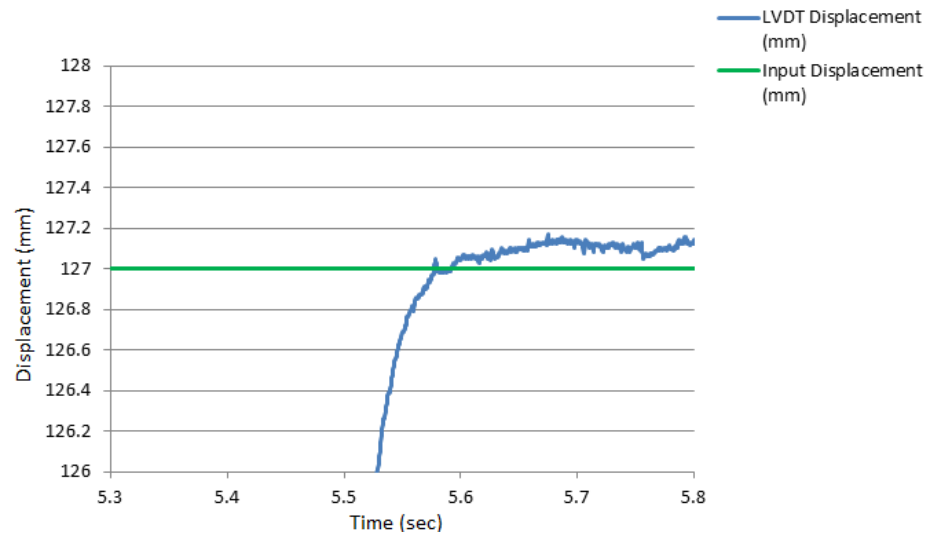


Figure 40 - Overshoot of Step Response

Figure 41 and Figure 42 are close ups of the step response and depicts data for the rise time, settling time, and overshoot of the EMA for the step response portion of the test where the EMA is retracting upward. The rise time of the EMA for this particular step response test was 0.407 seconds and the settling time of the EMA is 0.59 seconds. There was no overshoot for the EMA on this particular step response test.

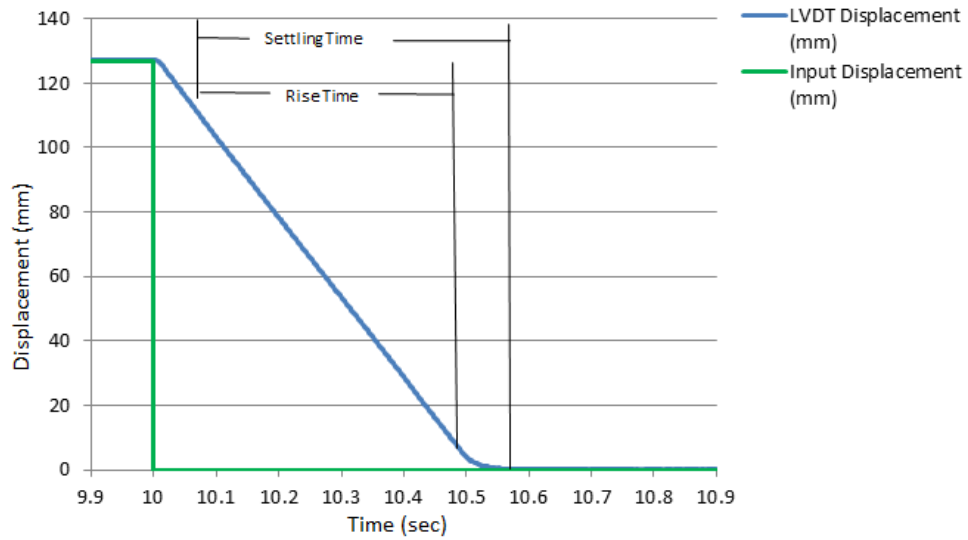


Figure 41-Rise Time and Settling Time of Step Response

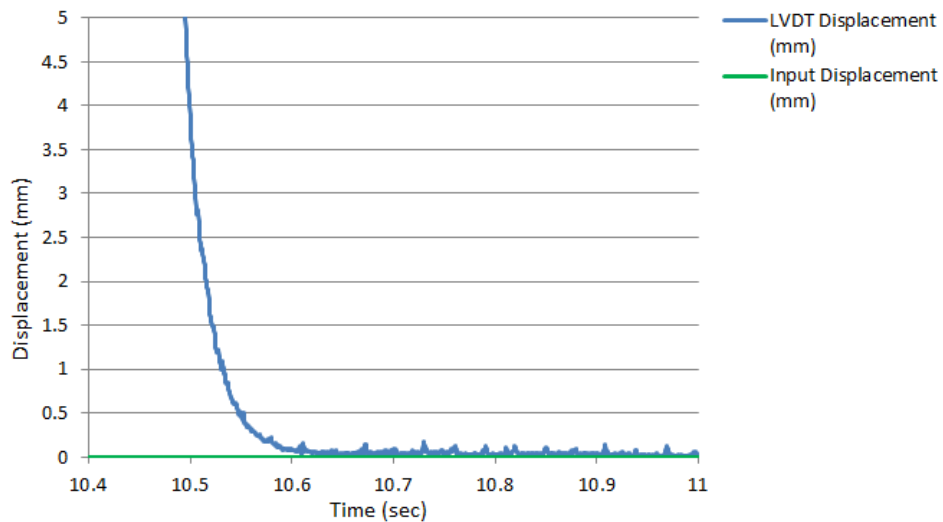


Figure 42-Settling Time of Step Response

The step response test also revealed the electric power characteristics of the actuator.

Figure 43 below displays the DC bus voltage and DC bus current collected with the Newton's 4th Power Analyzer. The transient spikes in current and voltage are shown at points in the step response test. Here, the EMA actuator arm travels at maximum velocity from a stationary position to the next commanded position. The first peak in current

correlates to the inrush of power to accelerate the motor at maximum velocity in order to reach the commanded displacement. The corresponding bus peak power is 2181 watts at ten seconds as shown in Figure 44. At the onset of the motion, the bus voltage dropped suddenly due to a sudden current draw. The third and larger peak of voltage occurs when the motor stops because the EMA actuator arm has reached the commanded position. This voltage rise on the DC bus is caused by regenerative energy being placed back onto the DC bus due to inertial rotation of the motor as it is decelerating from maximum speed of 4660 rpm to a stop. In turn, the motor becomes a generator for a brief period of time. The peak regenerative power is 713.7 watts shown in Figure 44. The voltage corresponding to the peak regen energy is 389 V, 59 volts higher than the nominal bus voltage of 330 V, an 18% increase. The corresponding current is 3.53 A, this current should be negative. However, the bus current was recorded by the power analyzer as an rms value. Thus, it is always recorded as positive.

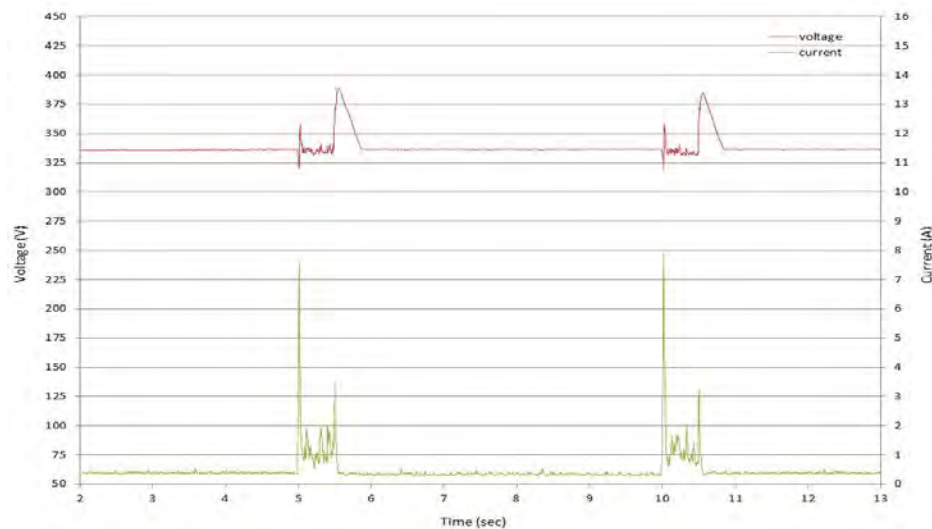


Figure 43 – DC bus Voltage and Current Data from Step Response

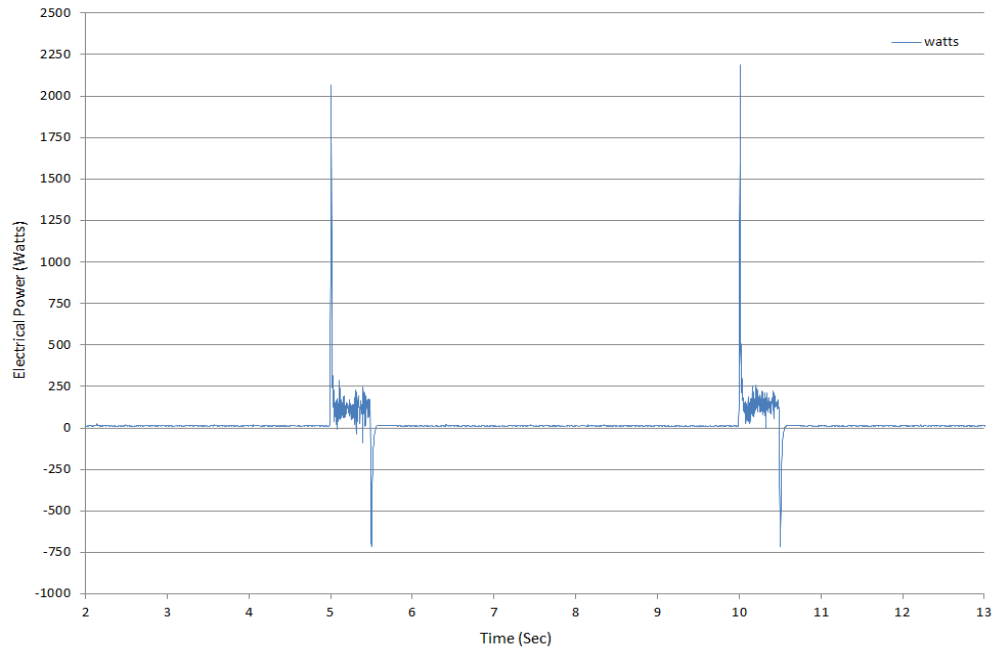


Figure 44 - DC Bus Electrical Power in Step Response Test

In order to record the regenerative current going to the resistor during the step response test, the leads that were recording the DC bus current were attached to the jumper to the regenerative resistor on the back of the controller to record the regenerative current. Then the same step response test was rerun. Figure 45 below shows the recorded DC bus voltage and regenerative resistor current recorded. The DC bus voltage is identical to the DC bus voltage in Figure 43, indicating the repeatability of the test. The regenerative resistor current is only occurred during regenerative portions of the step response test, where there is a voltage rise on the DC bus and the capacitance on the regen circuit have been filled to capacity. Figure 46 is the power dissipated through the resistor.

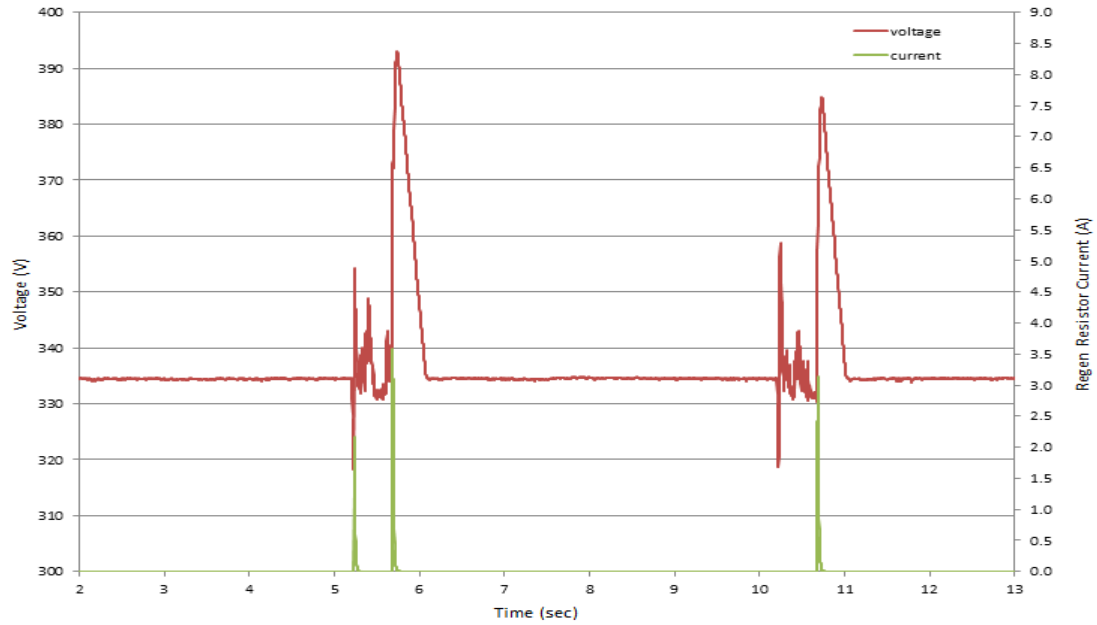


Figure 45 - DC bus Voltage and Regen Resistor Current Data from Step Response

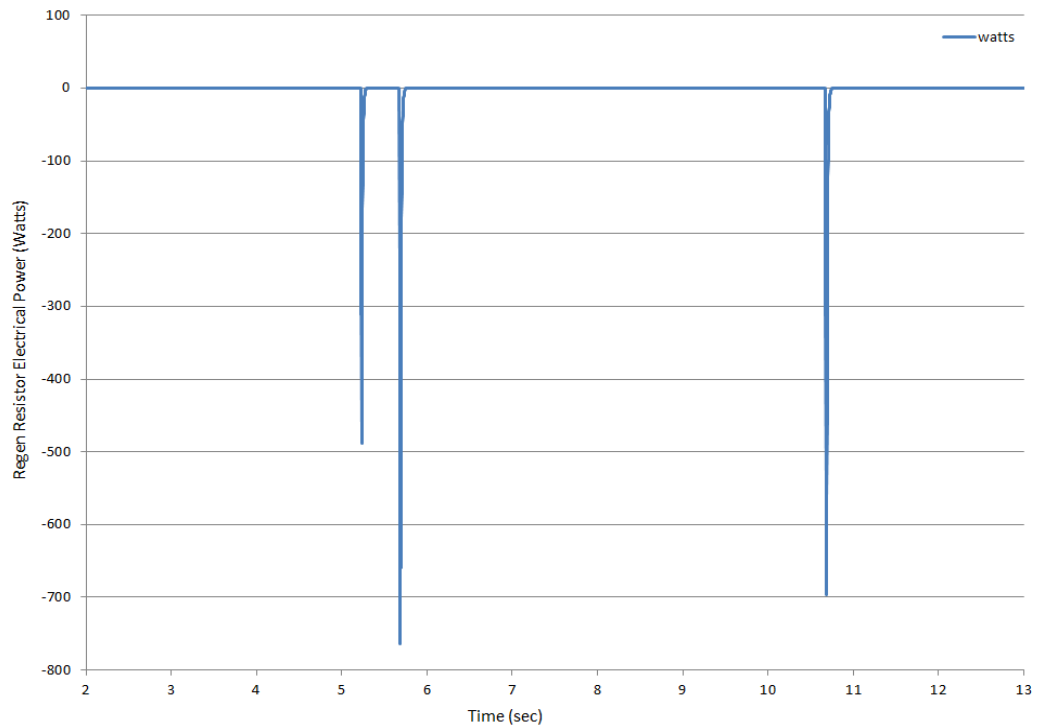


Figure 46 - Electrical Power in Watts Recorded on the Regen Resistor

During the regenerative mode of the motor, the regenerative energy first goes to the bus capacitor on the regen circuit, causing the rise of the bus voltage. When the bus voltage on the capacitor reaches a design threshold, the regenerative energy, in the form of current, is sent to the regenerative resistor where the regenerative electric energy is converted to heat. To quantitatively calculate the regenerative energy, a method based on the measured bus voltage and current across the regenerative resistor is derived. The regenerative period is defined as the time the bus voltage rises. Regenerative energy stored in the bus capacitor was calculated based on the initial and end bus voltage during the regenerative period and the capacitor size. Regenerative energy is dissipated by the resistor was calculated based on the measured power across the resistor. The following is an example how the regenerative energy from the deceleration of the actuator in the step response was calculated.

Figure 47 shows the bus voltage and regenerative resistor current of the second regenerative event from the deceleration of the actuator. The time interval at which the voltage rise occurs on the DC bus during this regenerative portion of the step response was used to calculate the regen energy stored in the capacitors. The regenerative energy is dissipated by the regenerative resistor is calculated by integrating the recorded regenerative resistor power over time (Figure 48).

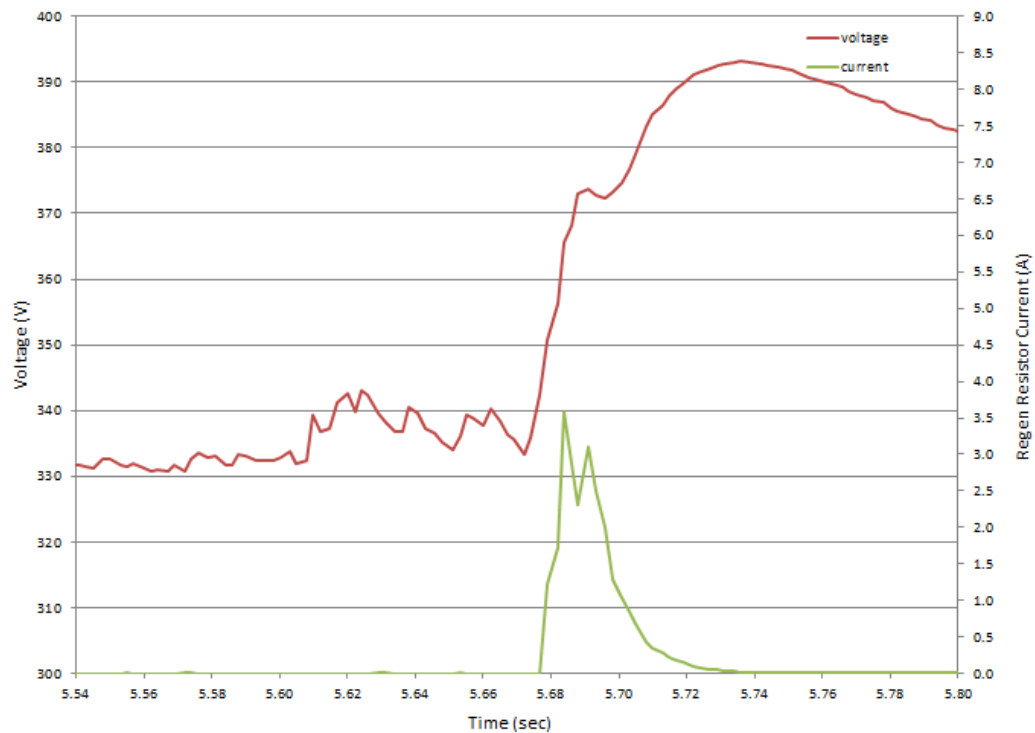


Figure 47 - Regenerative Portion of the Step Response Test Recorded By the Power Analyzer

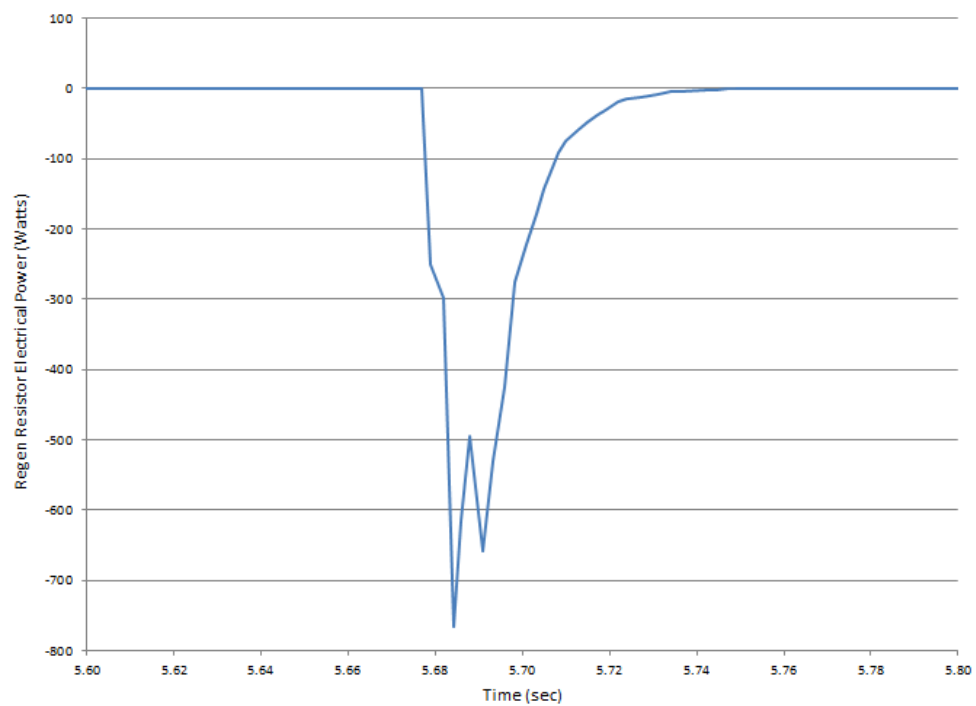


Figure 48 –Electrical Power in Watts Recorded on the Regenerative Resistor

Calculating the electrical energy stored in the capacitors and the energy dissipated from the regenerative resistor during the voltage rise and comparing it to the calculated mechanical energy of the EMA actuator, the EMA's electric and mechanical power characteristics were quantified.

First, the energy stored in a capacitor can be estimated:

$$U_C = \frac{1}{2} C_T * V^2 \quad (1)$$

where U_C is the Energy stored in a capacitor in Joules, C_T is the Total capacitance on regen circuit in Farads, (0.000235 Farads in this case), and V is the DC bus voltage.

The DC bus voltage at the onset of the regenerative event, V_1 , is taken from 5.61 seconds in Figure 47 (333 V). This voltage is used to calculate the capacitor's initial stored energy. The bus voltage at the end of the regenerative period, V_2 , is 388V, shown as the peak at 5.74 seconds in Figure 47. Therefore, the regenerative energy stored in the capacitor is the capacitor's energy rise over the period of voltage rise:

$$\Delta U_C = U_{C2} - U_{C1} = \frac{1}{2} C_T (V_2^2 - V_1^2) \quad (2)$$

$$\Delta U_C = \frac{1}{2} (0.000235 \text{ Farad}) (388^2 - 333^2) \quad (3)$$

$$\Delta U_C = 4.67 \text{ Joules} \quad (4)$$

The regenerative energy when a current flows on the regenerative resistor and is dissipated starts at time $t_{R1} = 5.68$ seconds. This event ends at the time when the DC bus voltage reaches its peak and starts to drift downward and as the regen resistor current approaches zero, which is $t_{R2} = 5.73$ seconds. These time events are shown in Figure 48.

Energy dissipated by the regenerative resistor:

$$U_R = \sum_{i=t_{R1}}^{t_{R2}} \frac{(P_{i+1} + P_i) * (t_{i+1} - t_i)}{2} \quad (5)$$

$$U_R = 12.37 \text{ Joules} \quad (6)$$

where U_R is the energy dissipates on the regen resistor in Joules, P is the measured electrical power in watts from the regen resistor (Figure 48), t is time, t_{R2} is the time at which DC bus voltage reaches its peak ($t_{R2} = 5.73$ seconds), t_{R1} is the time at which DC bus voltage starts to rise ($t_{R1} = 5.68$ seconds).

The total Regenerative electrical energy:

$$U_{Total} = \Delta U_c + U_R \quad (7)$$

$$U_{Total} = 17.03 \text{ Joules} \quad (8)$$

Below are the equations for characterizing the mechanical energy for the EMA system during the regenerative event in the step response test.

The motor rotor inertia (J_{motor}) is given by:

$$J_{motor} = 0.000145 \text{ kg-m}^2 \quad (9)$$

The rotation of the motor (ω):

$$\omega = \text{Max velocity} = 485.9 \text{ radians/second} \quad (10)$$

The energy represented as the motor rotor inertia (E_{motor}) term:

$$E_{motor} = \frac{1}{2} J_{motor} * \omega^2 \quad (11)$$

$$E_{motor} = 17.24 \text{ Joules} \quad (12)$$

The calculated mechanical energy is only 0.09 Joules more than the regenerative electrical energy which is plausible because of the mechanical and electrical efficiency losses in the geartrain, motor, and controller.

Reversal Test

A reversal test commands the EMA under no-load to move half of its full stroke at a specified slew rate, reverse direction, move a full stroke, and then reverse half of its full stroke back to the starting position. The reversal test will evaluate the EMAs' position accuracy under no load.

In the test, the actuator arm was commanded a 50% max velocity rate of 125 mm/second from a specified zero position to a position of 68.5 mm stroke outward, retract 127 mm, and then back to mid-stroke specified position. This evaluation examines the actuator position and speed accuracy. The transient electric power of the actuator is also evaluated. The recorded velocity is used to determine when steady-state power should be evaluated and the interval over which the peak power should be integrated to determine peak energy delivered. Figure 49 below is the position input of the reversal test. The actuator was mounted vertically with the ram pointing downward. Positive displacement means the actuator extending downward.

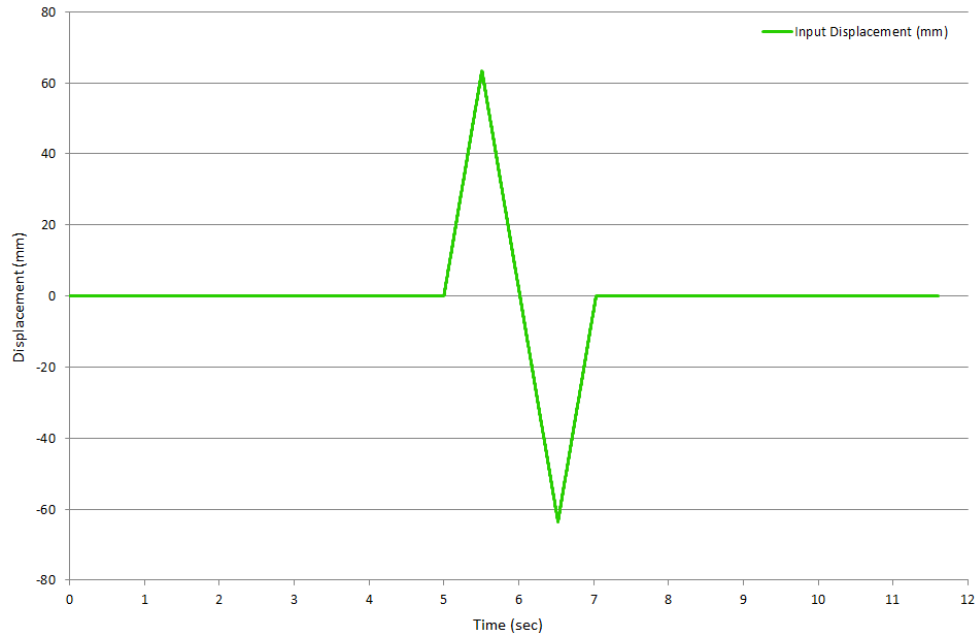


Figure 49 - Commanded Displacement for the Reversal Test

Figure 50 below is the recorded position and rate of the reversal test. From the recorded rate, it is observed that the EMA initially overshoots the commanded rate each time there is a directional change for the EMA displacement. As soon as the EMA overshoots the commanded position, the EMA quickly adjusts its rate to the commanded rate of 125 mm/second. This specifies that the actuator always starts at maximum rate and then adjusts to the commanded rate. This control mechanism will have an impact on the regenerative energy as shown later. Figure 51 and Figure 52 are enlargements of regions of Figure 50. At each point of position reversal, the actuator overshoots and a maximum rate is deployed briefly to correct the position, and then return to commanded rate.

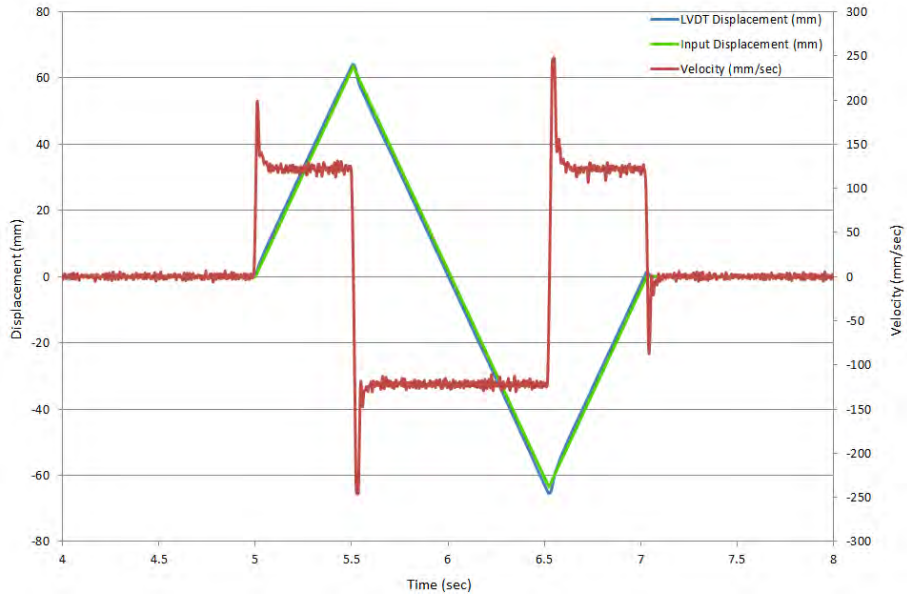


Figure 50-Mechanical Reversal Results

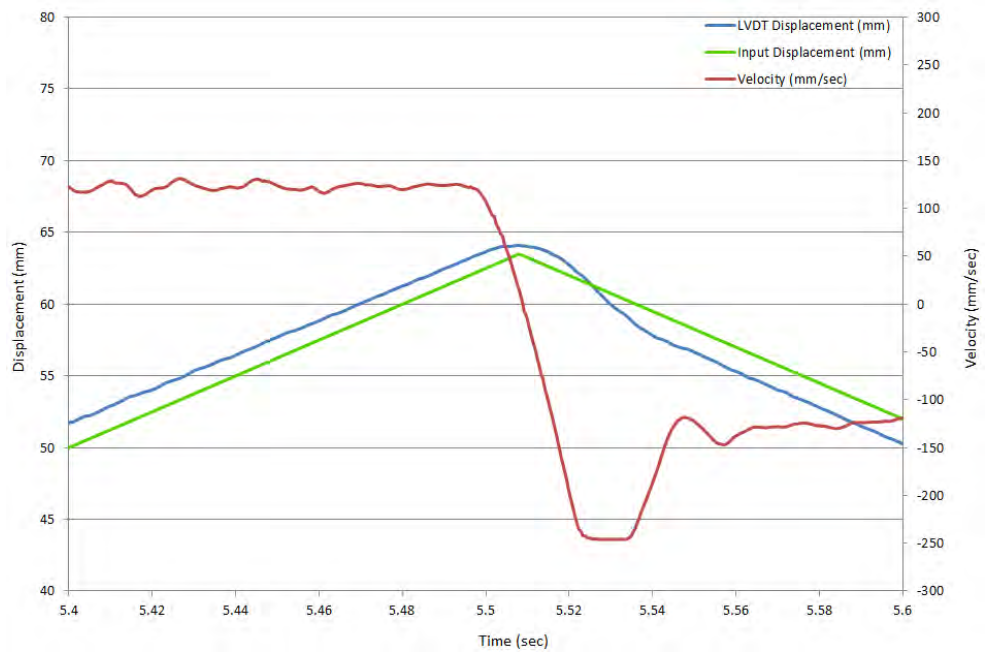


Figure 51 - Close up of first reversal

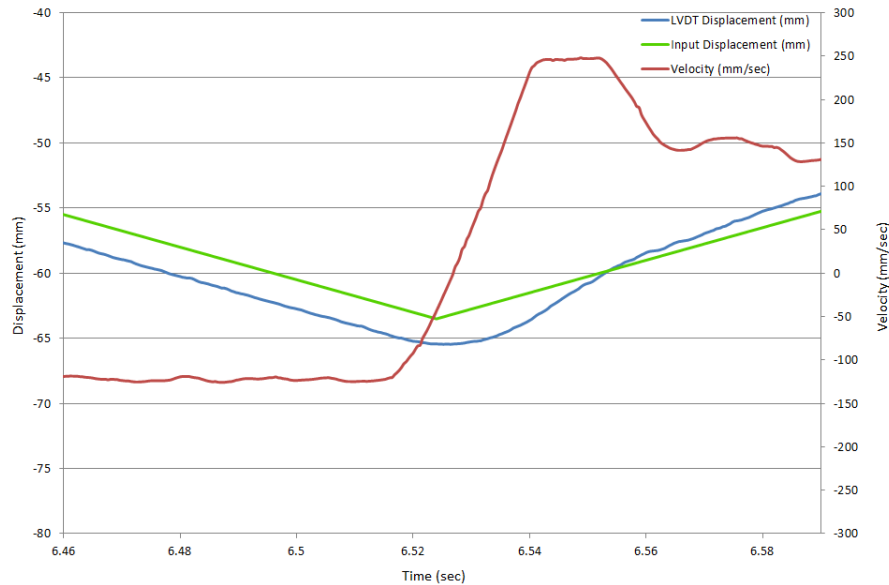


Figure 52 - Close up of second reversal

Figure 53 displays the DC bus voltage and current collected with the Newton's 4th Power Analyzer for the reversal test. The transient spikes in current and voltage occur where the EMA actuator arm starts traveling to a commanded position or it reverses directions to the next commanded position. Figure 54 displays the electrical power recorded on the DC bus during the reversal test. The first peak of electrical power is the power draw when the motor begins rotating. The second peak in power is a small regenerative peak which is due to the motor decelerating from 200 mm/second to the commanded rate of 125 mm/second after over shooting when the motor started rotating (Figure 50). The third peak in power is a regenerative peak as the motor quickly decelerated from 125 mm/second to a rate of zero in order to reverse directions (Figure 50). The fourth peak in power resulted from the motor drawing power to immediately rotate at the commanded rate (Figure 50). The fifth peak in power is regenerative power from overshooting to the maximum rate of -250 mm/second and having to decelerate to

the commanded rate of 125 mm/second (Figure 50). The sixth peak in power is a regenerative peak as the motor quickly decelerated from 125 mm/second to a rate of zero in order to reverse directions. The seventh peak in power resulted from the motor drawing power in order to immediately rotate at the commanded rate of 125 mm/second (Figure 50). The eighth peak in power represents the regenerative power from overshooting to the maximum rate of 250 mm/second and then decelerating to the commanded rate of 125 mm/second (Figure 50). The ninth peak in power is a regenerative peak as the motor quickly decelerated to a rate of zero.

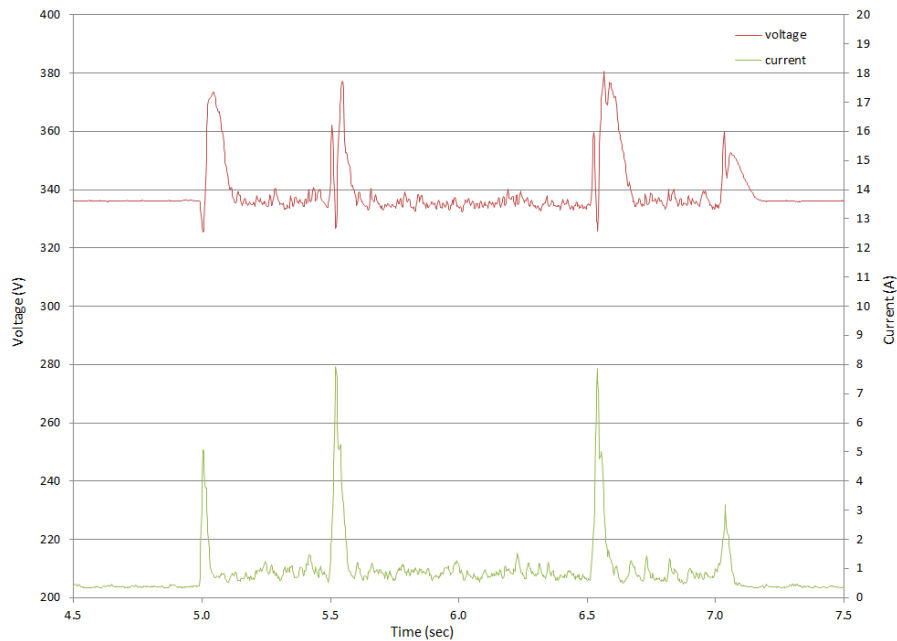


Figure 53 - DC bus Voltage and Current

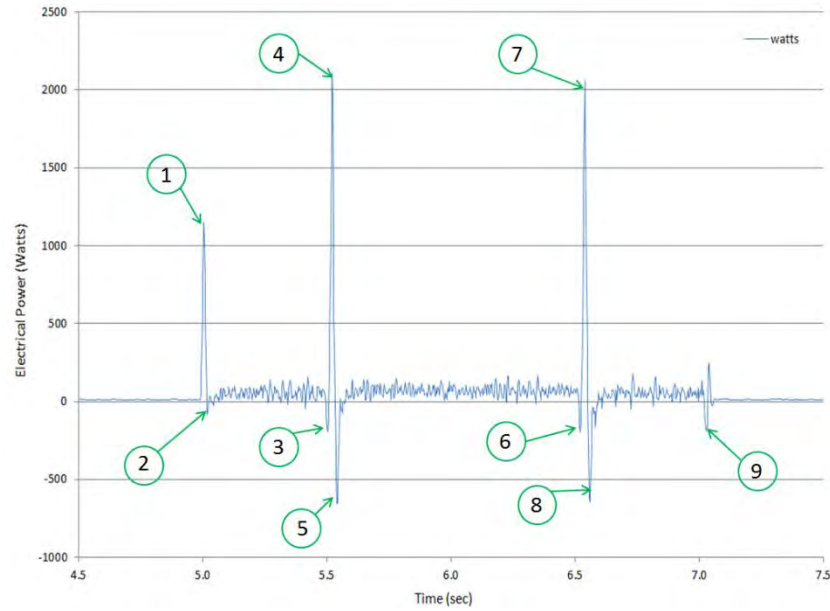


Figure 54 - Electrical Power from Reversal Test

Frequency Response

A sinusoidal frequency sweep test with no load is done to evaluate the frequency response of an EMA. A sinusoidal position command was used with a linearly increasing frequency from near to zero to 20 Hz:

$$x = A * \sin(2 * \pi * (f_{\max} / \Delta t) * A) \quad (1)$$

where A is the amplitude in millimeters, f_{\max} is the maximum frequency in hertz, and Δt is the change in time in seconds. The amplitude attenuation and phase lag from the frequency response test need to fall within the envelope defined by user specific parameters. Also the mechanical, electrical, and thermal results for the frequency response test are then analyzed to see if the EMA performance falls into the user specified parameters. Figure 55 below is the frequency response test commanded profile with a chosen 3.8 mm amplitude, 2.5% of the Danaher actuator's full stroke, and with sweeping frequency range from zero to 20 Hz. During the test, the actuator was mounted

vertically upsidedown. Positive displacement means the actuator is extending downward with gravity assisting.

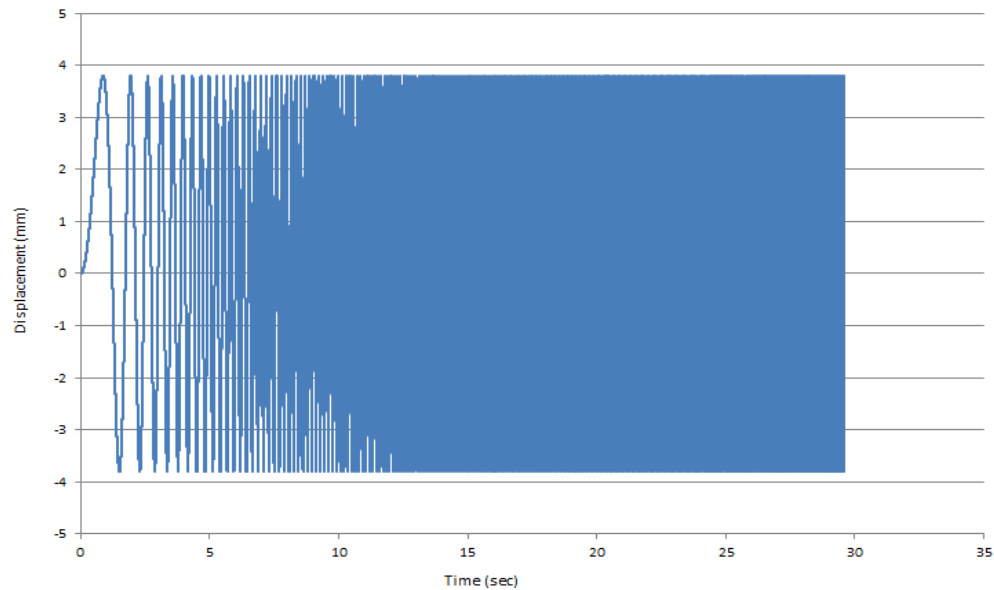


Figure 55 - Commanded Profile for the 3.8 mm Frequency Response Test

The displacement results of the sinusoidal frequency sweep test are shown in Figure 56. The vertical lines show the onset of velocity limit, current limit, and temperature limit which will be discussed later. Figure 57, Figure 58, and Figure 59 display the velocity, current, and thermal plots, respectively, along with pointing out where their individual limits were reached. Figure 60 displays the electrical power on the DC bus for the frequency sweep test.

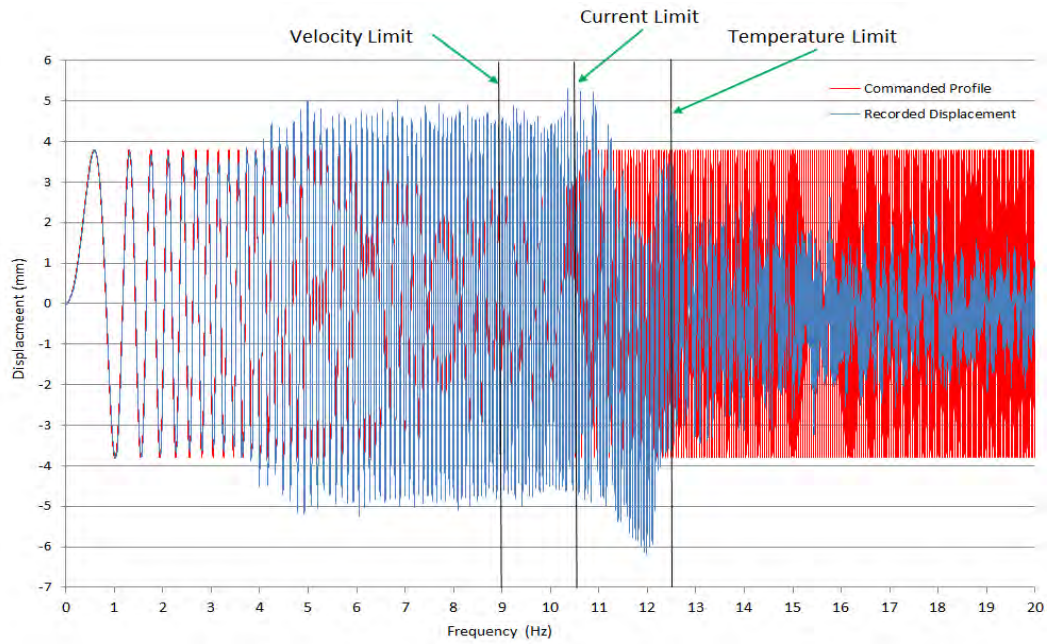


Figure 56 - Displacement Results from the 3.8 mm Frequency Sweep Test

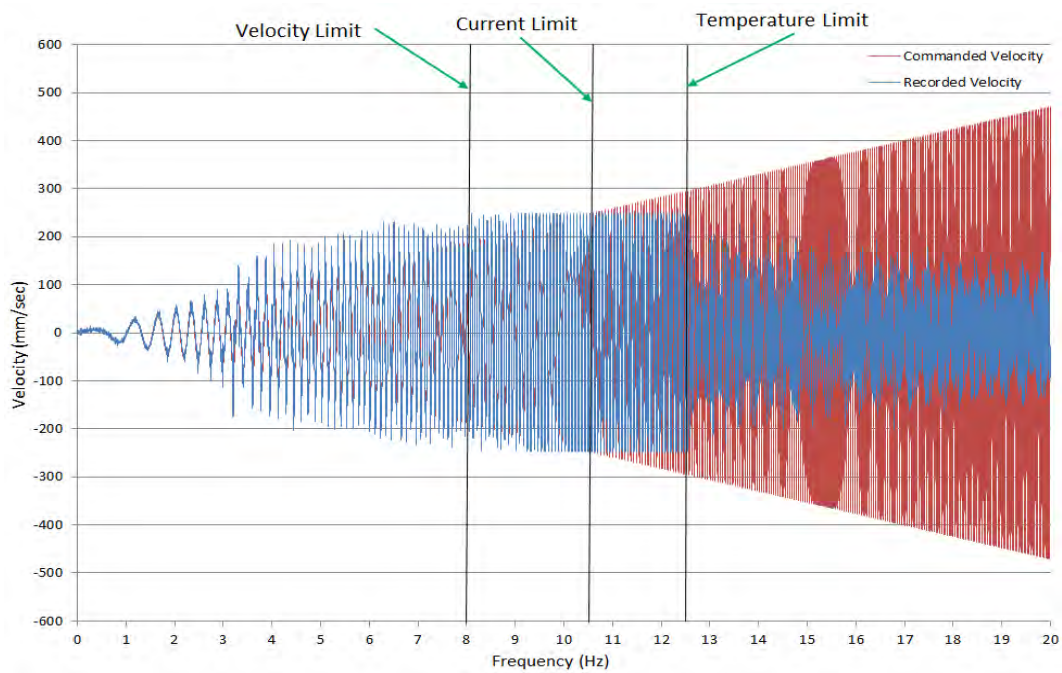


Figure 57 - Velocity Results from the 3.8 mm Frequency Sweep Test

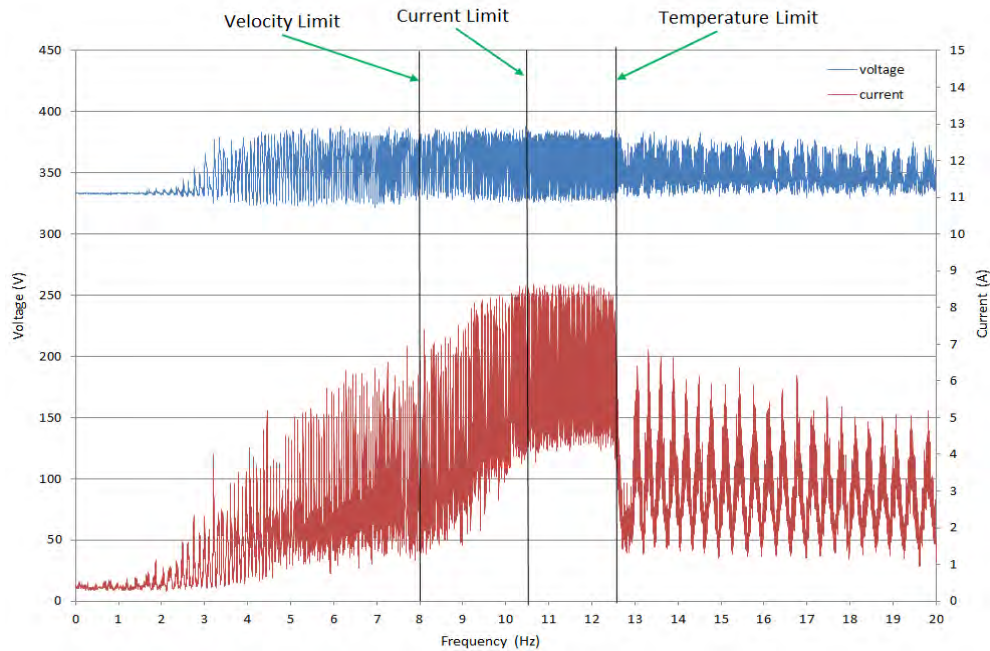


Figure 58 - Voltage and Current Results from the 3.8 mm Frequency Sweep Test

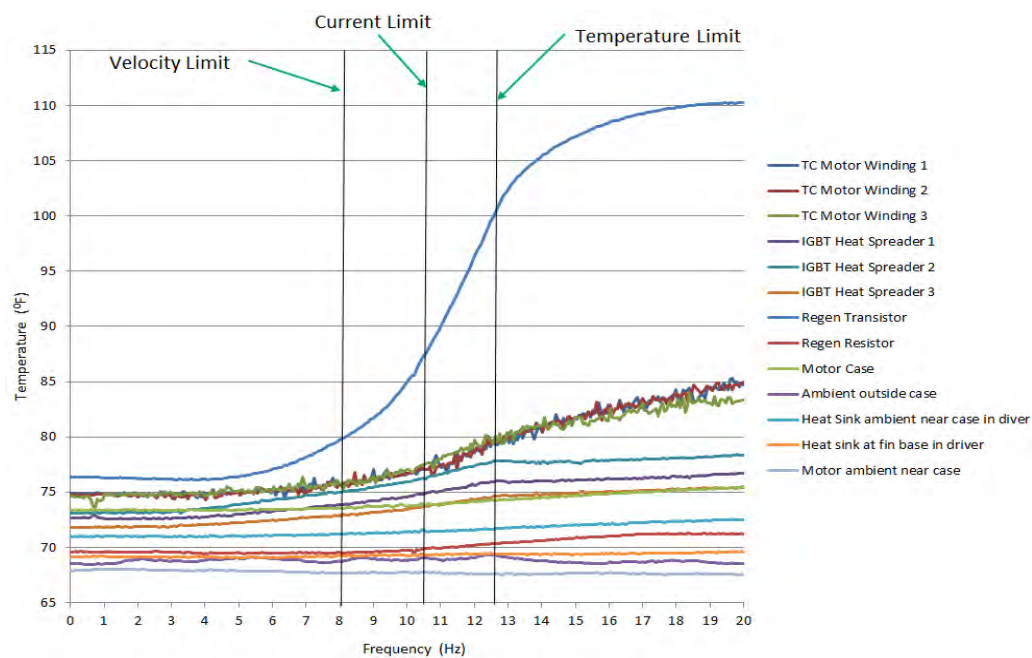


Figure 59 - Thermal Voltage and Current Results from the 3.8 mm Frequency Sweep Test

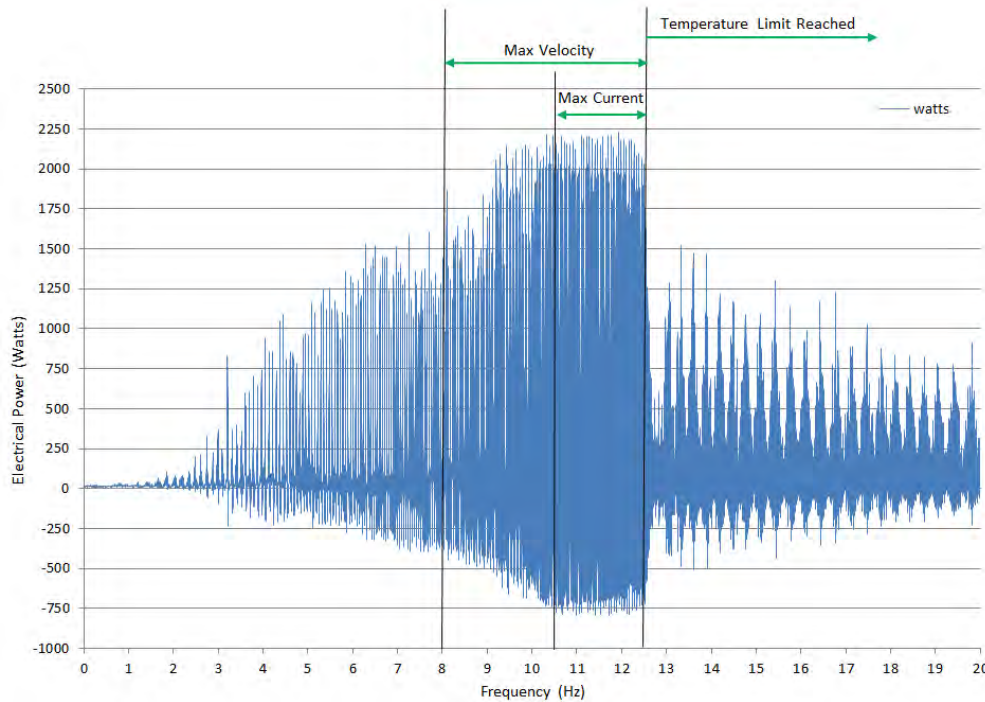


Figure 60 - Electrical Power Results from the 3.8 mm Frequency Sweep Test

A close up view of the EMA displacement control at each point in frequency the EMA reaches a limit in velocity, current, and temperature as shown in Figure 61, Figure 62, and Figure 63. Figure 57 shows that the actuator reached its velocity limit near 8 Hz. Starting from this frequency, the bus current began a much steeper climb as shown in Figure 58. At 10.5 Hz, the actuator reached its current limit. When the current limit is reached, the EMA control began to drift downward as it attempted to follow the commanded position while maintaining the magnitude of the commanded stroke. At the onset of reaching the velocity limit, accompanied by the sharp increase of current, the actuator's temperature starts rapidly increasing. This is shown by the regen transistor temperature in Figure 59. At 12.5 Hz, the bus current suddenly dropped about 50% and remained at the lower level for the rest of the test. The corresponding voltage and power also have dropped (Figure 62 and Figure 60). As a result, the actuator temperature

climbing rate decreased significantly as indicated by regen transistor and the three IGBT heat spreader temperatures in Figure 59. We believe that the sudden current drop was triggered by the overheating of the motor controller. Interestingly, when the actuator entered into a low current state, the actuator velocity dropped as well (Figure 57). The actuator is no longer able to maintain the stroke anymore (Figure 56).

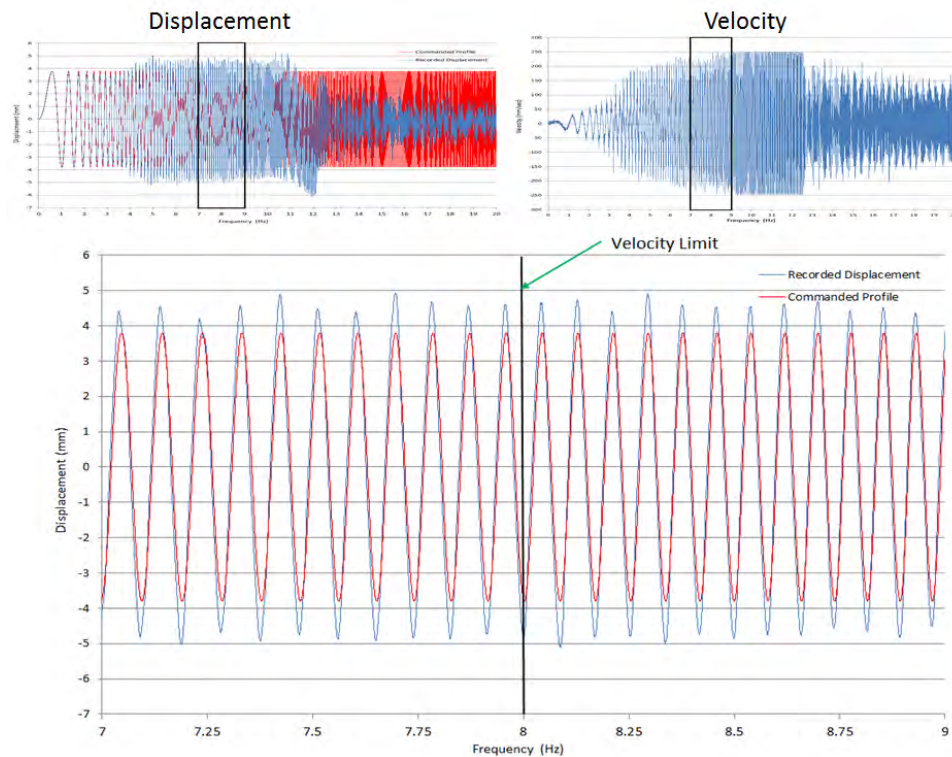


Figure 61 - Close up view of Displacement Results When Reaching the Velocity Limit

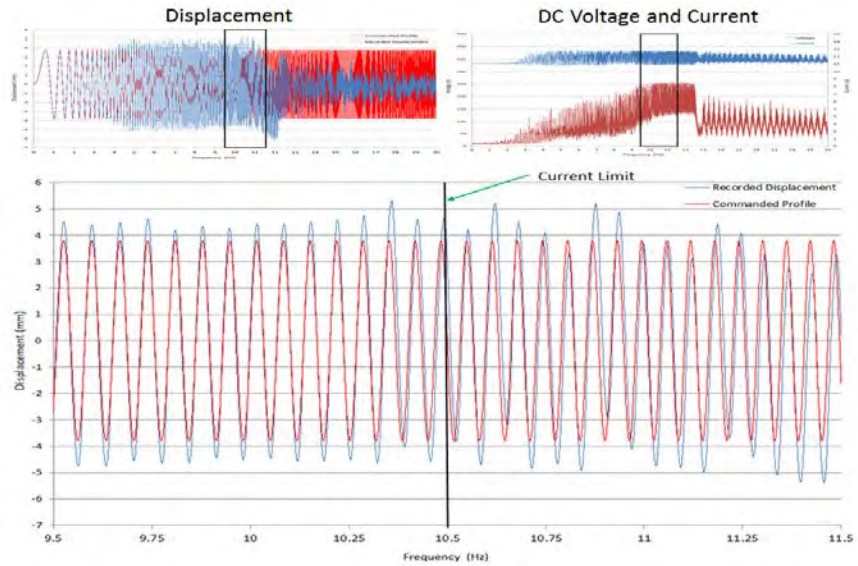


Figure 62 - Close up view of Displacement Results When Reaching the Current Limit

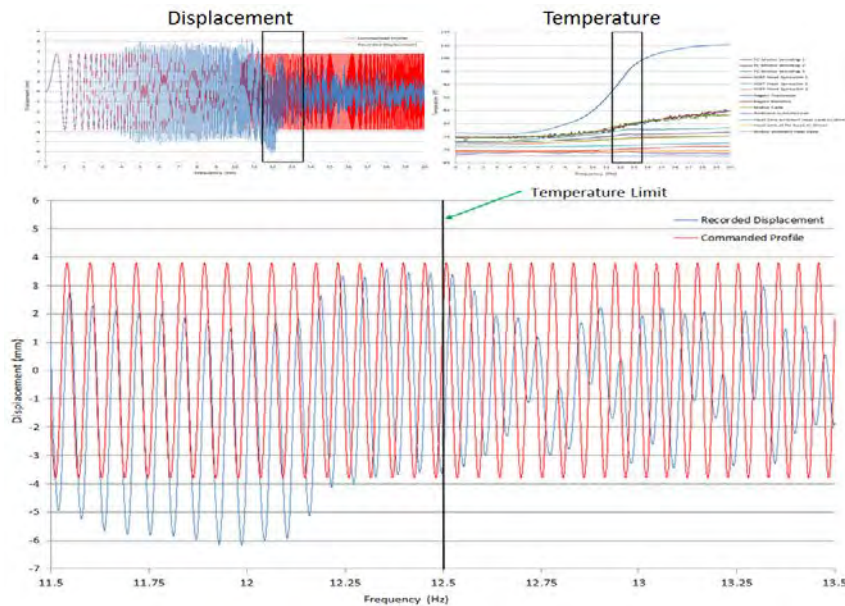


Figure 63 - Close up view of Displacement Results When Reaching the Temperature Limit

Figure 64 is the Bode plots of the actuator's frequency response. The EMA hit -3 dB at 10.5 Hz. This was where the current limit of the EMA was reached and the control

of the EMA displacement started to drift. The phase lag hit 60 degree at 12 Hz directly before the temperature limit was reached.

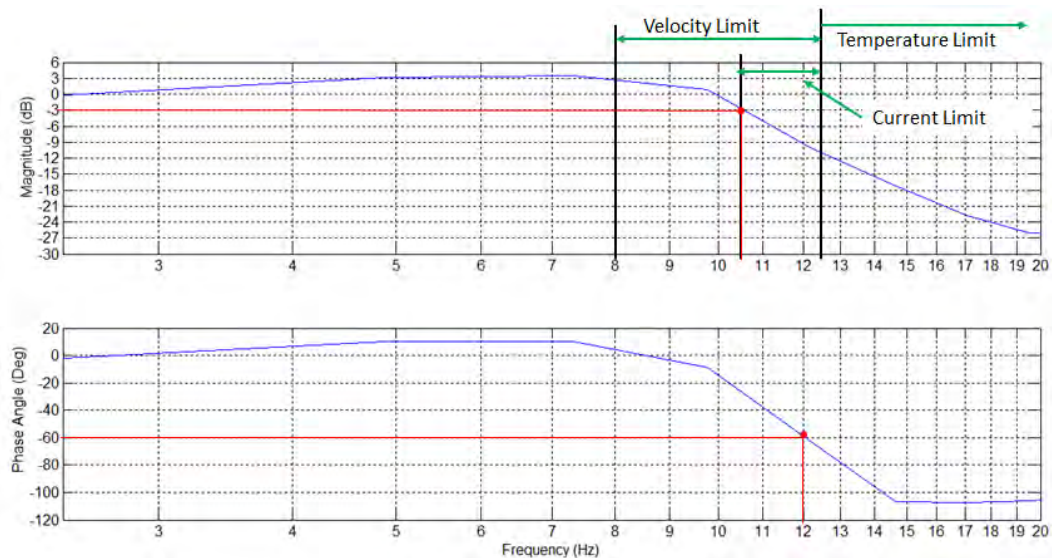


Figure 64 - Bode Plot of 3.8 mm Frequency Sweep Test

Holding Tests

Each flight control surface actuation system will be required to hold the surface under a user specified percentage of a stall load indefinitely. For those control surfaces where a mechanical brake mechanism is not allowed (e.g., an aileron), an EMA actuator relies on an electromagnetic field to hold the surface. During holding, all the electric current in EMA turns to heat, resulting in a thermally stressful scenario. The holding test evaluated the EMA's thermal performance.

For the Holding test, an EMA was commanded to hold zero displacement while a load of 5000 N (64% of the motor's stall load) was applied using the hydraulic load fixture. Figure 65 below shows the total thermal results recorded over the duration of the 1800 second test. The temperatures on the motor windings on the EMA rose considerably

and were still rising after 1800 seconds because of the high power draw to each winding to hold the 5000 N load while staying stationary. A closer look of the thermal stress induced on the motor windings as well as the IGBTs associated with these windings is shown in Figure 66 and Figure 67 respectively.

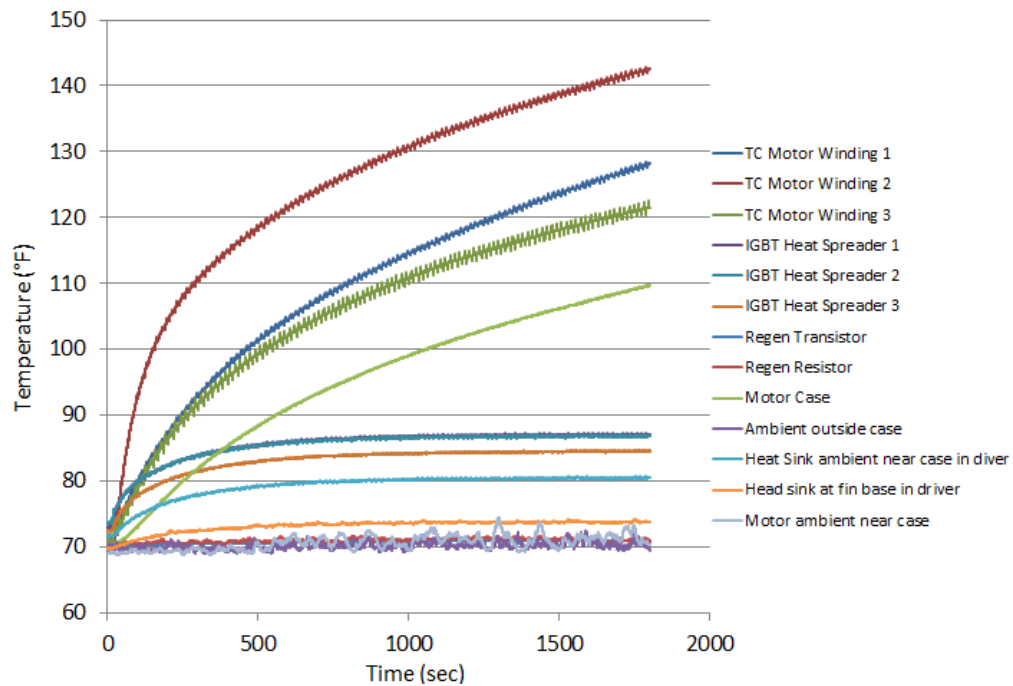


Figure 65 - Temperature plot for holding 5000 N with no Disturbance

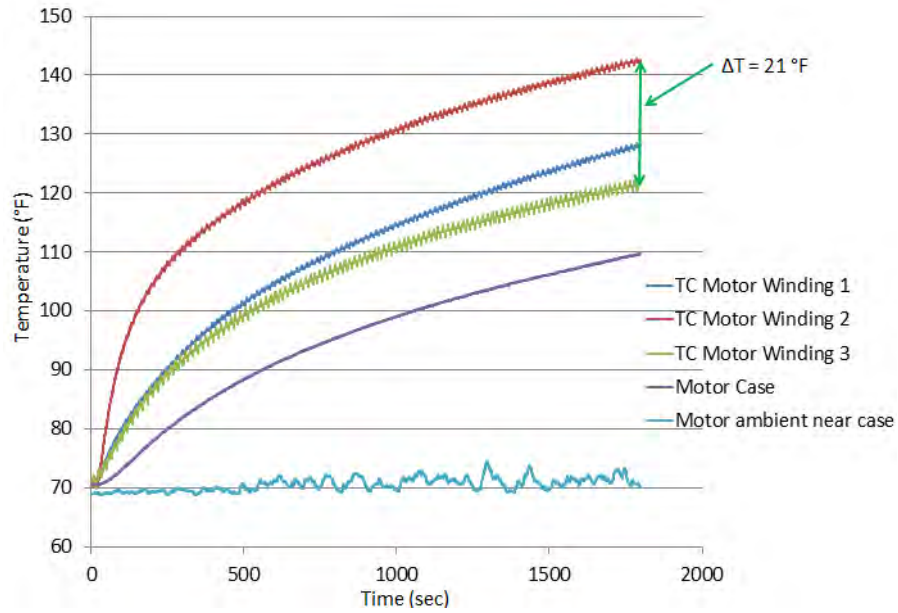


Figure 66 - Temperature plot of motor for holding 5000 N with no Disturbance

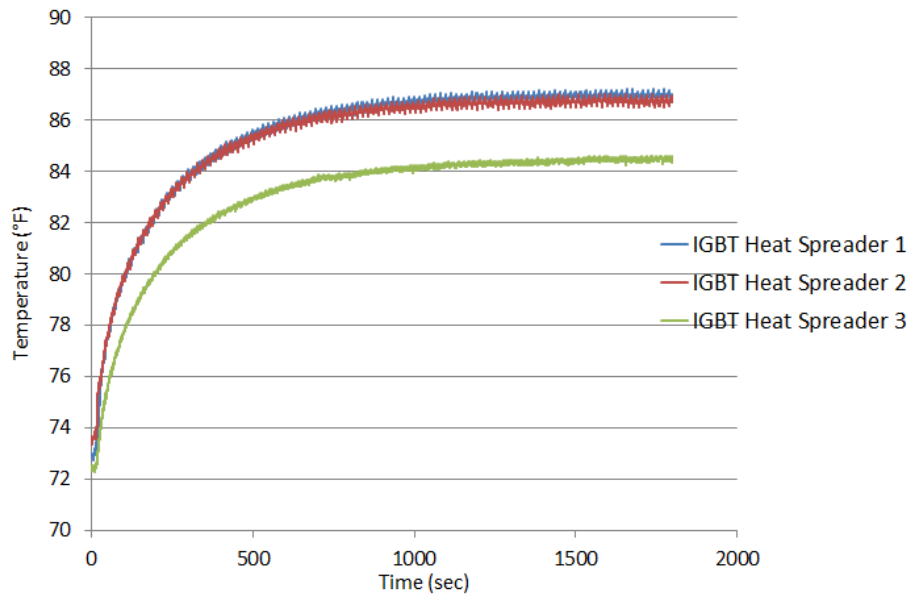


Figure 67 - Temperature plot of IGBTs for holding 5000 N with no Disturbance

In addition to high temperature rise, the motor's three windings also experienced significant temperature difference, 21 degree Fahrenheit at 1800 second (Figure 66),

which could cause thermally induced structure stress. One way to reduce the thermal gradient and, thus, the overall thermal stress on the windings for a wye-connected 3-phase motor is to engage all three phases equally throughout the holding profile. To do this, half a rotation of the motor, 1.6 mm displacement, (which correlated to a displacement of -0.8 mm to 0.8 mm) was needed to equally distribute electrical power across the three windings throughout the holding test. Understanding that such a rotation, imposed as a disturbance on holding, deems that the test is not strictly holding anymore. The author does not know the impact of such a motion disturbance on the control of the aircraft and its feasibility. The goal here is to evaluate the effectiveness of such a motion disturbance in reducing temperature gradient among the windings of the motor, and therefore reducing the thermally induced structure stress. A sinusoidal displacement profile with amplitude of 0.8 mm and frequency of 0.01Hz was chosen for this task and the test was run again with a 5000 N load applied to the EMA. The amplitude of 0.8 mm is equivalent to one quarter rotation of the motor. The low frequency of 0.01 Hz was chosen to minimize the impact of the sinusoidal movement of the motor on the control surface. The commanded and recorded displacement and force for the sinusoidal holding test is shown in Figure 68 and Figure 69 below. The force variation in Figure 69 is a result of the hydraulic press active load control. The hydraulic load fixture is actively controlling force when connected to the EMA while the EMA is extending and retracting.

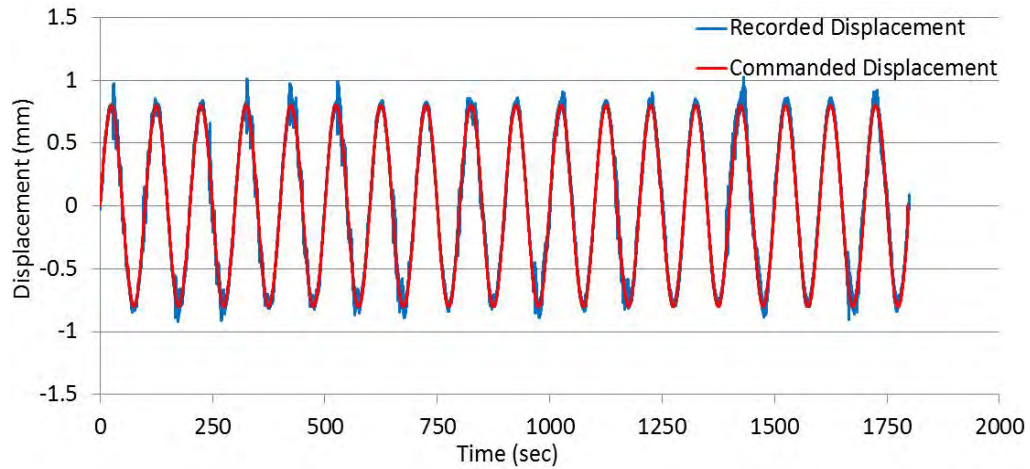


Figure 68 - Commanded and Recorded Displacement for the 5000 N Holding Test with a Sinusoidal Disturbance

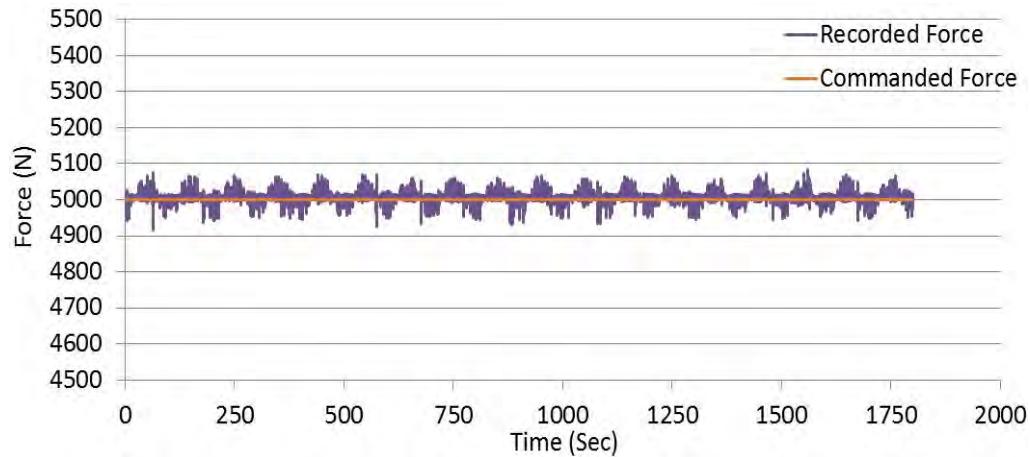


Figure 69 - Commanded and Recorded Force for the 5000 N Holding Test with a Sinusoidal Disturbance

The temperature plot of all the thermocouples is shown below in Figure 70, while Figure 71 and Figure 72 are temperature readings from the motor and the driver, respectively. Temperature oscillation in the motor windings corresponding to the back forth rotation of the motor can clearly be seen in Figure 71 when the motor rotated half a rotation in a sinusoidal fashion. The three phase motor windings' temperature gradient is

4 degrees Fahrenheit at 1800 second (Figure 71), compared to 21 degree Fahrenheit at still holding (Figure 66), a significant reduction.

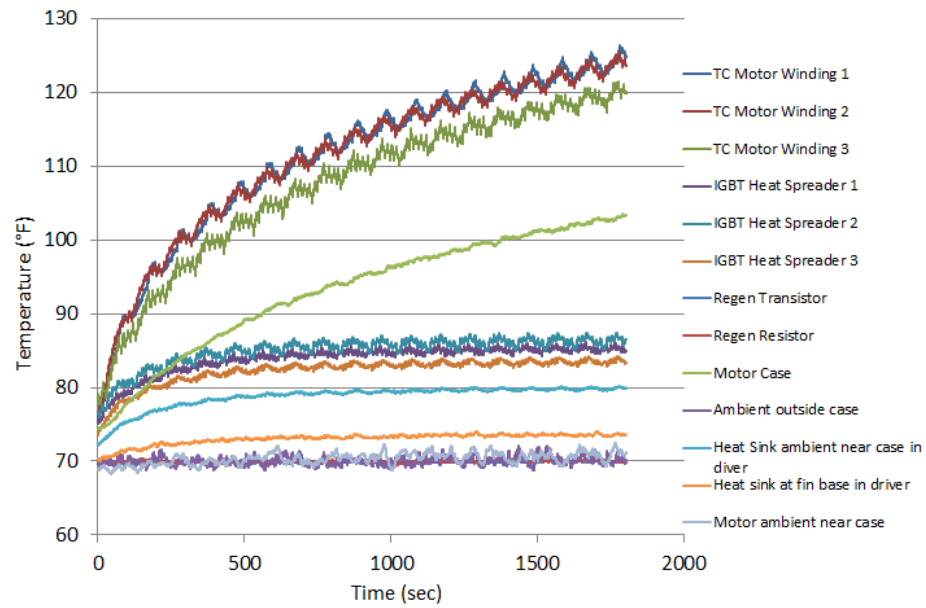


Figure 70 - Temperature plot for holding 5000 N with Sinusoidal Disturbance

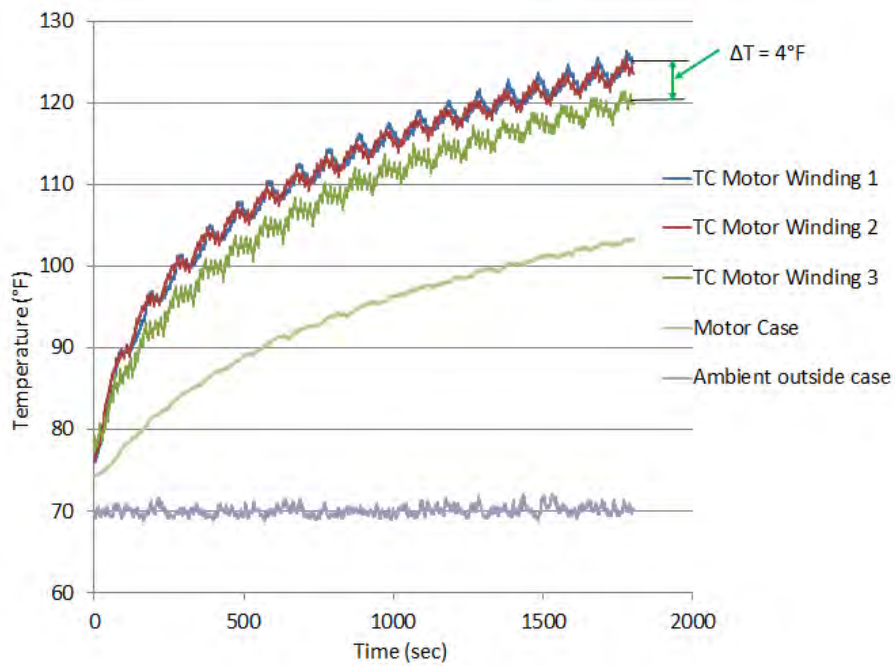


Figure 71 - Temperature plot of Motor for holding 5000 N with Sinusoidal Disturbance

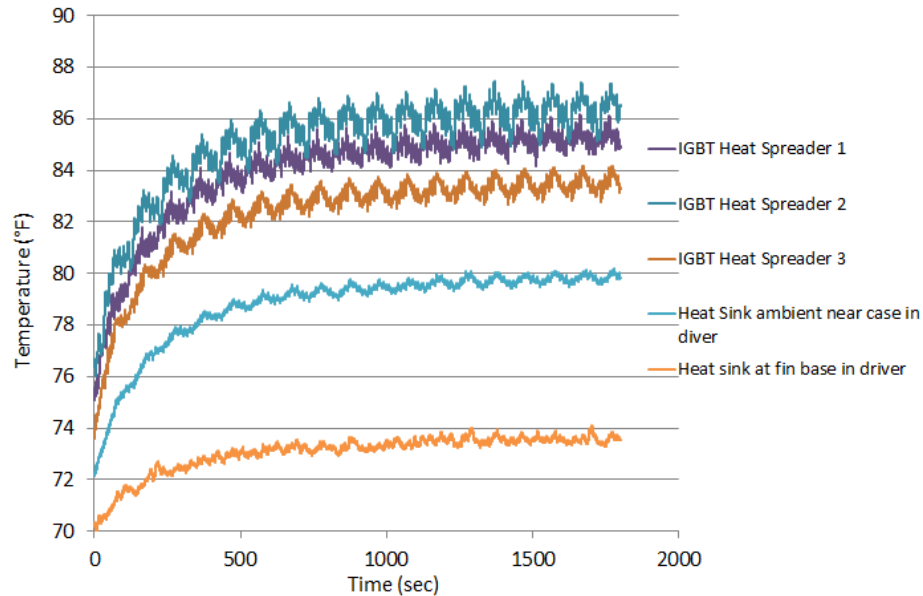


Figure 72 - Temperature plot of IGBTs for holding 5000 N with Sinusoidal Disturbance

There is a clear difference in temperature gradient within the motor windings between the 5000 N holding test with no oscillation to the 5000 N holding test with sinusoidal oscillation that engages all 3 motor windings by rotating the motor half a rotation. The holding test in which the 3 windings are engaged, compared to the holding test with no sinusoidal oscillation, had a temperature gradient of ΔT reduction from 21 degree Fahrenheit to 4 degree Fahrenheit (81% reduction).

CHAPTER 7

DYNAMIC LOAD CONTROL

In order to test real time dynamic flight loads an actuator would encounter while in flight and how the actuator being tested can handle such loads, a mission test was run. The stroke and force profile of the mission test was generated using information based the NASA Dryden flight study [7]. The profile was scaled to fit the capabilities of the current industrial EMA on hand that will be used in the test set-up. Where the commanded for to the EMA was 7% of the force from the recorded mission profile and the maximum displacement rate for the EMA was reduced to 57% from the recorded mission profile velocity. For future testing the combat mission profile will not be scaled down because the purpose of the testing is to make sure the EMA can handle similar inflight dynamic loads and displacements. Figure 73 below displays the results of a dynamic segment of the mission test run. It can be seen that improvement needs to be done on control of the hydraulic load fixture when running a dynamic stroke and load profile while coupled to the EMA. The hydraulic load fixture control when coupled with the EMA is less than desirable when running a mission test with 50% overshoots of commanded loads when the frequency of the commanded load is higher.

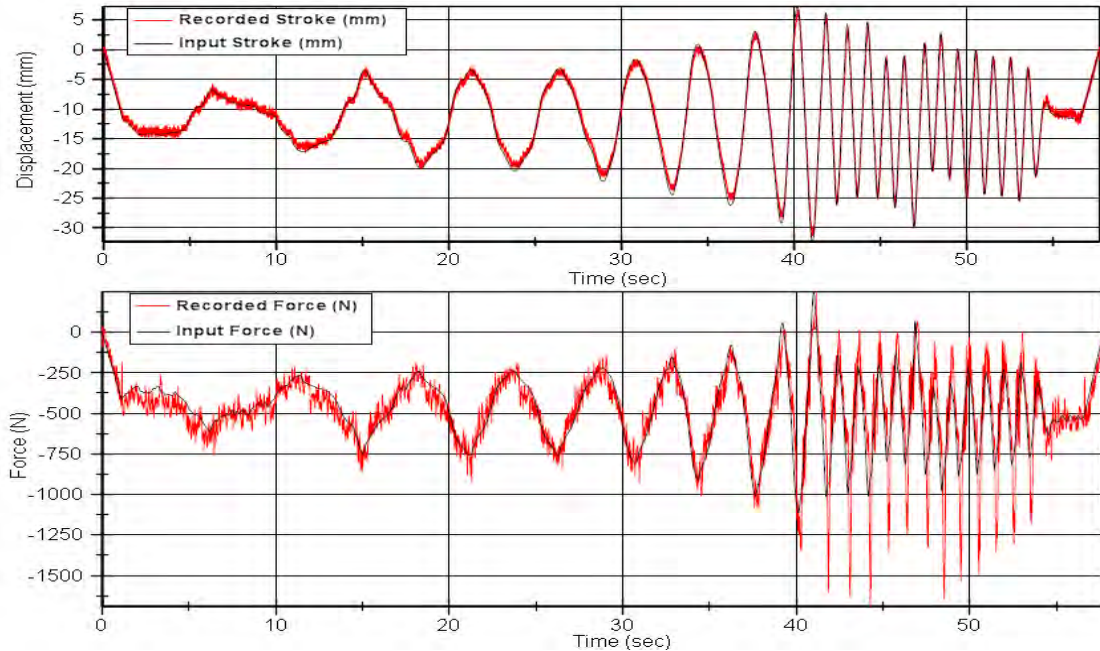


Figure 73 - Control of Force and Displacement over a Dynamic Profile

Cascade Control

Extensive work has been done to tighten up the control of the hydraulic press with the use of a PID cascade control loop for the press that is inside the LabVIEW control block of the experiment to allow “on the fly” load compensation. In order to have the best possible control between the EMA and hydraulic load fixture when running dynamic mission profile while coupled together, an EMA Test System Control Scheme and a Cascade Control Command Generation diagram was developed, as seen below in Figure 74 and Figure 75 respectively. Figure 74 depicts the overall test control, where the National Instruments Data Acquisition (DAQ) records the force on the EMA and places it into the PID loop shown in Figure 75. The PID loop utilizes integrals and derivations to adjust the force command signal to the hydraulic load fixture controller in order to tighten the control of the load on the EMA during a test.

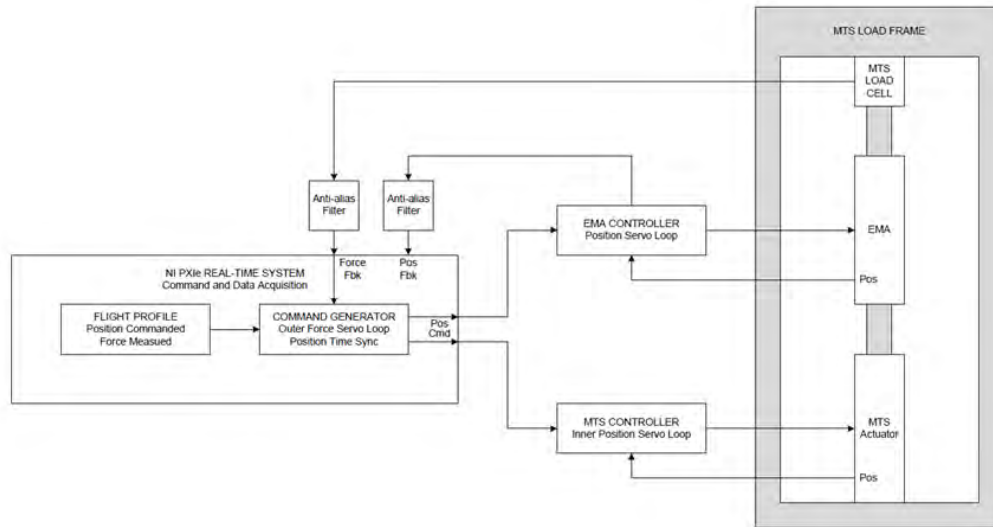


Figure 74 - EMA Test System Control Scheme

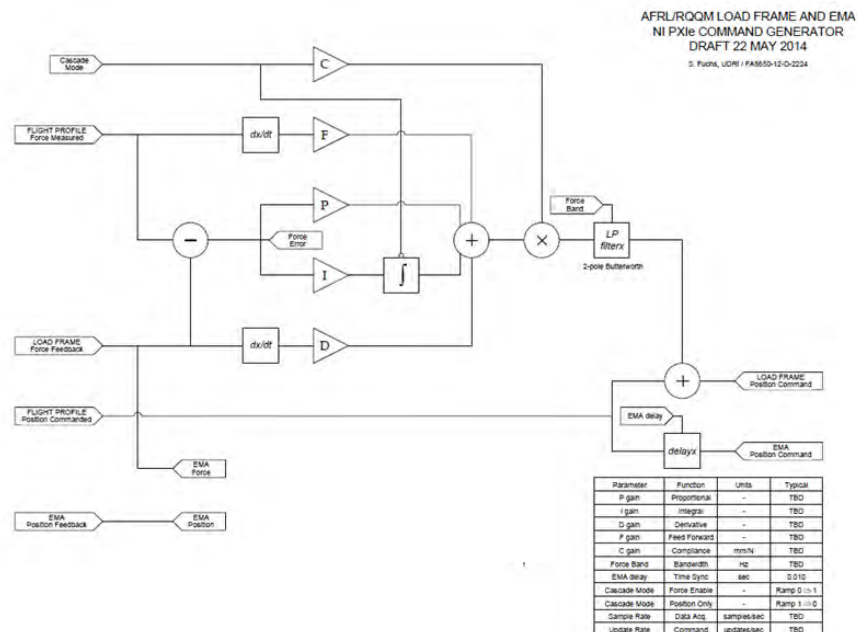


Figure 75 - Cascade Control Command Generation

Signal Response of the EMA and Hydraulic Press Fixture

A signal response test needed to be performed on both the MTS hydraulic fixture and the EMA. This is so when running a test where the EMA and hydraulic fixture are

both imposing a dynamic movement or force that they do so simultaneously with minimal lag time. A difference in time can cause control issues with the EMA and hydraulic fixture when they are attached together running a test profile. An NI LabVIEW program was developed to test these signal responses by recording the signal being fed to the controller along with position/force feedback signal from the system. These were recorded on the same clock in the DAQ Real Time system so that a time delay was part of the recorded data. A diagram involving the DAQ and controller for the signal response test is displayed below in Figure 76.

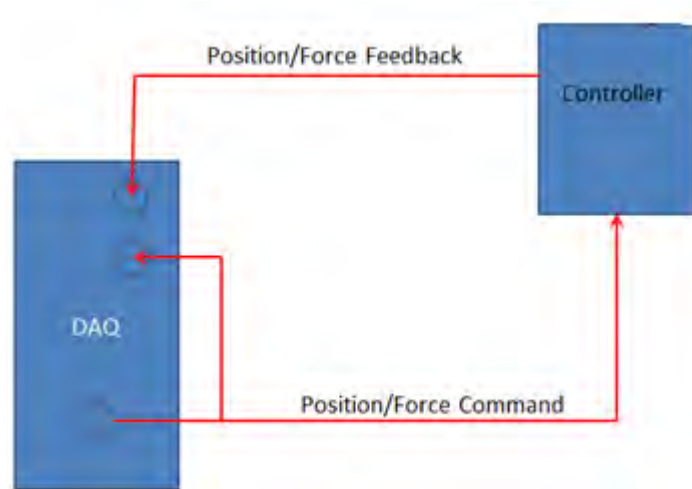


Figure 76 - Diagram of Signal Response Test

Sine sweep signal response tests were performed with the MTS hydraulic fixture stroke frequency ranging from 0.5 Hz to 6 Hz. Multiple cycles were recorded so as to find the average time delay of each frequency. This was done by taking the time difference when the commanded signal and the recorded signal go through a 'zero' point on the profile. The stroke displacement for the hydraulic fixture was 10 mm.

Similar sine sweep signal response tests were performed with the Danaher EMA from 0.5 Hz to 6 Hz decoupled from the hydraulic press arm. Because of a high level of noise was on the recorded displacement signal, a three point smoothing was used. An enlarged plot of the 4Hz test run on the EMA is shown in Figure 77 below.

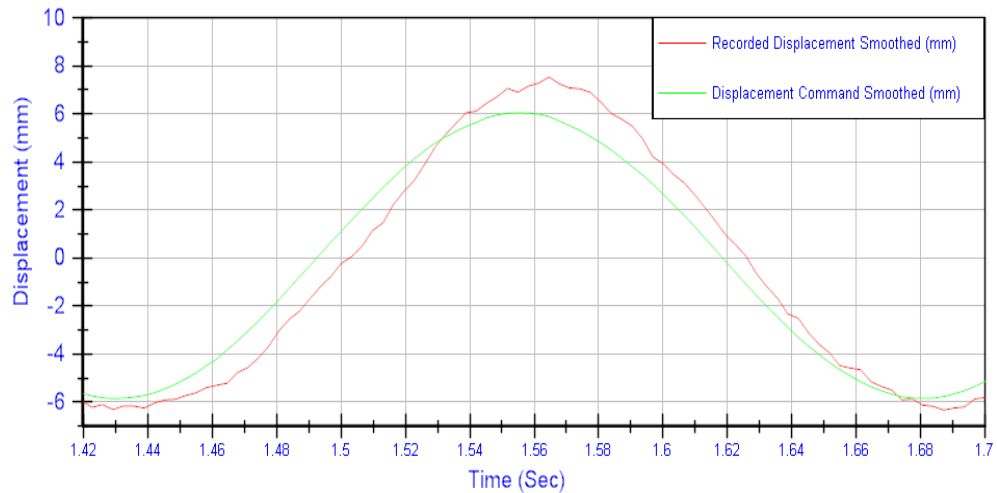


Figure 77 – Segment of a 4 Hz Signal response of EMA

For the best results of the signal response test data above, a 1000 Hz analog pre-filter created for the MTS recorded displacement signal to eliminate any unwanted. The results from the tests run are shown below in Figure 78 [29].

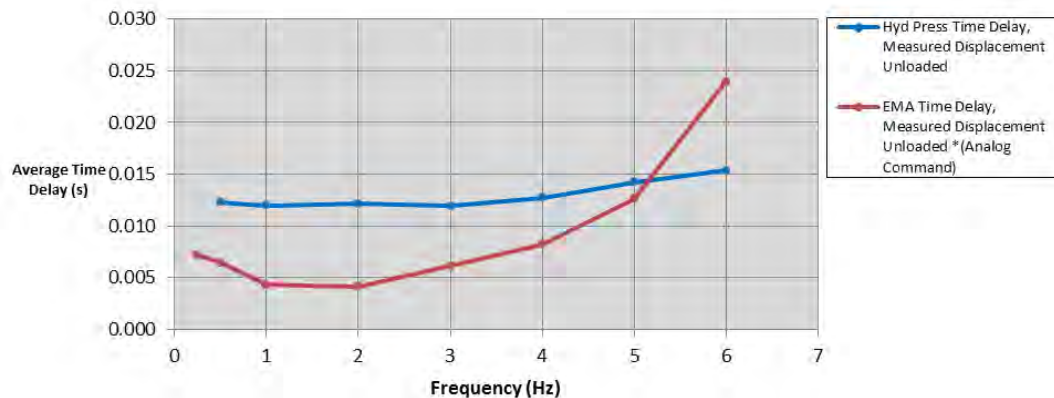


Figure 78 - Time Delay vs Frequency for Press and EMA [29]

The results were as expected with the EMA's time response, although nonlinear, being faster than the hydraulic fixture. It is speculated that the reason for the EMA's time delay increase with increasing frequency is because the rate at which the controller can command displacement is being reached. This occurs somewhere between the 2 Hz and 3 Hz range of the signal, where there is a rise in time delay for the EMA. This is acceptable for the testing and control of the EMA because the frequency rate at which the EMA is being tested in a flight scenario will not be above 3 Hz.

In order to exhibit dual control of displacement and force for the hydraulic load fixture (Figure 75) the LabVIEW command must be able to equate an offset in displacement to force seen by the load. The EMA system spring constant, $F=kX$ (Hooke's Law), needed to be determined so that it can be incorporated into the cascade control command generation for the test rig.

The EMA was commanded to hold position (given a zero speed command) while coupled to the hydraulic load fixture. The hydraulic load fixture was commanded to exert a sinusoidal force ($\pm 2,500$ N centered at 2,600 N). Force and displacement were recorded from the hydraulic load fixture Analog I/O and plotted against each other. The inverse of the slope of the linear best fit to the data is the system C-value, where $C = 1/k$. Below, in Figure 79 and Table 3, is a plot and table of the EMA system spring constant 'C' at frequencies 0.5 Hz, 1 Hz, and 4 Hz [29]. The C-value measured from this data was reasonable to use in the PID control because the majority of a mission test will be in the 0.1 Hz to 1 Hz frequency range and the slopes in that range shown in Table 3 are very close in value. [29].

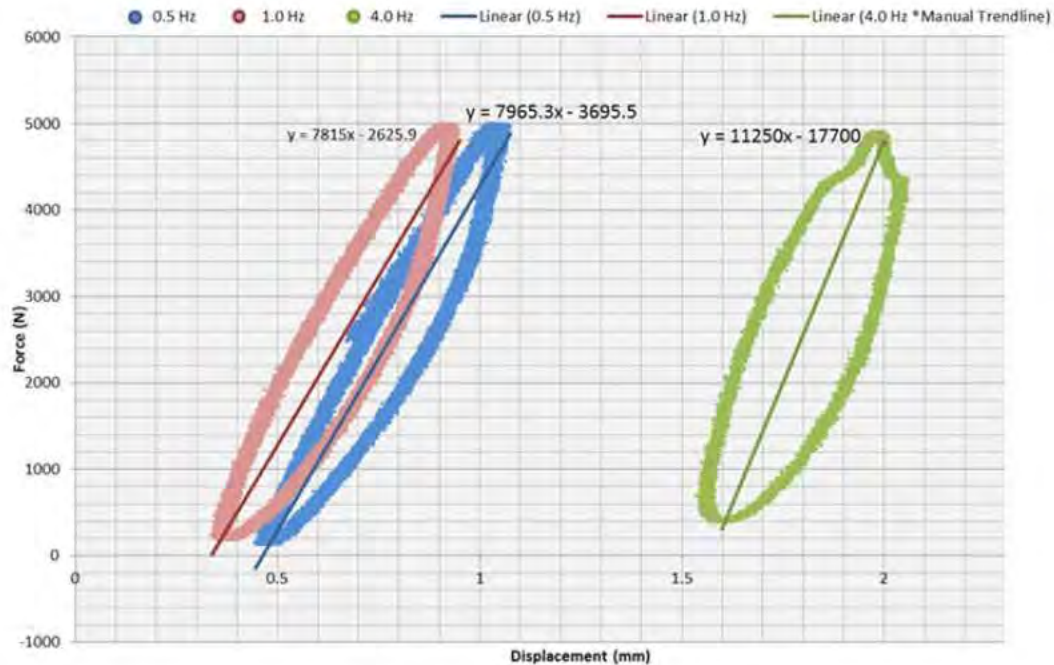


Figure 79 - System Spring Constant (K) [29]

Table 3 - System Spring Constant Results

Frequency (Hz)	Slope K (N/mm)	C-Value (N/mm)
0.5	7965	1.26E-04
1.0	7815	1.28E-04
4.0	11250	8.89E-05

Recording Electrical Data

Three phase motor electrical data was collected in order to record accurate electrical readings of the power going to the EMA motor from the controller. Correct sensors and appropriate filtering must be chosen to obtain the reliable electrical data at high rates on the three phase lines. This is required so that high speed transient data can be recorded when testing the EMAS. This experiment currently uses a Newton's 4th Power Analyzer for recording of electrical data of the EMAS because the correct voltage

and current sensors still need to be appropriate filtering to obtain the most reliable data. DC bus voltage and current RMS value were recorded via a Newton's 4th power analyzer which analyzes the signals at 2.2 MHz and records the values calculated for power, voltage and current at a 500 Hz rate.

In order to record electrical data on the DC bus with voltage probes and hall effect current sensors, a sampling rate of 100,000 samples per second was chosen for the motor's DC bus voltage and current. (The high speed DAQ can sample 16 channels simultaneously at 1 MHz so it can record at the specified 100,000 samples per second rate.) There was noise in the electrical signals being recorded. To eliminate the high frequency content on the line from EMI and the 16 kHz switching frequency of the motor controller on the lines and prevent the recording of aliased data, a 3777 Hz 2-pole Passive low pass analog pre filter was built for the DC bus voltage and DC bus current signal. The filtered voltage and current signals are shown in Figure 80 and Figure 81 respectively.

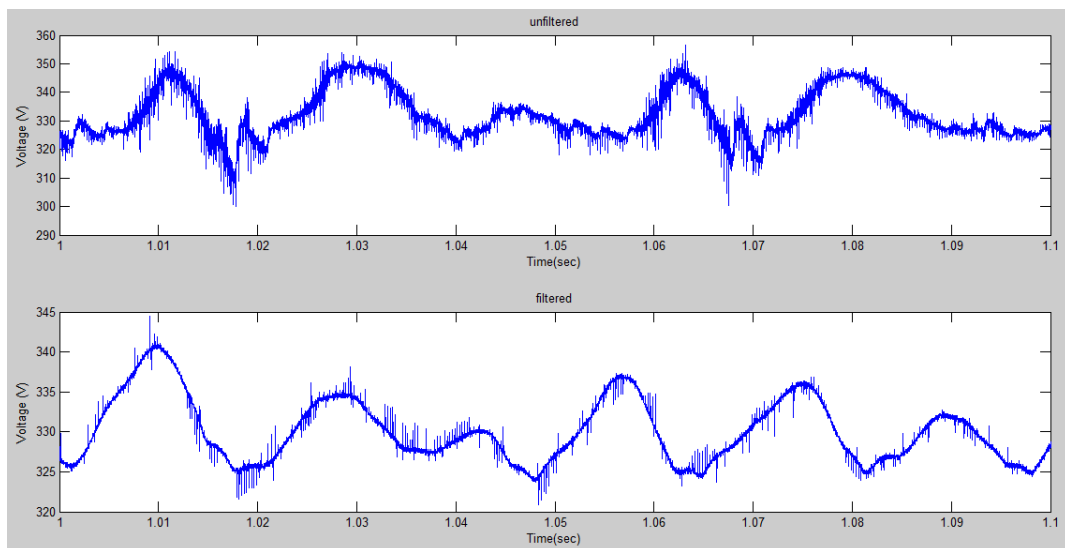


Figure 80 - Unfiltered and Filtered DC Bus Voltage

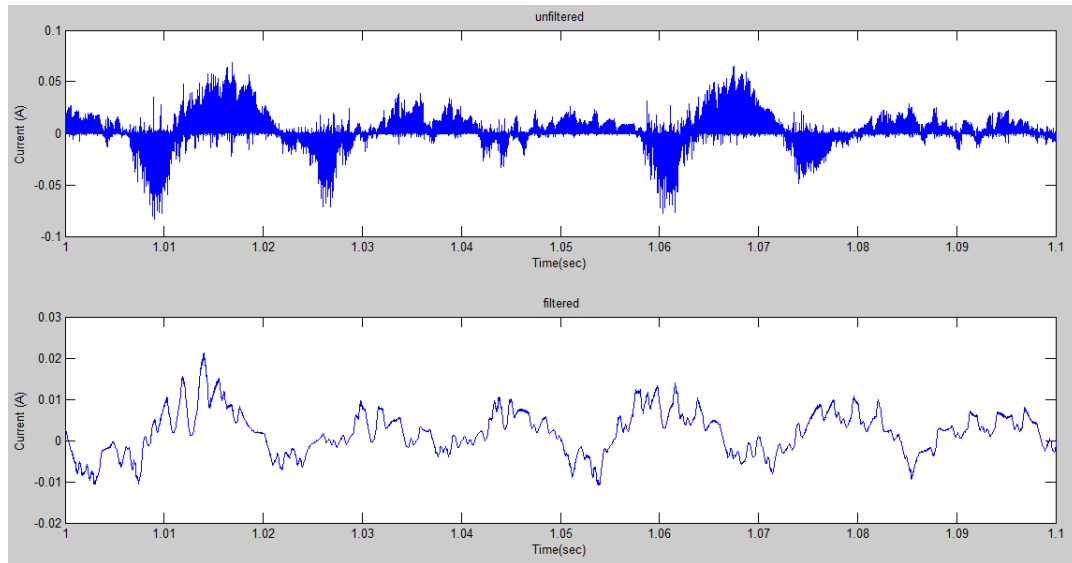


Figure 81 - Unfiltered and Filtered DC Bus Current

CHAPTER 8

CONCLUSION

A laboratory apparatus and data acquisition system were successfully constructed for evaluating scaled aircraft flight control actuators under simulated mission profiles. A MTS hydraulic load frame is used to simulate a control surface's aerospace load. A NI based DAQ was used to record the motor controller's DC bus voltage at high rates and the actuator's position, load, and temperatures. The DC bus rms voltage, current, power, and regenerative power were recorded by a Newton's 4th power analyzer. Key performance characteristics tests such as frequency response, step response, reversal, backlash, and holding were carried out with a Danahar EC5 actuator to validate that this lab setup can successfully evaluate and characterize EMAS.

The lab tests show that holding presents the most significant challenge to the thermal management of an EMA system. During a holding, all the electric power is converted to heat. The motor windings and motor controllers are heated unevenly causing temperature gradient induced structure stress. To reduce the thermal gradients within the motor, a half rotation back and forth in the form of a 0.01 Hz sinusoidal disturbance was imposed on holding to evenly engage the motor's three phases. This resulted in an 81% temperature variation reduction among the three windings. Although a small motion

disturbance is effective in reducing the motor and motor drive's thermal gradients, it is not known if such a disturbance is feasible in practice.

The continuous frequency sweeping revealed that the EMA under test reaches the speed limit first, then the current limit, and finally the temperature limit. When the actuator's electronics reached the thermal limit, the actuator controller drastically reduced its power. This caused drastic amplitude and phase lagging. Continuous frequency sweeping proved to be a useful test to evaluate EMA's performance.

The step response and reversal test showed that when an EMA reverses direction or suddenly decelerates, a significant spike of regenerative power may occur. This regen power could present as a thermal challenge to an aircraft flight control EMA system.

To use this lab apparatus to simulate dynamic mission profile of an aircraft flight control surface, the accuracy of the load provided by the MTS hydraulic load frame has to be improved. A double loop control scheme has been derived. The hope is that once this control strategy is implemented, this lab setup will be fully capable of subjecting an EMA to a simulated flight control mission and evaluate its performance.

BIBLIOGRAPHY

- [1] Lammers, Z., "Thermal Management of Electromechanical Actuation System For Aircraft Primary Flight Surface Controls", MS thesis, Dept. Mech. Eng., University of Dayton, Dayton, OH, 2013.
- [2] Robinson, D., "Design and Analysis of Series Elasticity in Closed-loop Actuator Force Control", PhD dissertation, Dept. Mech. Eng., Massachusetts Institute of Technology, Cambridge, MA, 2000.
- [3] Moir, I. and Seabridge, A., "Flight Control Systems", *Aircraft Systems; Mechanical, Electrical and Avionics Subsystems Integration*, 3rd ed. West Sussex, England: Wiley, 2008, pp.4-5.
- [4] Garg, A., Linda, R., and Chowdhury, T., "Evolution of Aircraft Flight Control System and Fly-By-Light Flight Control System", *International Journal of Emerging Technology and Advanced Engineering*, Vol. 3, Issue 12, pp.60-64, December, 2013.
- [5] Pratt, R. W., "Industrial considerations for flight control", *Flight Control Systems: practical issues in design and implementation*, Stevenage Hertz, United Kingdom: The Institution of Engineering and Technology, London, England and The American Institute of Aeronautics and Astronautics, 2008, pp.7-9.
- [6] Janker, P., Claeysen, F., Grohmass, B., et al., "New Actuators for Aircraft and Space Applications", *11th international Conference on New Actuators*, Technical Paper, pp. 346-354, Bremen, Germany, June, 2008.
- [7] Jensen, S. C., Jenney, G. D., Raymond, B. and Dawson, D., "Flight Test Experience with an Electromechanical Actuator on the F-18 Systems Research Aircraft", *19th AIAA Digital Avionics Systems Conference*, 7-13 Oct. 2000, Philadelphia, PA, USA.
- [8] Barnett, S., Lammers, Z., Razidlo, B., Leland, Q. et al., "Test Set-up for Electromechanical Actuation Systems for Aircraft Flight Control," *SAE 2012 Power Systems Conference*, SAE Technical Paper 2012-01-2203, October, 2012.

- [9] Wells, J., Amrhein, M., Walters, E., Iden, S., et al, "Electrical Accumulator Unit for the Energy Optimized Aircraft", *SAE International Aerospace Conference*, Technical Paper 2008-01-2927, November, 2008.
- [10] Jacob, J. D. "On The Fluid Dynamics and Adaptive Airfoils," *Symposium on Adaptive Structures and Material Systems -1998 ASME International Mechanical Engineering Congress and Exposition*, Anaheim, CA, November, 1998.
- [11] Cesnik, C., Brown, E., "Active Warping Control of A Joined-Wing Airplane Configuration," in *44th AIAA/ASME/ASCE/AHS Structures, Structural Dynamics, and Materials Conference*, Norfolk, Va, April 2003.
- [12] McRuer, D., "A Flight Control Century: Triumphs of the System Approach", *Journal of Guidance*, No. 2, pp. 161-173, August, 2003.
- [13] Chakraborty, I., Mavris, D., "A System and Mission Level Analysis of Electrically Actuated Flight Control Surfaces using Pacelab SysArc", AIAA Science and Technology Forum and Exposition (SciTech) 2014, National Harbor, Maryland, Jan 13-17, 2014, AIAA-2014-0381.
- [14] Rosero, J., Ortega, J., Albada, E., and Romeral, L., "Moving Towards a More Electric Aircraft," *IEEE A&E Systems Magazine*, March 2007, pp. 3-9.
- [15] Kleemann, E., Dey, D., and Recksiek, M., "The Development of A Civilian Fly By Wire Flight Control System", ICAS Congress, 2000.
- [16] Bennett, J., Mecrow, B., Atkinson, D., Atkinson, G., "Safety-critical design of electromechanical actuation systems in commercial aircraft", *IET Electric Power Applications Journal*, Vol. 5, Iss. 1, pp. 37-47, 2011.
- [17] Vaculik, S., "A Framework for Electromechanical Actuator Design", PhD dissertation, Dept. Mech. Eng., The University of Texas at Austin, Austin, TX, May, 2008.
- [18] Croke, S. and Herrenschmidt, J. "More Electric Initiative-Power-by-Wire Actuation Alternatives," in *Aerospace and Electronics Conference*, Dayton, OH, 1994, pp.1338 – 1346
- [19] Hall, D. and Layton, S., "Hybrid Electrical Power Source Testing For Electromechanical Actuation Applications" *IEEE Energy Conservation Engineering Conference*, IEEE Technical Paper 5472636, Washington, DC, August, 1996.
- [20] Van den Bossche, D., "The A380 Flight Control Electrohydrostatic Actuators, Achievements and Lessons Learnt," *25th International Congress of the Aeronautical Sciences, ICAS 2006*, September, 2006.

- [21] Bennett, J., Mecrow, C., Atkinson, D., "A Prototype Electrical Actuator for Aircraft Flaps", *IEEE Transactions on Industry applications*, Vol. 46, No. 3, pp. 915-921, May/June, 2010.
- [22] Balaban, E., Saxena, A., Bansal, P., Goebel, K.F., Stoelting, P., Curran, S., "A Diagnostic Approach for Electro-Mechanical Actuators in Aerospace Systems" *IEEE Aerospace Conference*, Big Sky, MT, March, 2009.
- [23] Balaban, E., Saxena, A., Goebel, K., Byington, C., Watson, M., Bharadwaj, S., Smith, M., Amin, S., "Experimental Data Collection and Modeling for Nominal and Fault Conditions on Electro-Mechanical Actuators", *Prognostic Health Management Conference*, San Diego, September, 2009.
- [24] Antonelli, M., Bucci, G., Ciancetta, F., Fiorucci, E., "Automatic test equipment for avionics Electro-Mechanical," *Measurement*, no. 57, pp. 71-84, November 2014.
- [25] Balaban, E., Saxena, A., Narasimhan, S., Roychoudhury, I., Goebel, K., Koopmans, M., "Airborne Electro-Mechanical Actuator Test Stand for Development of Prognostic Health Management Systems", *Prognostic Health Management Conference*, Portland, OR, January, 2010
- [26] Koopmans, M., Mattheis, C., Lawrence, A. and Harding, S. "Electro Mechanical Actuator Test Stand for In-Flight Experiments", Design Project, Dept. Mech. Eng., California Polytechnic State University, San Luis Obispo, CA, 2009.
- [27] Robertson, C.R., "Chapter 3: Three Phase A.C. Circuits", *Further Electrical and Electronic Principles*, 3rd ed. Burlington, MA: Newnes, 2008, pp.104-105.
- [28] Bell, S., "Measurement Good Practice Guide", No 11, *A Beginner's Guide to Uncertainty of Measurement*, Issue 2, National Physical Laboratory Tedington, Middlesex, UK: Crown Copyright, 1999, pp.1.
- [29] Racine, E., Lammers, Z., Barnett, S., Murphy, J. et al., "Energy Analysis of Electromechanical Actuator under Simulated Aircraft Primary Flight Control Surface Load," SAE Technical Paper 2014-01-2182, 2014, doi:10.4271/2014-01-2182.

APPENDIX

Hardware Specifications

Kollmorgen EC5 Electromechanical Actuator

Source: Linear Positioners Catalog_en-US_revA

<http://www.kollmorgen.com/en-us/products/linear-actuators/electric-cylinders/ec5-series>



Figure 82 - Industrial EMA under test

Kollmorgen AKM42G Servomotor

Source: AKM_Selection_Guide_en-US_revA.pdf

<http://www.kollmorgen.com/en-us/products/motors/servo/akm-series/akm-series-ac-synchronous-motors/ac-synchronous-servo-motors>

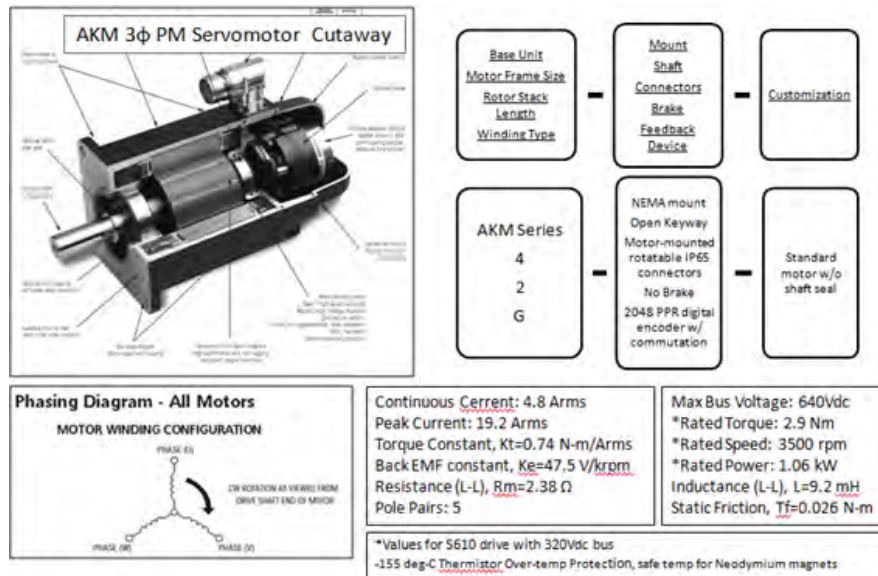


Figure 83 - EMA motor specifications

Kollmorgen S610 Servodrive

Source: S300_S600_Catalog_en-US_RevA

<http://www.kollmorgen.com/en-us/products/drives/servo/serviced-drives/s600/>

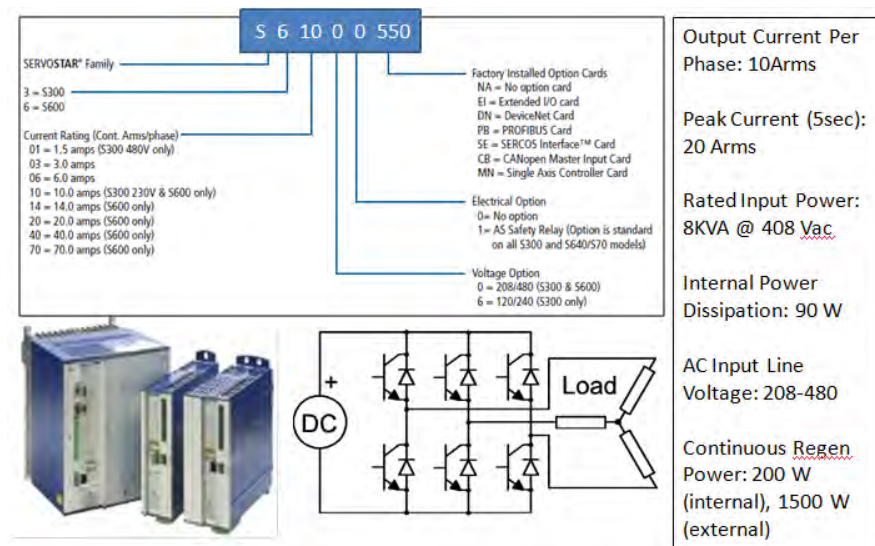


Figure 84- EMA drive specifications

MTS Servohydraulic Load Frame

Source: <http://www.mts.com/en/products/producttype/test-systems/load-frames-uniaxial/servohydraulic/standard/index.htm>

MTS 370.10 22 KIP Load Frame



Actuator Type	Axial
Vert. Test Space (min/max)	Ext 363/1753 mm (14.3/69.0 in)
Load Frame Column Spacing	533 mm (21.0 in)
Load Frame Column Diameter	76.2 mm (3.0 in)
Actuator Location	Integral to Base
Actuator Force Rating	100 kN (22 kip)
Load Cell Force Rating	100 kN (22 kip)
Actuator Dynamic Stroke	250 mm (10 in)
Crosshead Positioning	Hydraulic Powered Adjustment
Crosshead Locks	Hydraulic Powered Adjustment
HSM Maximum Flow Rating	228 lpm (60 gpm) 4 servovalve
Floor Standing HSM	Included
Controller Platform	494 Platform
Calibration - Site	Standard Factory Calibration
Calibration - Electronics	494.16/494.25/494.26
Calibration - Cable Length	7.5 m (25 ft)
Calibration - Output Polarity	Tension (+), Compression (-)
Calibration - Full Scale	250 mm, +/- 150 mm
Installation	On-site

Shown with optional hydraulic grips


Figure 85 - Hydraulic Press specifications

MTS Servohydraulic Controller

Source: <http://www.mts.com/en/products/producttype/test-components/controllers/flextest-controllers/index.htm>

FlexTest 60 Controller

FlexTest 60



Front
(6 VME slots)

Back
(8 transition slots,
7 powered)

About MTS FlexTest Models 40/60/100/200 Controllers

MTS FlexTest Models 40/60/100/200 Controllers are generally used in servohydraulic test systems. They provide real-time closed-loop control, with transducer conditioning and function generation to drive various types of servo-actuators.

A FlexTest Controller consists of:

- One or more Series 494 Hardware chassis that contain controller hardware.
- A computer workstation that runs MTS controller applications.

PARAMETER	FLEXTEST 40	FLEXTEST 60	FLEXTEST 100	FLEXTEST 200
Test Stations	2	Up to 6*	Up to 8	Up to 8
Control Channels	Up to 4	Up to 8	Up to 16	Up to 40
Conditioned Transducer Inputs	Up to 12	Up to 24	Up to 40	Up to 80
Auxiliary Data Inputs	Up to 16	Up to 32	Up to 64	Up to 96

*With On/Off Hydraulic Service Manifolds only

Station Builder

Station Manager

Basic TestWare

Station Desktop Organizer

Hwi File Editor

Controller Management Tool

Figure 86 - Hydraulic Press Controller specifications

MTS Force Transducer

Source: <http://www.mts.com/en/products/producttype/test-components/grips-fixtures-accessories/load-cells-force-transducers/index.htm>

MTS 661.20H-03 Load Cell

Controller Platform
TEDS
Load Cell Model Number
Thread Type
Load Cell Force Rating
Load Cell Thread Form
Load Cell Cable Connector Type
Electronics
Calibration - Site
Cable Length
Calibration - Output Polarity
Calibration - Full Scale



494 Platform
Included
661.20H-03
Metric
100 kN (22 kip)
M27 X 2MM-6H
JT
494.16/494.25/494.26
Standard Factory Calibration
7.5 m (25 ft)
Tension (+), Compression (-)
100 kN (22 kip)

MTS 661 Series Load Cells are designed for a wide array of static and dynamic testing applications. The cells are designed for cyclic operation in through zero tension/compression modes.

- Low deflection and high degree of stiffness gives better dynamic performance.
- High output shear web design resists off-axis loading and moments, increasing accuracy and resolution.
- Proprietary wiring techniques reduce electrical noise.
- Temperature compensation helps ensure stability.
- Designed for easy integration with other accessories, platens, and fixtures.
- Manufactured with aircraft-quality steels, specially heat-treated to minimize distortion.

Figure 87 - Hydraulic Press Load Cell

National Instruments Data Acquisition Machine

Source: NI PXIe-1071 User Manual and Specifications

<http://sine.ni.com/nips/cds/view/p/lang/en/nid/208933>

The DAQ machine is made up of an NI PXI chassis outfitted with a Real-Time controller, and three modules or cards—one for electrical, mechanical, and thermal measurements.

NI PXIe-1071, 4-Slot 3U PXI Express Chassis

781368-01



- 3 hybrid slots
- 230 W total power available from 0 to 50 °C
- High performance - up to 1 GB/s per-slot dedicated bandwidth and 3 GB/s system bandwidth
- Compact and lightweight PXI chassis, 13.1 lb (5.94 kg)
- Compatibility with PXI, PXI Express, Compact PCI, and Compact PCI Express modules

Figure 88 - PXIe Chassis

NI PXIe-8102 1.9 GHz Dual Core Real-Time Embedded SW

781184-33



- Deployment platform for LabVIEW Real-Time and LabWindows™/CVI Real-Time applications
- Execution target for NI LabVIEW Real-Time Version 8.6.1 or later applications
- 1 GB (1 x 1 GB DIMM) 800 MHz DDR2 RAM standard, 2 GB maximum
- 1 GB/s maximum system and 250 MB/s maximum slot bandwidth
- Integrated hard-drive, USB, serial, Gigabit Ethernet, and other peripheral I/O

Figure 89 - PXI Controller

NI PXIe-6361, X Series DAQ (16 AI, 24 DIO, 2 AO)

781055-01



- 16 analog inputs, 2 MS/s 1-channel, 1 MS/s multichannel; 16-bit resolution, ± 10 V
- Two analog outputs, 2.86 MS/s, 16-bit resolution, ± 10 V
- 24 digital I/O lines (8 hardware-timed up to 10 MHz)
- Four 32-bit counter/timers for PWM, encoder, frequency, event counting, and more
- Analog and digital triggering and advanced timing with NI-STC3 technology
- Support for Windows 7/Vista/XP/2000

Figure 90 - Module 1—Electrical Card

NI PXIe-6366, X Series DAQ (8 Simultaneous AI, 24 DIO, 2 AO)

781057-01



- 8 simultaneous analog inputs at 2 MS/s/ch with 16-bit resolution; 16 MS/s total AI throughput
- Two analog outputs, 3.33 MS/s, 16-bit resolution, ± 10 V
- 24 digital I/O lines (8 hardware-timed up to 10 MHz)
- Four 32-bit counter/timers for PWM, encoder, frequency, event counting, and more
- Analog and digital triggering and advanced timing with NI-STC3 technology
- Support for Windows 7/Vista/XP/2000

Figure 91 - Module 2—Mechanical Card

**NI PXIe-4353 32-Ch Thermocouple
Input**
781348-01



**NI TB-4353 Isothermal Terminal Block
for PXIe-4353**
781349-01



- Front mounting terminal block for the NI PXIe-4353
 - Built-in cold-junction compensation
 - Screw terminal connectivity
 - Autodetected; hot swappable
-
- 32 thermocouple input channels; 8 built-in cold-junction compensation channels; 0.3 °C accuracy
 - 90 S/s/ch sample rate in high-speed mode; 1 S/s/ch sample rate in high-resolution mode
 - 300 Vrms CAT II channel-to-earth ground safety isolation
 - Autozero channels for offset error compensation; open-thermocouple detection
 - Multidevice triggering and synchronization via PXI Express
 - NI-DAQmx driver software and NI LabVIEW SignalExpress LE interactive data-logging software

Figure 92 - Module 3—Thermal Card

Newton's 4th Power Analyzer

Source: <http://www.newtons4th.com/products/power-analyzers/ppa5500-precision-power-analyzer/>

User Manual: <http://newtons4th.com/wp-content/uploads/2014/07/PPA55xx-User-Manual.pdf>

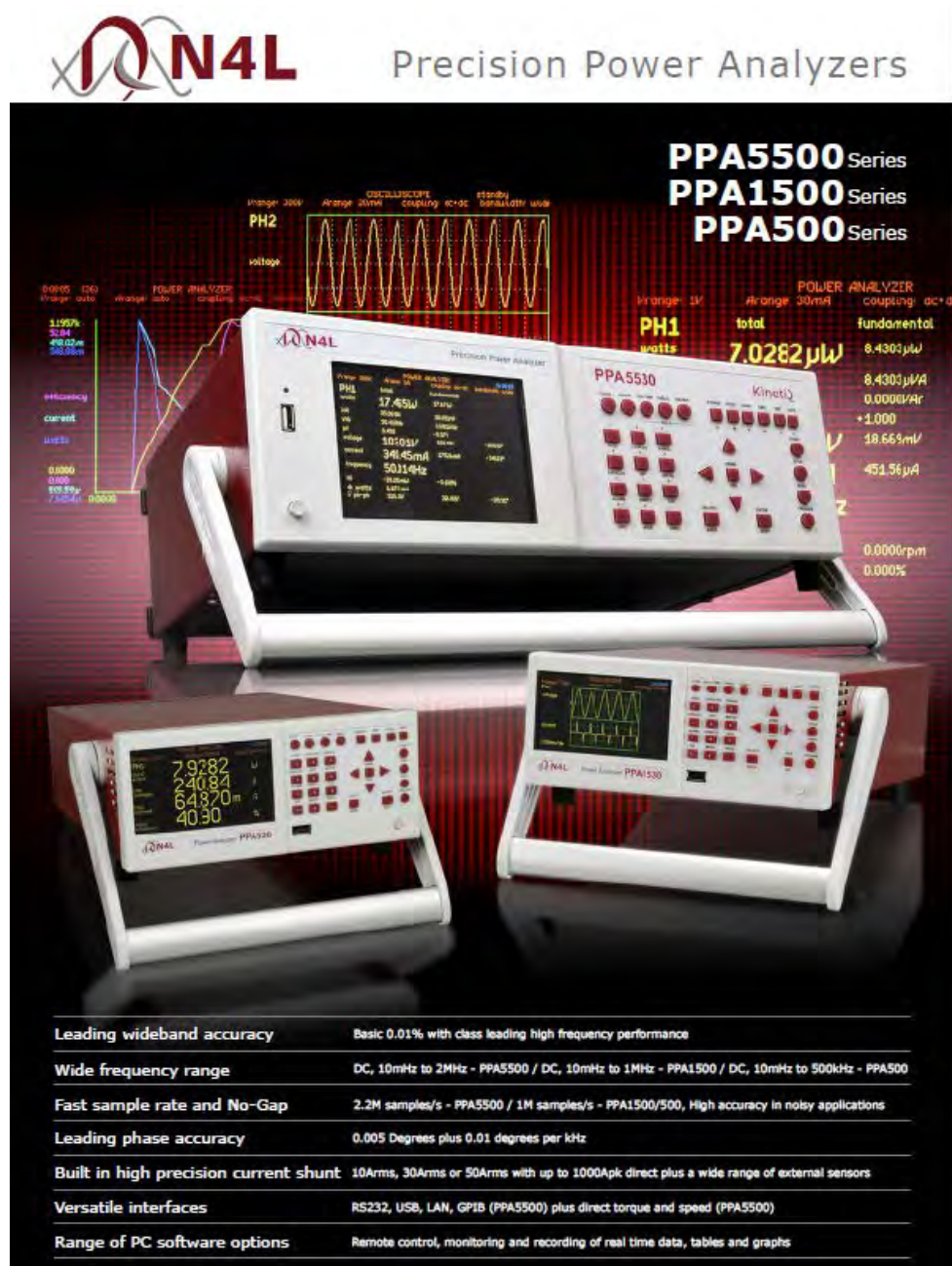


Figure 93 - Newton's 4th Power Analyzer

LEM Current Transducer and Tectronix Voltage Probe

Source: High-voltage Differential Probes, Current Transducer LA 55-P

<http://www.tek.com/differential-probe-high-voltage>

<http://www.alldatasheet.com/datasheet-pdf/pdf/114818/LEM/LA55-P.html>

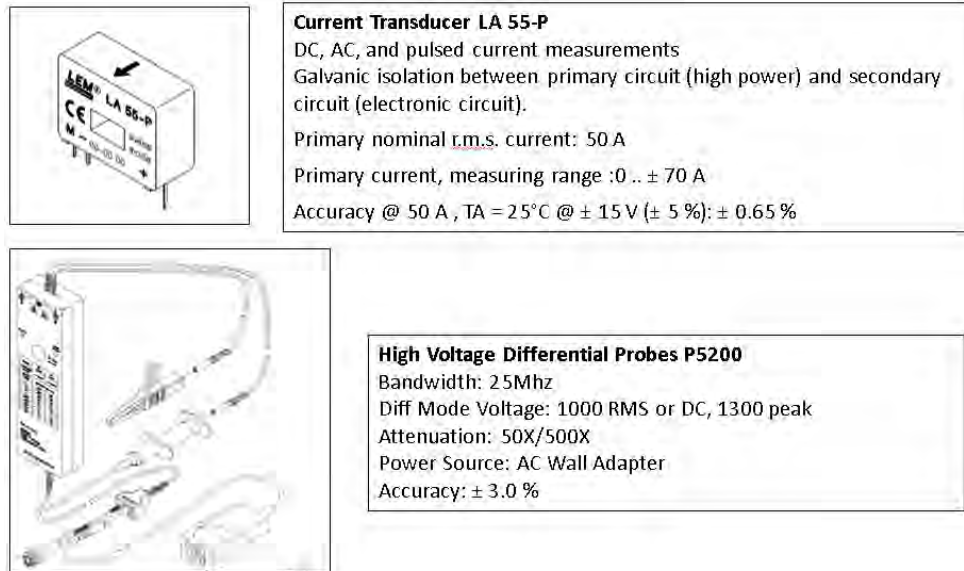


Figure 94 - Electrical Sensors

Omega Thermocouples Probes

Source: <http://www.omega.com/pptst/JMQSS.html>

Quick Disconnect Thermocouples with Miniature Connectors

(*)MQSS Series -JMQSS, KMQSS, EMQSS, TMQSS, NMQIN



OMEGA's Quick Disconnect Thermocouples with Miniature Connectors are high quality, economical thermocouple probes. They feature a glass filled nylon connector which is rated for temperatures up to 220°C (425°F). The probes are available in with diameters as small as 0.25mm(0.010 inches) and as large as to 3.0mm(0.125 inches).

Figure 95 - Thermocouples